



# Development of a magnet system for the CERN BDF/SHiP Facility

Victoria Bayliss, Josef Boehm

Rutherford Appleton Laboratory, STFC (UK)

## Abstract

The SHiP experimental setup requires a magnet-based shield immediately after the proton target in order to deflect the very large background flux of muons away from the detector acceptance. To this end, a magnet system integrated within the hadron stopper in the target bunker has been proposed. The aim of this work was to move the design of the magnet system within the target shielding from a conceptual stage to a preliminary engineering design. This was done taking into account the strict constraints on the design and integration aspects of the magnet system imposed by the integration and remote handling of the target complex. In order to arrive at a sufficient level of understanding of the implementation of the magnet system, its performance and costs, and the development timeline, a preliminary engineering study has been done in close collaboration with the Beam Dump Facility (BDF) target complex team and the SHiP experiment team as part of the BDF/SHiP Comprehensive Design Studies.

## Change Record

Issue	Change	Person
1.0	Initial issue	VB
2.0	Reissued with review action items listed in SD3. (24/07/2019)	VB
3.0	Reissued with comments from R Jacobsson (22/08/2019)	JB
3.1	Issued V3 of report as public note	JB

This document "G:\01 Projects\03 Magnets & Facilities Programme\2018-BDF\_Design\_Document\02 Documentation\2019-BDF\_Design\_ReportG:\01 Projects\03 Magnets & Facilities Programme\2018-BDF\_Design\_Document\02 Documentation\2019-BDF\_Design\_Report V3.docx"

## Supporting Documents

ID	Title	File name/document reference
SD1	Drawings of coil former with details for cooling channels	BDF_Magnet_Former.dfx
SD2	BDF Magnet field map	20190717 BDF Magnet BField Map.txt
SD3	Minutes from technical review of documentation	MM-SHIP-190701-RAL
SD4	BDF model file	201907 Full BDF_3_FinalBaseline_SeparateMaterials.model

## Table of Contents

1.	Introduction and Scope.....	8
1.1.	Scope.....	8
1.2.	BDF Target and Target Complex (TTC) overview .....	9
1.3.	Magnet requirements.....	10
2.	Magnetic fields.....	10
2.1.	Development of basic magnetic model .....	12
2.1.1.	BH Curves.....	12
2.1.2.	Model extent.....	13
2.1.3.	Shape of magnet core blocks.....	13
2.1.4.	Size of gaps between blocks .....	15
2.2.	Optimisation of magnet yoke geometry.....	17
2.2.1.	Stainless Steel pillar .....	18
2.2.2.	Magnetic iron return path .....	19
2.2.3.	Varying gaps in magnetic iron.....	20
2.2.4.	Reducing stray field at coil ends .....	20
2.2.5.	Reducing compression of flux lines through the coil.....	24
2.3.	Optimisation of Coil Geometry .....	25
2.3.1.	Coil packing factor.....	25
2.3.2.	Coil bend radius .....	25
2.3.3.	Sizing the coil: Current density, aspect ratio and Ampere-turns.....	26
2.4.	Summary of magnet optimisation (Geometry & Performance) .....	30
2.5.	Forces.....	33
2.5.1.	Forces on shielding.....	33
2.5.2.	Forces on coil .....	37
2.6.	Stray fields.....	38
2.6.1.	Stray fields from within the target area.....	38
2.6.2.	Stray fields outside of the target bunker shielding.....	39
3.	Assessment of hysteresis effects after multiple energisation .....	41
4.	Preliminary engineering design of the magnet coil .....	43

4.1.	Comparison of different coil materials .....	43
4.2.	Gas-cooled vs liquid-cooled coil.....	44
4.3.	Aluminium coil .....	45
4.3.1.	Example of a small aluminium coil.....	46
4.3.2.	Pressure drop of cooling circuit of aluminium heat exchangers .....	47
4.4.	Copper coil .....	48
4.4.1.	Example of existing copper coil .....	48
4.4.2.	Pressure drop of cooling water, hollow copper conductor .....	50
4.4.3.	Separation of electric and coolant circuits .....	51
4.5.	Influence of ionising radiation on magnet materials.....	52
4.5.1.	Potting material for copper coils .....	53
4.5.2.	Interface material for aluminium coils.....	54
5.	Gas-cooled coil.....	54
5.1.1.	Gas cooling layout for an aluminium coil.....	55
5.2.	Design of the gas-cooled coil .....	57
5.3.	Coil data .....	58
5.3.1.	Sub-dividing the aluminium coil to obtain redundancy.....	59
5.3.2.	Calculations of cooling requirements .....	59
5.3.3.	Supply of helium gas to coil body .....	62
5.4.	Assembly of magnet coil into steel housing .....	64
5.4.1.	Assembly of coil at site of coil manufacturer.....	67
5.5.	Assembly of helium gas supply channel .....	68
6.	Sensors.....	72
6.1.	Temperature sensors on magnet coil .....	72
6.2.	Magnetic flux density at defined locations.....	73
6.3.	Flux density integral over core of magnet .....	74
7.	Requirements for the operation of the magnet coil.....	75
8.	Information relevant to manufacture.....	75
8.1.	Potential suppliers .....	75
8.1.1.	Magnet coil .....	75
8.1.2.	Magnet instrumentation.....	76
8.1.3.	Low carbon steel .....	76
8.2.	Cost estimation for the development phase .....	76
8.3.	Production of the final magnet system.....	78

9.	Final Design .....	79
10.	Conclusions .....	81
Appendix A.	BH data used in magnetic modelling .....	82
Appendix B.	BH curves used in the Hysteretic Opera model .....	83

## List of Figures and Tables

Figure 1:	Concept design for the target and target complex (TTC) .....	9
Figure 2:	Baseline model - full model with air regions on RHS and regions of interest on LHS .....	10
Figure 3:	Flux path around the desired magnetic circuit shown with black solid arrows, flux short-circuiting through alternate routes shown by black dashed arrows .....	11
Figure 4:	B-field through cross-section at centre of magnet (z=0mm).....	11
Figure 5:	BH data.....	13
Figure 6:	Helium container end plate (left) and coil service chimney models .....	13
Figure 7:	Effect on B-field along the beamline axis from gaps impeding the movement of flux in z...	14
Figure 8:	Top left: Simple block configuration; Top right: Overlapping blocks in z; Bottom: Overall arrangement (CERN) .....	15
Figure 9:	Gap naming convention for descriptions used in Table 1 .....	15
Figure 10:	Magnetic model showing the beamline axis along which the field is considered as a black dashed line .....	18
Figure 11:	Example of B-field along the beamline.....	18
Figure 12:	Left: Impact of stainless steel thickness on the integrated field along the beamline, Right: Stainless Steel thickness dimension.....	19
Figure 13:	Impact of the dimensions of the magnet iron return path on the Integrated B-field along the beamline .....	19
Figure 14:	Impact of gap sizes on the integrated B-field along the beamline .....	20
Figure 15:	Magnetic flux short-circuiting around the coil. Flux shown by purple arrows .....	20
Figure 16:	Modifying the bunker and proximity shielding to prevent flux loss on the beamline: Top left: Baseline. Top right: "Half cut". Bottom Left: Simple SS blocks. Bottom right: SS spacer .....	21
Figure 17:	Impact of modifying the proximity and bunker shielding on integrated field.....	22
Figure 18:	Top left: Integrated field comparison. Top right: B field on axis comparison. Bottom: Variations considered for modifications to magnet iron.....	23
Figure 19:	Compression of magnetic flux through the coil.....	24
Figure 20:	Impact of packing factor on the integrated B-field along the beamline .....	25
Figure 21:	Impact of coil radius on the integrated B-field along the beamline .....	26
Figure 22:	Integrated field with increasing number of ampere-turns, $0.35\text{A}/\text{mm}^2$ .....	26
Figure 23:	Integrated field with increasing number of ampere-turns, at $0.35\text{A}/\text{mm}^2$ and $0.45\text{A}/\text{mm}^2$ , with coil height 300mm .....	27
Figure 24:	Integrated field with increasing number of ampere-turns, at $0.35\text{A}/\text{mm}^2$ (solid lines) and $0.45\text{A}/\text{mm}^2$ (dashed lines), and coils heights set to 300mm, 320mm and 340mm.....	27
Figure 25:	Performance with power for Coil A and Coil B .....	28

Figure 26: Performance of Coil A and Coil B with current ramping, compared to the performance of optimised coils for given current densities (as Figure 23) .....	29
Figure 27: Performance of Coil A and Coil B with current ramping.....	29
Figure 28: B-field profile along the beamline in final model .....	30
Figure 29: Comparison of effect of modifications .....	31
Figure 30: Final model with individual magnet and shielding blocks modelled in separate materials	33
Figure 31: Forces on the coil .....	37
Figure 32: Internal surface of the target region/proximity shielding .....	38
Figure 33: Field maps through the target region at 200mm height intervals (top left at 200mm height, then top right, bottom left and bottom right) overlaid over the target region mesh. B-fields on the outer edge reach $1.4 \times 10^{-1} \text{T}$ and everywhere else is $\sim 5 \times 10^{-4} \text{T}$ (5 Gauss) .....	39
Figure 34: Fields on the outside of the shielding of the target complex .....	40
Figure 35: Fields at 1m from the surface of the shielding of the target complex .....	40
Figure 36 Demagnetisation of iron by alternating the applied field H (proportional to current I) .....	41
Figure 37: System of aluminium coil with heat exchanger glued to the top of the coil.....	46
Figure 38: Small aluminium coil with attached heat sinks: single cooling circuit on left, divided circuit on right.....	46
Figure 39: Experimental set-up of sample aluminium coil with .....	47
Figure 40: Aluminium heat exchanger with embedded channels seen in cross section, unit is friction-welded.....	47
Figure 41: Dipole coil embedded in flux return yoke, seen from below .....	48
Figure 42: Area where the electric and cooling circuits are split.....	49
Figure 43: Cross sectional view of a compound copper coil, 9x9mm conductor, 4mm hole .....	49
Figure 44: Profiles of hollow copper conductor and insulation (Luvata of Finland).....	49
Figure 45: Comparison of 15mm with different orifices.....	50
Figure 46: Coolant manifold and coolant / electricity separation, on right: electrics in brown, coolant in blue / red.....	51
Figure 47: Proton beam coming from left, target area and magnet block with coil .....	52
Figure 48: Average annual radiation dose at coil height .....	53
Figure 49: Restraint of Aluminium coil to keep interface undisturbed, heat exchanger can be at top or bottom of coil, or both.....	54
Figure 50: Cooling of the helium container and coil with helium gas, separate and combined variations (scheme by CERN) .....	56
Figure 51: Retention of aluminium coil in magnet former at bottom .....	57
Figure 52: Engineering values for heat transfer coefficients.....	60
Figure 53: Gas flow and cooling calculation for energised coil .....	61
Figure 54: Downstream gas inlet with cover plate .....	62
Figure 55: Upstream gas outlet with cover plate .....	63
Figure 56: Flow velocity and pressure drop of helium gas in 3m feed duct for various duct diameters .....	63
Figure 57: Coil in steel former, seen from below, showing retainer struts for holding coil.....	64
Figure 58: Retainer struts for coil, showing insulating PEEK insert (10mm high) and diagonal gas-flow channels .....	64
Figure 59: Bottom view of coil former, showing magnet channel and supply tube.....	65
Figure 60 Magnet former and coil from below, cross-strut vertical (image by CERN).....	65

Figure 61: Side view of magnet former, showing downstream and upstream ends.....	66
Figure 62: Retention of the aluminium coil within the magnet former, seen from above, also showing the location plugs.....	67
Figure 63: Proposal of an arrangement of magnet coil former (dark blue, with dowel pins) and iron blocks above it .....	68
Figure 64: Coil former is delivered with fixed gas stand-pipe and loose electrical cabling.....	69
Figure 65: Magnet former (dark blue) with coil inside (yellow) and shielding blocks above (grey), shown midway between down and upstream side.....	70
Figure 66: Coil body surrounded by coil former (only one halve shown) and attached supply channel which is split.....	71
Figure 67: Hood above helium container with gas cooling supply and coil power connections (sensor wiring not shown, will be parallel to coil power cables).....	72
Figure 68: Temperature sensor, set in Stycast, on aluminium substrate .....	73
Figure 69: Location of Hall sensors on the steel yoke as seen from below, Hall sensors doubled for redundancy .....	73
Figure 70: Example of a simple method for calculating the integrated flux through the magnet structure.....	74
Figure 71 2D model for a quarter-scale prototype magnet.....	77
Figure 72: Hybrid magnet structure, showing low carbon steel (grey), grain-oriented steel sheets (yellow) and magnet coil (red). Stainless steel is shown in white. ....	77
Figure 73: B-field profile along the beamline in final model .....	79
Figure 74 Outline of magnet body, showing materials and dimensions, magnet coil behind end cover plate .....	80
Table 1: Gap sizes.....	16
Table 2: Coil parameters for Coil A and Coil B .....	28
Table 3: Recommendations for dimensions changes based on optimising the magnetic circuit, also see Figure 74 .....	32
Table 4: Forces on magnet blocks.....	34
Table 5: Forces on proximity shielding blocks and Helium vessel .....	35
Table 6: Highest forces on the bunker shielding.....	36
Table 7: Effect of diameter of cooling water channel on pressure drop .....	50
Table 8: Coil data, gas-cooled coil structure.....	58
Table 9: Electrical resistivity and coil power consumption vs Temperature, base resistivity taken from manufacturer .....	58
Table 10: Physical expansion of coil body due to temperature rise .....	66
Table 11: Sizes of low carbon steel available from British Steel.....	76

## 1. Introduction and Scope

CERN is in the process of evaluating the feasibility of a new experimental facility, the so-called Beam Dump Facility (“BDF”), with the primary goal of hosting the search for Hidden Particles (“SHiP”) experiment. An executive summary of the CDS was submitted to European Particle Physics Strategy Update in December 2018 following the SHiP/BDF Technical Proposal submitted in 2015.

The experimental setup requires a magnet-based shield immediately after the proton target in order to deflect the very large background flux of muons away from the detector acceptance. The muon shield project is a collaboration between STFC, CERN (EP and EN departments) and Russian scientific institutes. Rutherford Appleton Laboratory (“RAL”) actively contributed to the preliminary engineering studies of the muon shield to the SHiP/BDF Technical Proposal (April 2015) and studies thereafter. Following a proposal by STFC/RAL in 2016, the muon shield now starts with a magnet system integrated within the hadron stopper in the target bunker. This solution has been studied as part of the physics re-optimization of the experimental configuration. It greatly improves the performance and reduces the overall size and cost of the free-standing part of the muon shield. The design has also been elaborated as part of the handling and integration study for the target complex.

The aim of this work package (as described in the Collaboration Agreement Reference KE4149/BE) is to move the design of the magnet system within the target shielding from a conceptual stage to a preliminary engineering design. This is done taking into account the strict constraints on the design and integration aspects of the magnet system imposed by the integration and remote handling of the target complex. In order to arrive at a sufficient level of understanding of the implementation of the magnet system, its performance and costs, and the development timeline, STFC completed a preliminary engineering design in close collaboration with the Target Complex team and the experiment team.

### 1.1.Scope

This study comprises the following aspects, which are addressed in this report:

- Optimisation of the magnetic circuit resulting in a final definition of the system. Outcomes of this include
  - o the simulated field maps for use in physics simulations and for the optimisation and engineering of the subsequent magnet chain;
  - o understanding of hysteresis effects after multiple powering cycles;
  - o understanding of the magnetic forces of the entire magnetized assembly and interaction with the external/contiguous shielding;
  - o understanding of stray fields, for example in the vicinity of the target
- a preliminary engineering design compatible with the Target Complex Design and the radiation environment, including
  - o thermal management (consideration of water and gas cooling, technical solution for connection for preferred option)
  - o powering requirements
  - o technical solution for connections of power cables, sensors etc.
  - o proposed technical solution for the integration of magnetic iron blocks inside the coil for handling reasons, compatible with the target Complex design



- any other infrastructure requirements in the Target Complex for coil operation
  - consideration of engineering risks (water leaks, short circuits etc)
  - long-term durability and reliability of the designed coil
- Plans for the future developments
- Cost estimates for the development phase and the production of the final magnet system
  - Proposed plan for prototyping the coil

## 1.2.BDF Target and Target Complex (TTC) overview

The target and target complex is still in development; the current design is referred to as the 'crane++' concept, shown in Figure 1 (Image provided by CERN 30/July/2019)

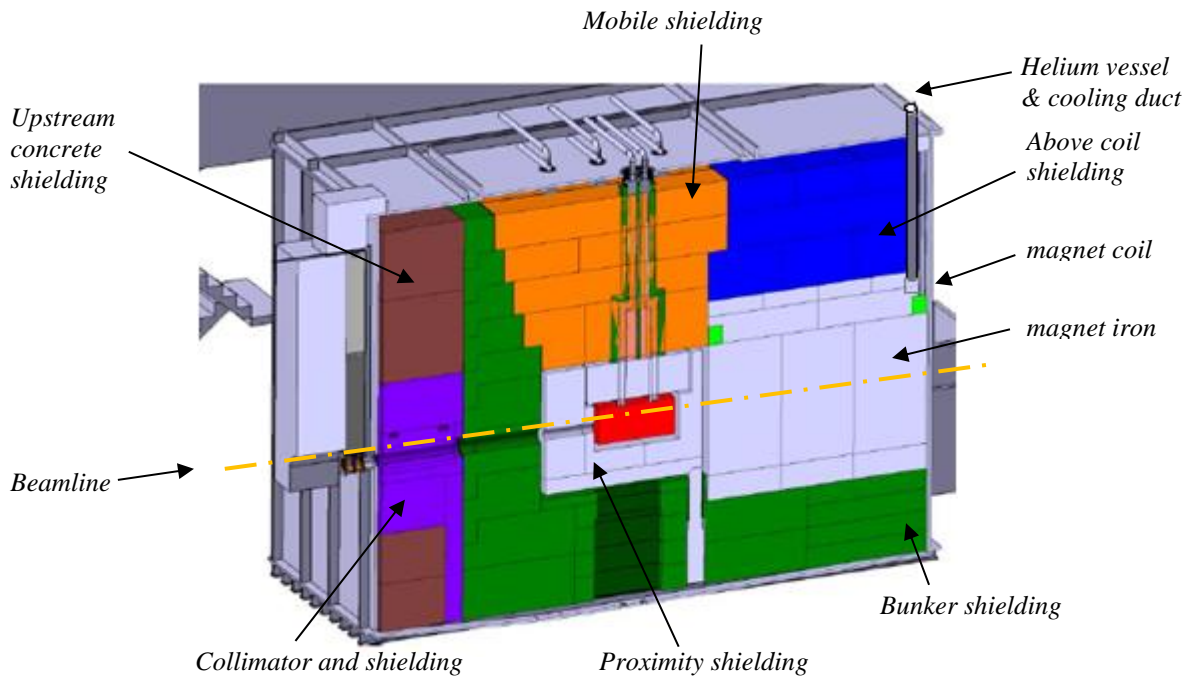


Figure 1: Concept design for the target and target complex (TTC)<sup>1</sup>

<sup>1</sup> 20190122\_BDFcranepiusplus.pdf

### 1.3. Magnet requirements

The aim of the magnet is to start sweeping muons out of the beamline as soon as possible after their production in the target. The extent of the magnet core, the central vertical pillar of magnetic iron above which the coil sits, is sized to maximise the impact of the magnet. It extends the full length of the shielding downstream of the target shielding, and 0.5m below and to either side of the beamline itself. Although the core only needs to extend 0.5m above the beamline, the coil is positioned higher than this in order to move it into a region of manageable radiation (see Section 4.5 for details.)

The number of muons which are swept out of the beamline in this region is determined by the strength of the magnetic field; this has a significant impact on the length of the muon shield downstream of the target bunker. The initial aim was to achieve 1.8T in this region; this was traded off with the cooling requirements for the coil to achieve such a high field. Ultimately it was decided to use a gas cooled magnet, limiting the power of the coil to 4kW.

## 2. Magnetic fields

A parameterised magnetic model for the target bunker has been developed in Opera Vector Fields software, as shown in Figure 2.

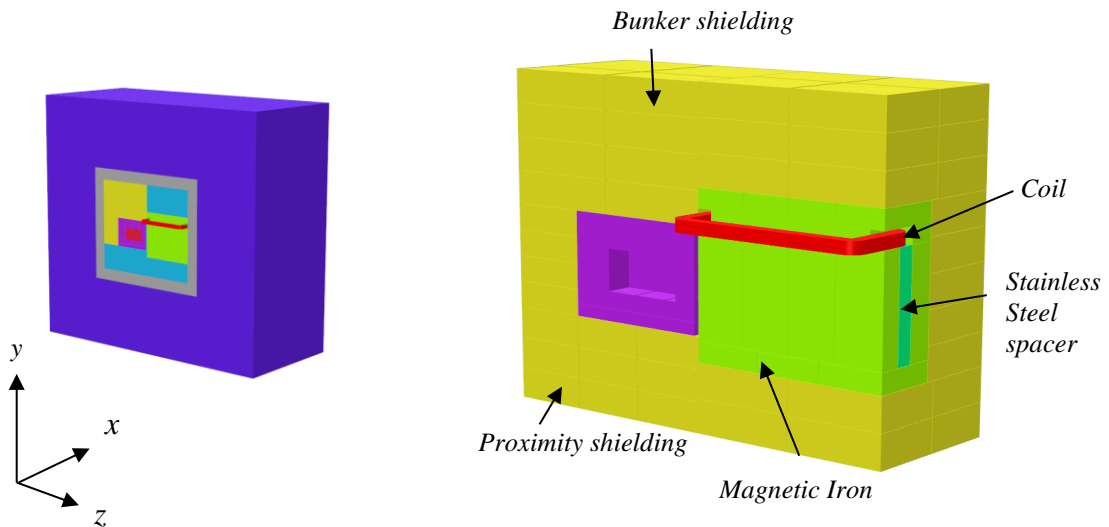


Figure 2: Baseline model - full model with air regions on RHS and regions of interest on LHS

The model used symmetry in the YZ plane to reduce solution times. In the regions of interest the model accurately represents the shielding block shapes in the engineering drawings and in the outer cast-iron shielding representative blocks are used (the correct number of blocks is used but a simplified shape has been adopted).

The magnetic circuit is shown in Figure 3 with the flux direction of the magnetic circuit indicated with black arrows. The useful region is the central pillar of magnetic iron with the flux going downwards – this is the region used to sweep muons out of the beamline and is referred to as the magnet core in

this report. The rest of the magnet iron provides a low reluctance route for the returning flux and is referred to as the magnet return path.

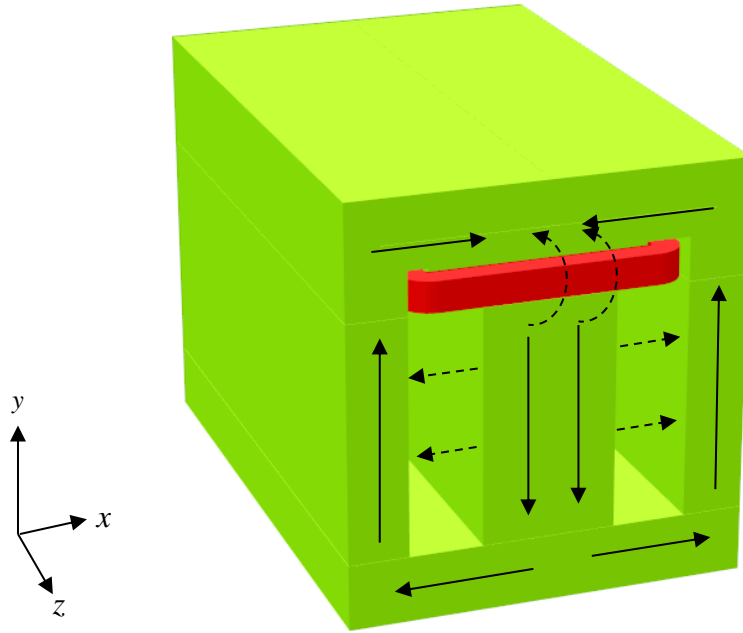


Figure 3: Flux path around the desired magnetic circuit shown with black solid arrows, flux short-circuiting through alternate routes shown by black dashed arrows

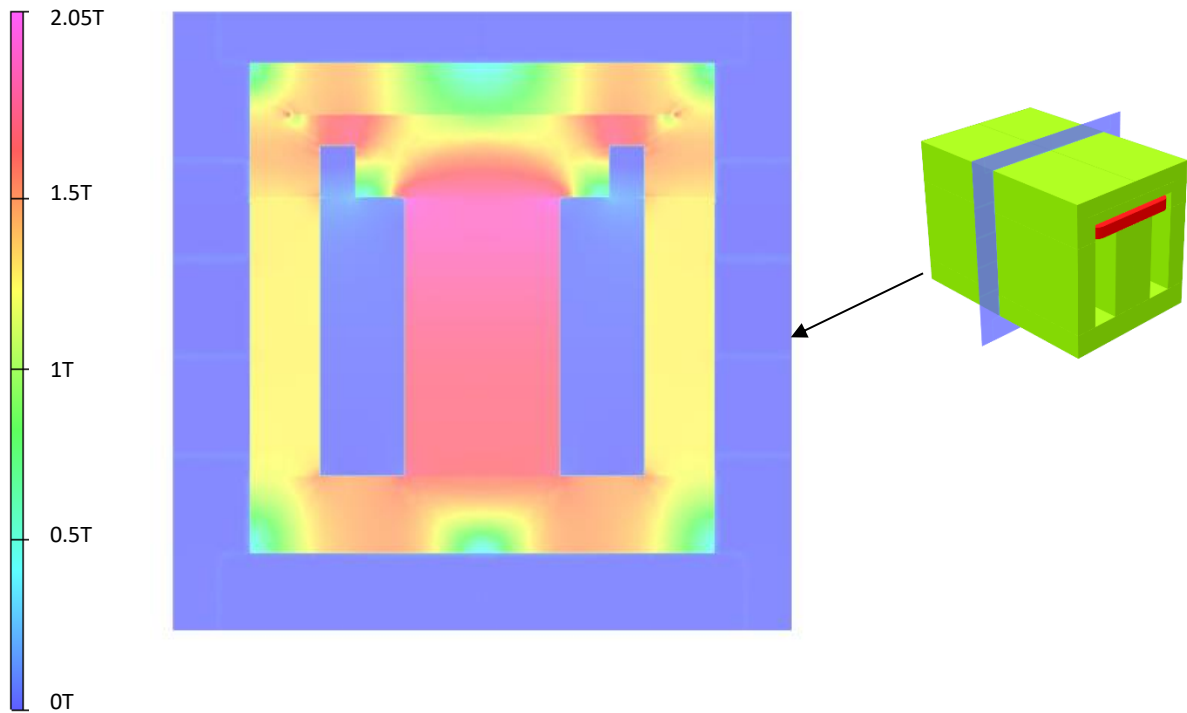


Figure 4: B-field through cross-section at centre of magnet ( $z=0\text{mm}$ )

The figure of merit used throughout the magnetic design is the integrated field along the beamline axis together with a similar field integral throughout the volume of the magnet core.

$$\text{Integrated field (Tmm)} = \int_{Z_{\max}}^{Z_{\min}} B dz$$

Where the beamline passes along the Z-axis from  $Z_{\min}$  to  $Z_{\max}$ .

## 2.1. Development of basic magnetic model

### 2.1.1. BH Curves

There are three materials used in the model and they are cast iron (GJS400-15), magnetic iron (baselined at US1010) and a nominally non-magnetic stainless steel.

The main magnet is assumed to be made of US1010 – the basic data used is that provided by Opera FEA software. This has been shown to compare well to measured data collected at RAL and to data used at CERN<sup>2</sup>. To build some tolerance into the model, the BH data used in the model is 97% that of the original Opera FEA data. In initial models, this reduced the B-field on the beamline axis in the order of 0.05T.

The data for the cast iron is taken from a presentation by the Magnet Technology Centre<sup>3</sup>. Initial modelling showed that changing the BH curve for the cast iron of the order 5% had a negligible effect on the B-field calculated on the beamline axis.

The stainless steel is expected to have a relative permeability of 1-1.05<sup>4</sup> - for comparison, US1010 is of the order of 1000. A conservative value of 1.1 has been used for the modelling for stainless steel – the increased permeability will allow more flux across the stainless steel spacer and therefore a lower flux in the magnet core. In initial models, using 1.1 rather than 1.05 reduced the B-field on the beamline axis in the order of 0.004T.

The BH curves used are shown in Figure 5 and the raw data is included in Appendix A.

---

<sup>2</sup> Davide Tommasini

<sup>3</sup> PRIZZTECH Magnetic properties of cast iron, Sampo Tuominen, Magnet Technology Centre

<sup>4</sup> Magnetic properties of stainless steel, Stainless Steel Advisory Service Information Sheet No.2.81

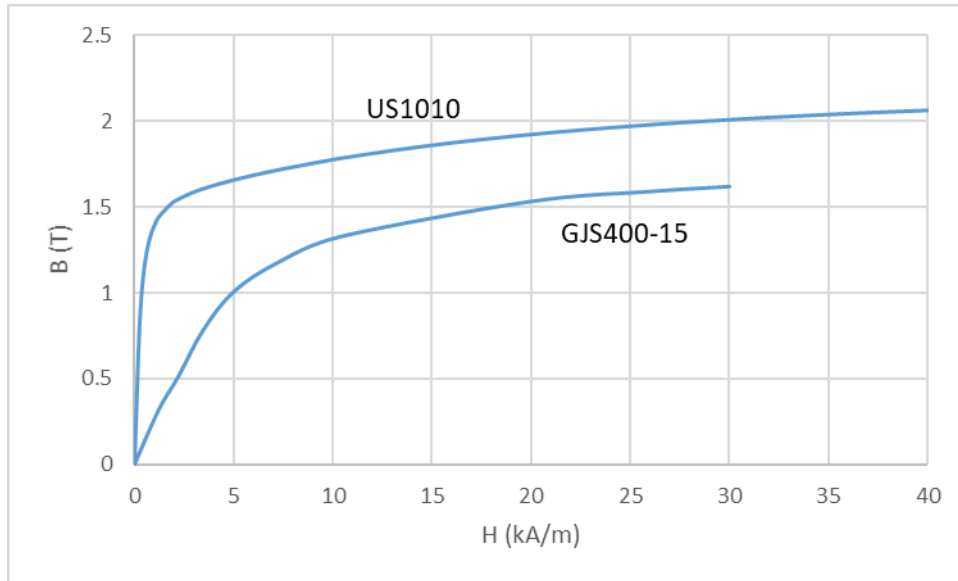


Figure 5: BH data

### 2.1.2. Model extent

Some details, such as the service ‘chimney’ for the coil and the helium vessel are omitted from the baseline model as they have been shown to have a negligible effect on the B-field in the core of the magnet.

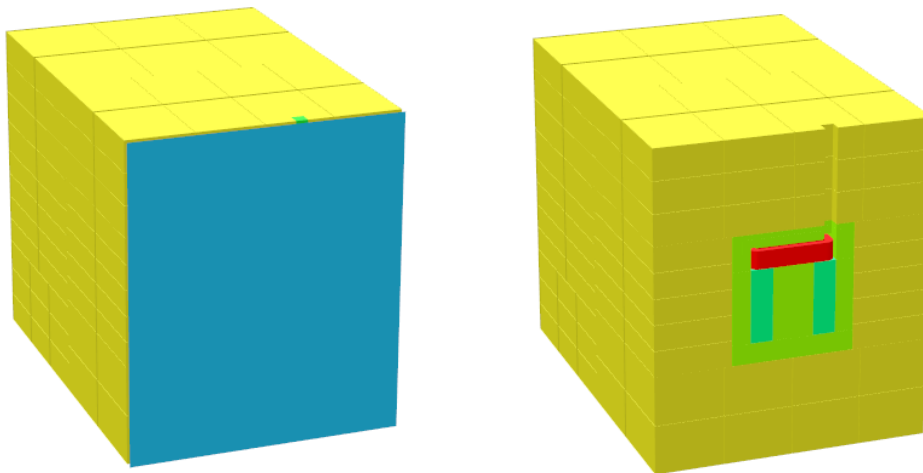
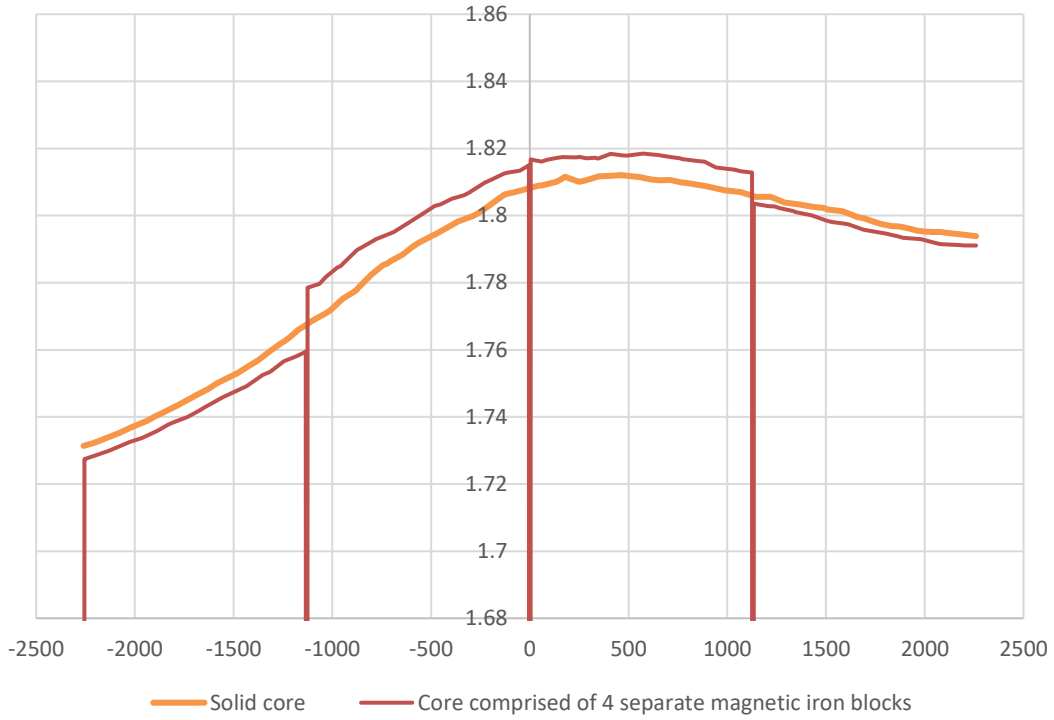


Figure 6: Helium container end plate (left) and coil service chimney models

### 2.1.3. Shape of magnet core blocks

In the magnet core, the vertical gaps between neighbouring blocks of magnet iron impede the flow of the flux between blocks – this means that the centre blocks have a higher magnetic flux than the outer blocks, the overall reluctance of the average flux path is higher, and there is a slightly lower integrated field than if there were no gaps. This can be seen in Figure 7.



**Figure 7: Effect on B-field along the beamline axis from gaps impeding the movement of flux in z**

To combat this effect, the option of having blocks overlapping in z was considered. This would increase the surface area between neighbouring blocks and therefore provide a lower reluctance path between blocks. Example of the blocks considered are shown in Figure 8. However modelling showed that this had a negligible effect on the shape of the B-field along the axis and so simple blocks will be used in all further studies.

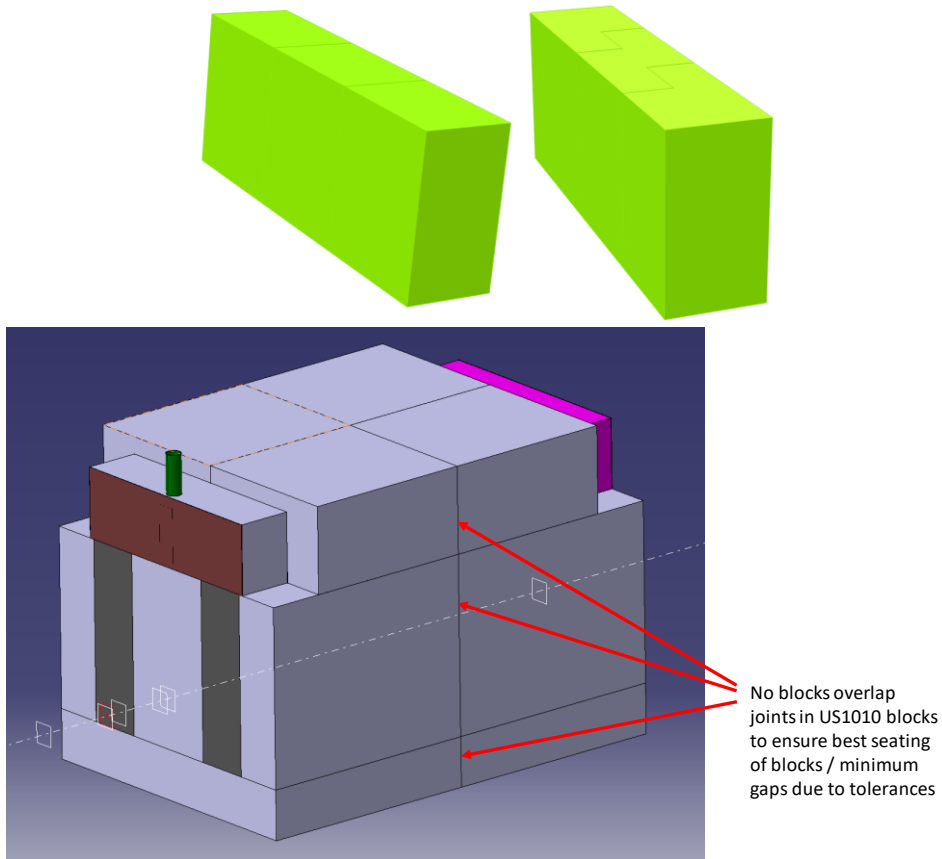


Figure 8: Top left: Simple block configuration; Top right: Overlapping blocks in z; Bottom: Overall arrangement (CERN)

#### 2.1.4. Size of gaps between blocks

The size of the gaps between blocks has a significant effect on the magnetic circuit as the reluctance of air is so much higher than that of the magnetic iron. The approach used to decide what gaps sizes to model has been to establish what gap sizes are possible and then model the worst case scenario; the worst case can be either the minimum gap size or the maximum gap size, depending on the location of the gap. This is summarised in Table 1; an example of the location of the gaps shown in Table 1 is shown in Figure 8.

The effect of gap size is considered further in the optimisation of geometry (2.2); there is some iteration between the manufacturing tolerances accepted and the impact of the gap size.

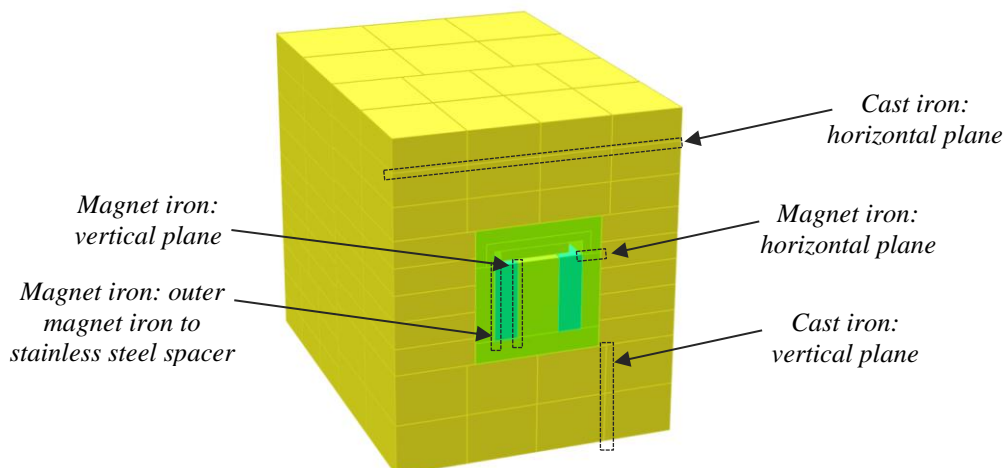


Figure 9: Gap naming convention for descriptions used in Table 1

Table 1: Gap sizes

Location	Reality		Baseline	
	Range	How range is defined	Size in baseline	Why
Magnetic iron: gaps in horizontal plane	≤2mm	Manufacturing tolerances for flatness and perpendicularity of 0.5mm can be achieved on each of the neighbouring blocks. Assembly tolerances do not apply as gravity will ensure the blocks are in contact.	2mm	The reluctance of the gaps in the main circuit will add to the overall reluctance, and therefore reduce the total flux generated by the coil. The worst case is therefore maximum reluctance.
Magnetic iron: gaps in vertical plane	≤7mm	In most cases assembly tolerances will dominate; blocks can be positioned to within 3-5mm <sup>5</sup> . Manufacturing tolerances for flatness and perpendicularity of 0.5mm can be achieved on each of the neighbouring blocks.	0mm	Any reluctance between the inner magnet core and the outer magnet return would reduce the amount of magnetic flux shortcutting across the stainless steel spacer. The worst case scenario is therefore zero gaps and minimum reluctance.
	≤2mm	The outer magnet iron will be bolted to the stainless steel spacer for positioning, so this gap will only be effected by the manufacturing tolerances.	0mm	
Cast iron: gaps in horizontal plane	≤20mm	Manufacturing tolerances for flatness and perpendicularity of 10mm can be achieved on each of the neighbouring blocks. Assembly tolerances do not apply as gravity will ensure the blocks are in contact.	10mm	Some flux from the return path of the magnetic circuit flows through the cast in iron in preference to the saturated iron. Due to the large volume of cast iron available, the gap size does not significantly affect how much magnetic flux doe this; therefore an average expected gap size has been used.
Cast iron: gaps in vertical plane	≤25mm	Manufacturing tolerances for flatness and perpendicularity of 10mm can be achieved on each of the neighbouring blocks. Assembly tolerances: blocks can be positioned to within 3-5mm.	10mm	
Gap between the magnetic iron and the proximity shielding	≤16mm	Manufacturing tolerances for flatness and perpendicularity of 10mm can be achieved on the cast iron and 0.5mm on the magnetic iron. Assembly tolerances: blocks can be positioned to within 3-5mm.	0mm	Some flux shortcuts directly through the cast iron around at this point rather than going around the desired magnetic circuit. The worst case scenario is therefore to assume the minimum reluctance and minimum gap size.

<sup>5</sup> E-mail Marco Calviani, 16/01/2019



## 2.2. Optimisation of magnet yoke geometry

The various aspects of the coil and yoke dimensions were considered with the intention of increasing the integrated magnetic flux in the core. The benefits to the magnetic circuit from a change to a given dimension is then traded off against the additional cost or increase in engineering complexity. A recommendation for the final dimensions based on this study is then made.

The figure of merit in comparing the effect of changing aspects of the magnet is taken to be the B-field along the beamline axis through the magnetic iron, as shown by the black dashed line in Figure 10. At the same time, it was checked that a similar field integral is obtained throughout the whole magnet core.

An example of the field along this line is given in Figure 11. The B-field at either end of the magnet core is lower than that in the centre; this is primarily because the flux is compressed through the coil itself and then spreads out along the beam axis in the core. In addition some flux short-circuits around the coil through the air at one end and the proximity shielding at the other – this issue is addressed in section 2.2.4 below.

The general approach taken in optimising the geometry was to:

- reduce the reluctance of the magnetic circuit so that more magnetic flux was generated for a given coil size,
- increase the reluctance of alternative flux routes such that more flux preferentially travels through the magnet core.

This process was completed with two different baseline geometries. Initially it was based on the geometry as described in documentation from CERN supplied in 2018 and on the assumption that a 1.8T field should be achieved on the beamline axis.

The second baseline geometry, which is used in the iterations described below changed the initial geometry by raising base of the magnet iron; this was because it was realised that there was no need for the magnet core to extend so far below the beamline. In addition, it was decided that it was preferable to operate at a lower B-field and avoiding the need for water-cooling to de-risk the magnet operation. The power of the magnet was therefore limited to 4kW.

The results from the first iteration were presented at CERN in March 2019 and those from the second iteration are discussed in detail below.

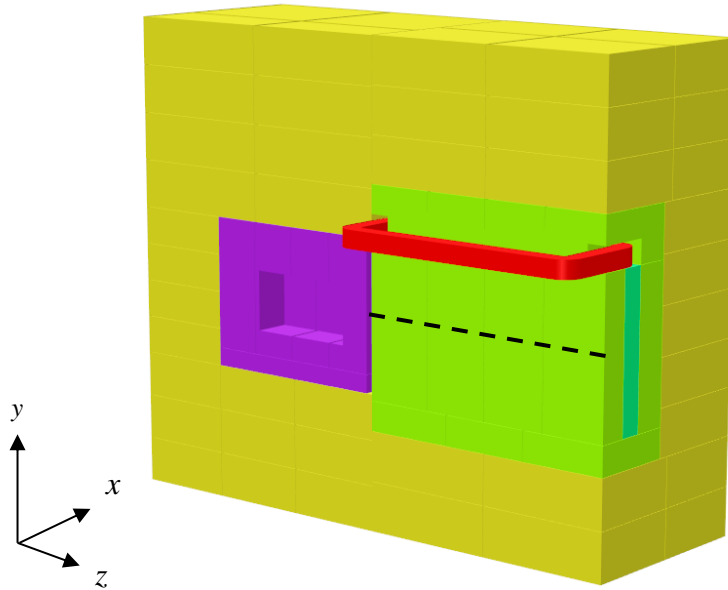


Figure 10: Magnetic model showing the beamline axis along which the field is considered as a black dashed line

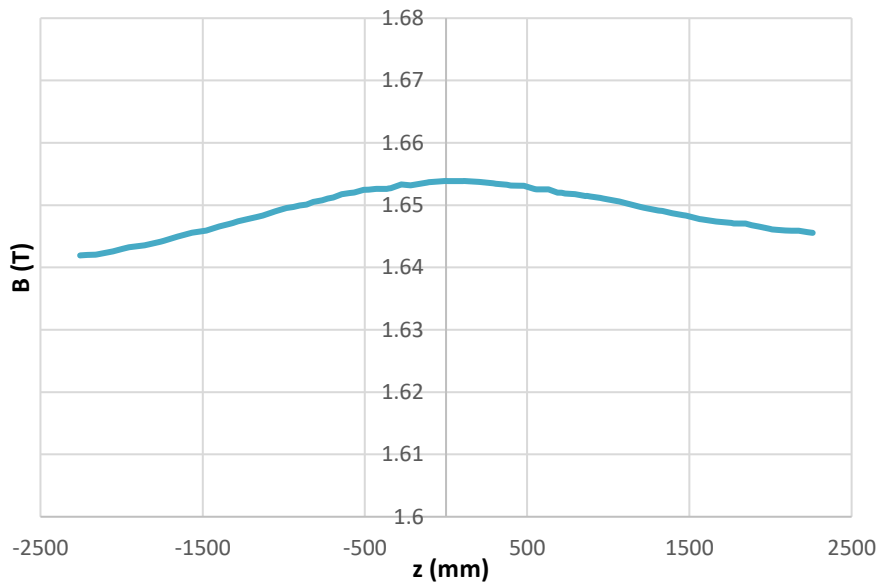


Figure 11: Example of B-field along the beamline

### 2.2.1. Stainless Steel pillar

Some of the flux, which would ideally travel down the magnet core, short-circuits across the stainless steel pillars on either side of the core. The width of this pillar was increased to increase the reluctance of this path and encourage more flux to follow the desired magnetic circuit.

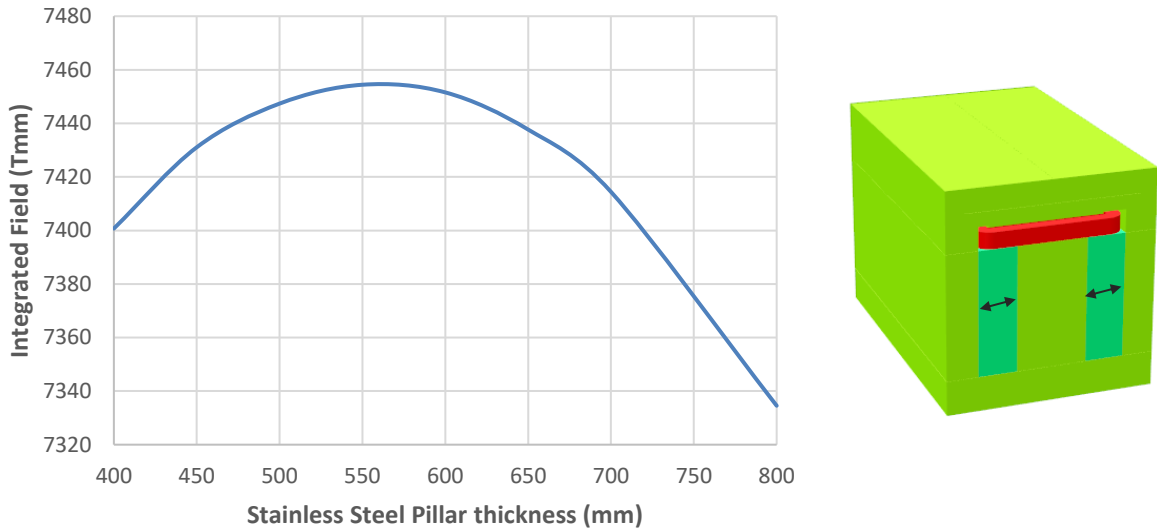


Figure 12: Left: Impact of stainless steel thickness on the integrated field along the beamline, Right: Stainless Steel thickness dimension

### 2.2.2. Magnetic iron return path

The magnetic iron return path (through the horizontal base, the outer vertical return section and the horizontal top) are sized in the baseline to be the same total width as the core. As the core has such a high flux, considering the magnetic iron in isolation, the reluctance of the path could be reduced if the return path were widened such that the field in those region were lower.

The most significant change came from increasing the width of the vertical return; this is due to it having the longest length as seen by the flux and therefore the greatest impact on the total path reluctance. However, in reality the magnetic iron is surrounded by a huge volume of cast iron – much of the return flux therefore returns through the cast iron at a very low B-field. So it was found that although increasing the thickness of the magnetic iron return was of some benefit, in reality the benefit is insignificant.

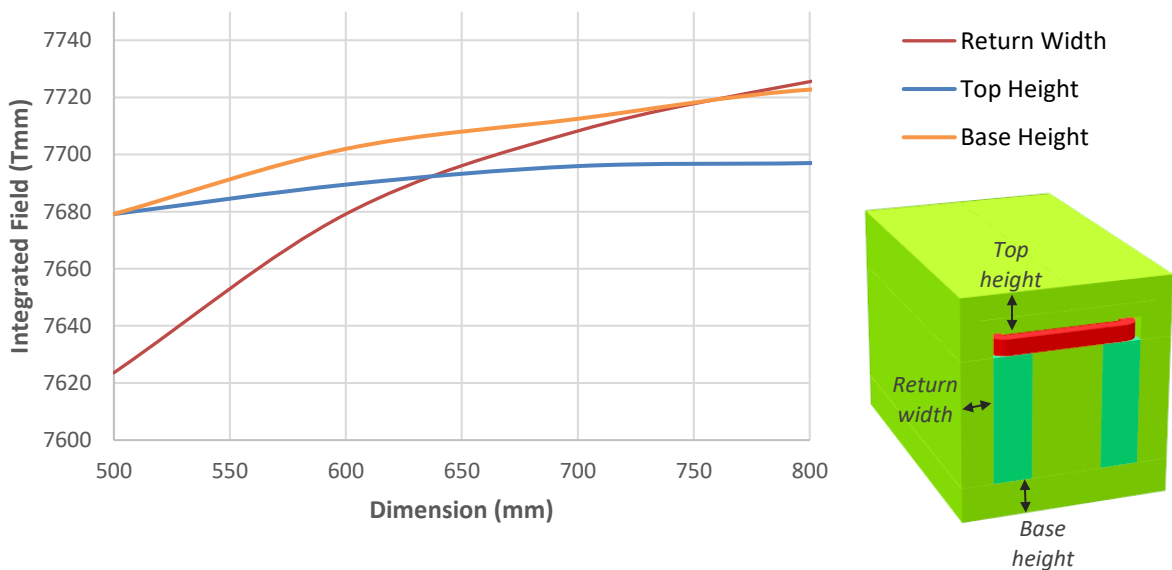


Figure 13: Impact of the dimensions of the magnet iron return path on the Integrated B-field along the beamline

### 2.2.3. Varying gaps in magnetic iron

Section 2.1.4 discussed the importance of the size of the gaps between the magnetic iron blocks, and how these gaps were derived from manufacturing tolerances and alignment accuracy. This was considered because the manufacturing tolerances often have a large impact on the final gap size; however it is more expensive to have shielding blocks made to tight tolerances. It is clear from Figure 14 that the size of the horizontal gaps has a far greater impact on the integrated field along the beamline than vertical gaps. The horizontal gaps are essentially only impacted by the manufacturing tolerances (the blocks are assumed to be well aligned due to settling under gravity).

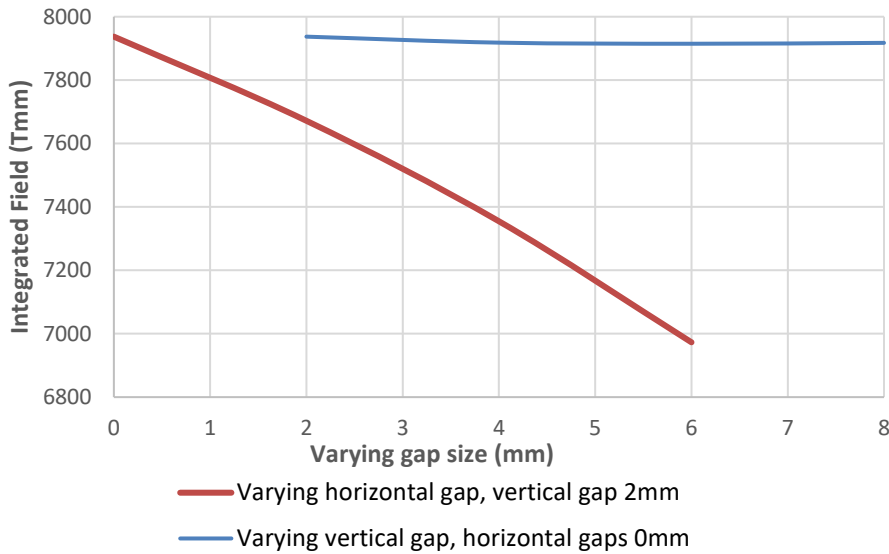


Figure 14: Impact of gap sizes on the integrated B-field along the beamline

### 2.2.4. Reducing stray field at coil ends

At either end of the magnetic iron, some of the flux short-circuits round the coil rather than taking the desired route through the magnetic circuit, as shown in Figure 15. On the target end it could even raise the stray field across the target. This could potentially be prevented in one of two ways – either by modifying the bunker shielding or by modifying the magnetic iron. These are discussed below.

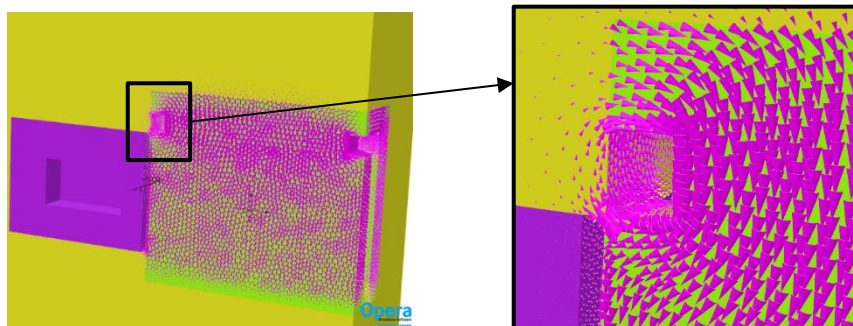


Figure 15: Magnetic flux short-circuiting around the coil. Flux shown by purple arrows

### 2.2.4.1. *Modifying the proximity shielding and bunker shielding*

The reduction in field at the upstream end of the magnetic iron, closest to the proximity shielding, is more significant than at the downstream end. This is because the reluctance of the path through the cast iron proximity shielding is lower than the path through air at the downstream end. Stainless steel has a lower permeability than cast iron and so it would be beneficial to replace some of the cast iron in this region with stainless steel.

Four variations were considered:

- the baseline where the whole of the proximity shielding and the bunker shielding was made from cast iron
- a “Half Cut” version where the height of the existing gap between the proximity shielding and the magnetic iron was increased to extend to the height of the coil
- “Simple SS (Stainless Steel) blocks” – in this version the bunker shielding block and proximity shielding block closest to the coil are replaced with stainless steel
- SS (Stainless steel) spacers were placed between the magnetic iron and the proximity shielding.

These variations are shown in Figure 16.

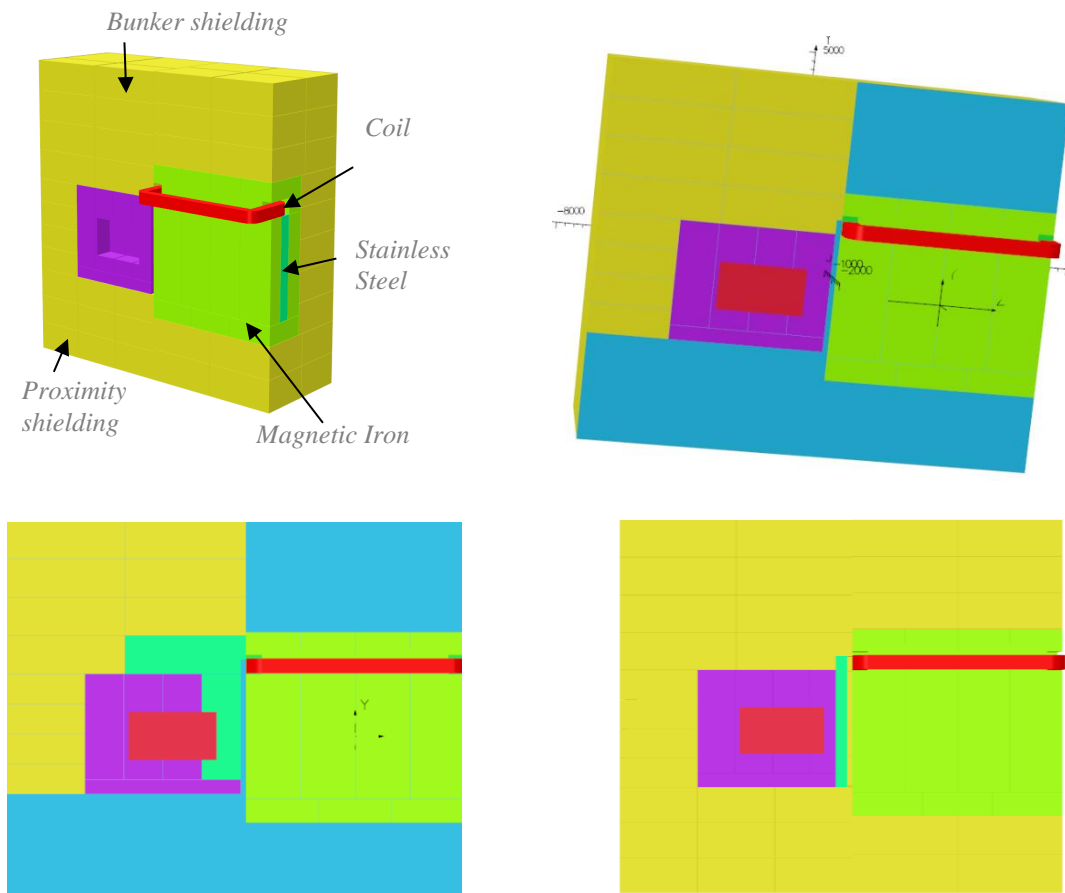
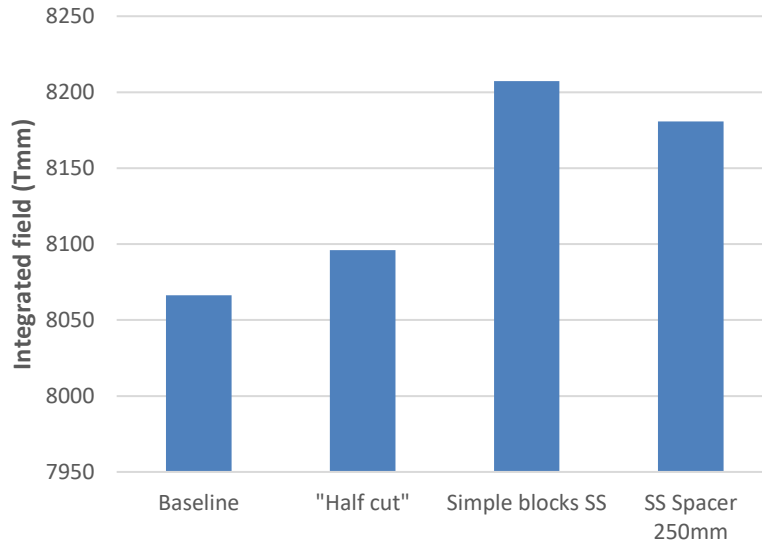


Figure 16: Modifying the bunker and proximity shielding to prevent flux loss on the beamline: Top left: Baseline. Top right: “Half cut”. Bottom Left: Simple SS blocks. Bottom right: SS spacer



**Figure 17: Impact of modifying the proximity and bunker shielding on integrated field**

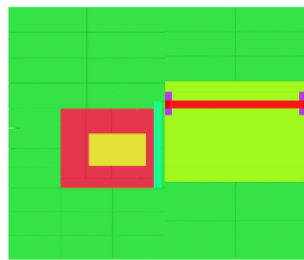
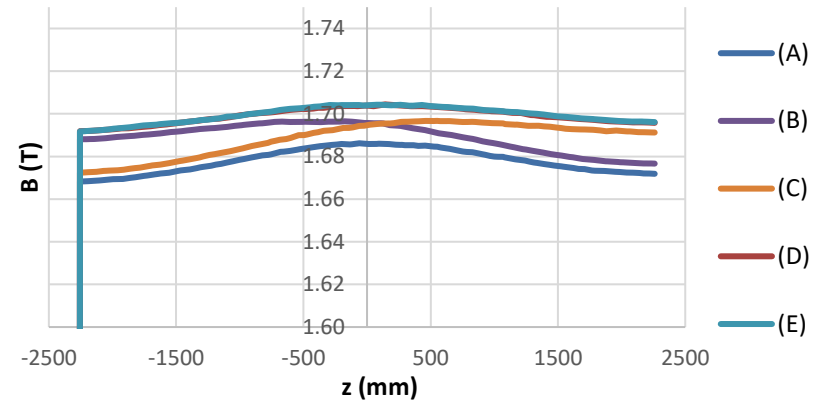
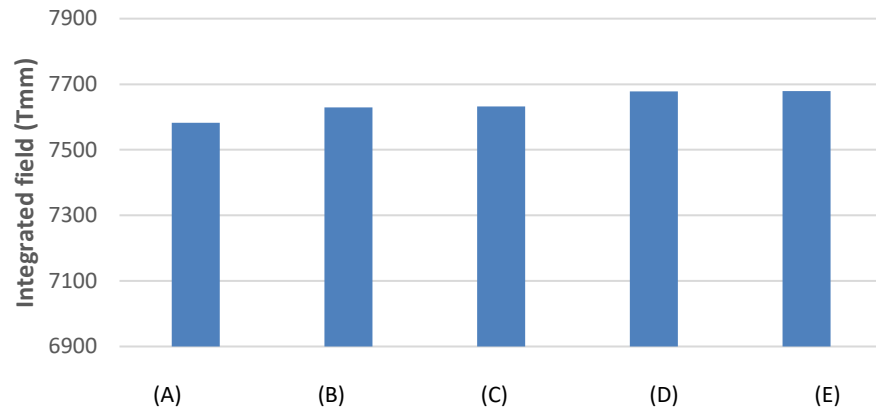
This study showed that modifying the materials used in this region was one of the largest gains on the integrated field that could be made without increasing the coil size. The choice of design must take into account the engineering effort and the manufacturing costs involved in changing the design of the proximity shielding; it is recommended that this is seriously considered and either the Simple SS blocks design or the SS spacer design is adopted.

As such, the baseline model on which the rest of this report is based, adopts the “SS Spacer” design shown here.

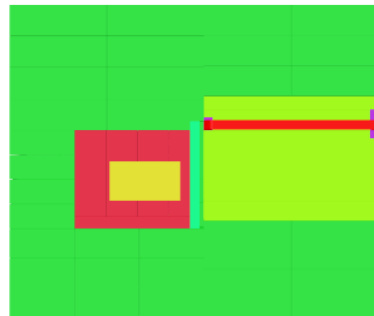
N.B. This study was done using a previous baseline model in which the magnetic iron extends equally above and below the beamline.

#### **2.2.4.2. *Modifying the magnetic iron***

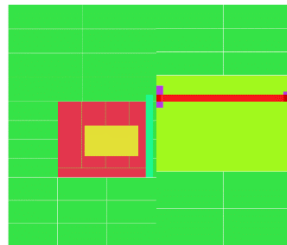
A further study was done with the new baseline (incorporating the SS Spacer design) to look at whether the magnetic iron could be modified in the region of the coil ends in order to reduce the flux short-circuiting the coil. The variations considered and the results are presented below in Figure 18; they show that the simple geometry initially used is the optimum, although there is little loss for the geometry adopted for gas cooling.



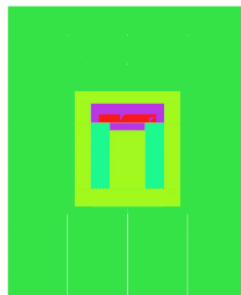
(A) Remove material above and below coil at  $Z_{min}$  and  $Z_{max}$



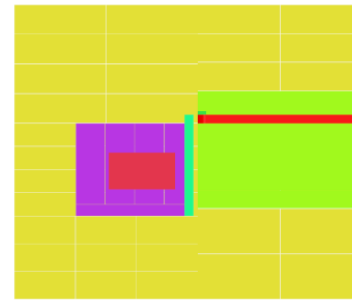
(B) Remove material above and below coil at  $Z_{min}$



(C) Remove material above and below coil at  $Z_{max}$



(D) Remove material above and below coil at  $Z_{max}$



(E) Baseline

Figure 18: Top left: Integrated field comparison. Top right: B field on axis comparison. Bottom: Variations considered for modifications to magnet iron.

### 2.2.5. Reducing compression of flux lines through the coil

As the magnetic flux passes through the coils, it is compressed along the horizontal axis z. This results in a high magnetic field at the height of the coil, and a correspondingly high reluctance in this region. This is the highest field region in the magnetic circuit; the magnetic iron is nearing saturation and so this small distance in the magnetic circuit is a disproportionately high fraction of the total reluctance of the magnetic circuit.

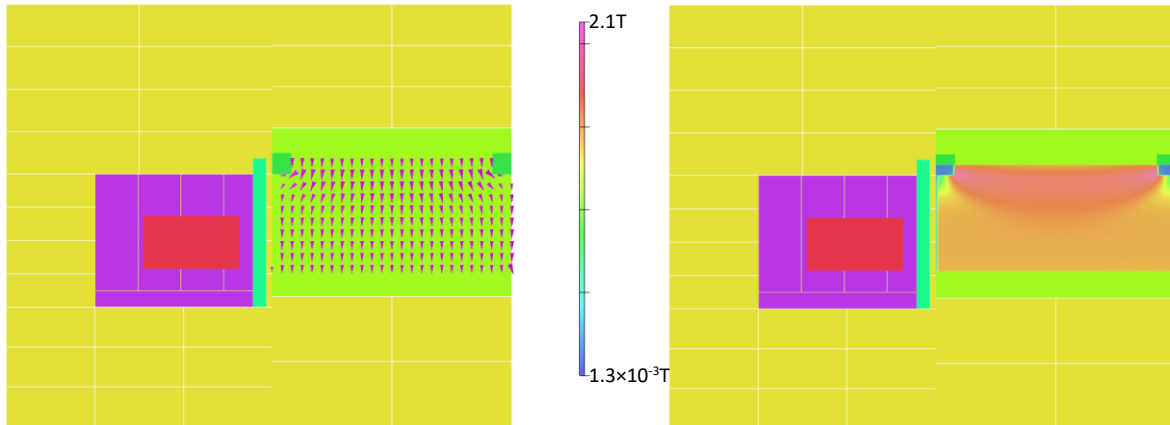


Figure 19: Compression of magnetic flux through the coil

If the coil could overhang the ends of the magnetic iron, rather than having to remove magnetic iron to accommodate them, the overall reluctance of the magnetic circuit could be significantly reduced.

At the downstream end of the magnetic iron, this is not possible as the coil would interfere with the helium container. At the upstream end of the magnetic iron this may be possible, however the mechanical restrictions, such as impact on assembly of the target shielding, need careful consideration. The current design of the target shielding allows the target and its proximity shielding to be removed without disturbing the rest of the shielding (including the coil and magnetic iron) and this should be maintained. It is possible that there is some scope of overhanging the coil at the upstream end slightly; this has not been evaluated at this stage, but may be worth exploring in the future.



## 2.3. Optimisation of Coil Geometry

### 2.3.1. Coil packing factor

The coil packing factor will usually be in the range 90-99% in an Aluminium strip coil and 60-70% in a copper wire coil; this is significantly lower in copper due to the additional need for insulation as well as the cooling channel. In either case the packing factor will depend on the coil size and aspect ratio, and the spaces between strips/wires will be filled with insulation. If the copper coil were wound in the same way as the aluminium coil, with a similarly high packing fraction, it would need insulating material between the individual strips. This insulating material would be affected by radiation. It would also significantly reduce the thermal conductivity in the direction perpendicular to the strips, making this design less suitable for gas cooling.

The results from modelling this range of packing factors showed that it has very little outcome on the integrated B-field along the beamline. This is consistent with the results for changing the current density in this range.

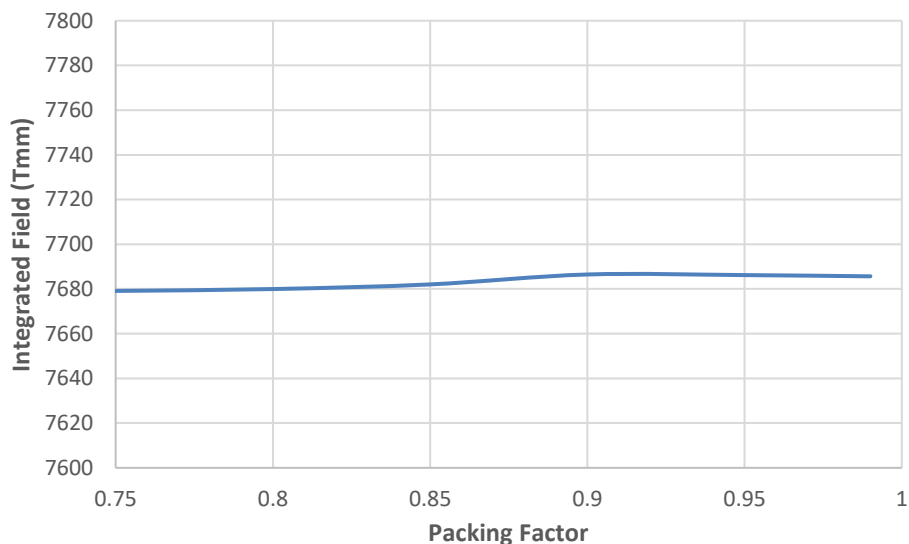


Figure 20: Impact of packing factor on the integrated B-field along the beamline

### 2.3.2. Coil bend radius

The magnet core in the yoke is a simple rectangle for ease of manufacture. The dimensions are limited by the internal dimensions of the coil; a larger coil bend radius results in smaller magnet yoke core. This section is the narrowest of the magnetic loop and therefore has the highest field region and the highest reluctance. When the internal dimensions are reduced to allow for an increased coil bend radius, the reluctance of this region is increased. This results in a decrease in integrated B-field along the beamline access with increasing bend radius, see Figure 21.

The range of realistic bend radii for this coil made from Aluminium strip would be 50-100mm, with the manufacturer advising that the 100mm bend radius would be easier to manufacture. There is comparatively little gain in integrated field in having a tight bend radius; therefore in this case it makes sense to follow the manufacturer's recommendations and allow a 100mm bend radius.

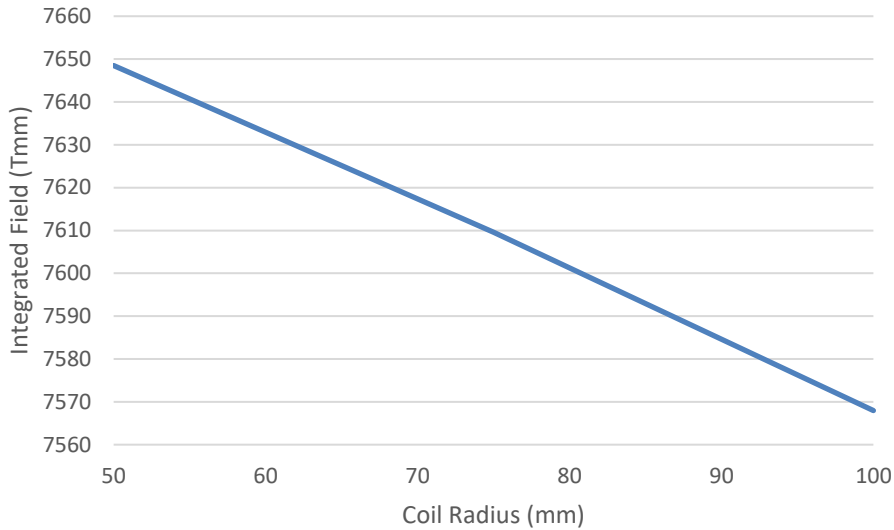


Figure 21: Impact of coil radius on the integrated B-field along the beamline

### 2.3.3. Sizing the coil: Current density, aspect ratio and Ampere-turns

The current density, aspect ratio and ultimately the number of ampere-turns were traded off to find the optimum solution. The coil is sized such that it operates at 4kW to allow for gas cooling only; the power is an output of both the current density and the number of ampere-turns.

If a coil is specifically sized to be operated at a current density of 0.35A/mm<sup>2</sup> with a given number of Ampere-turns, we see that initially the integrated field along the axis steadily increases with increasing ampere-turns. However as the coil cross-section increases, the coil is encroaching on the available iron in the magnetic circuit and therefore increasing the reluctance of the circuit. The results is that beyond 300,000 ampere-turns, increasing the size of the coil actually results in a lower integrated field on axis. This is shown in Figure 22.

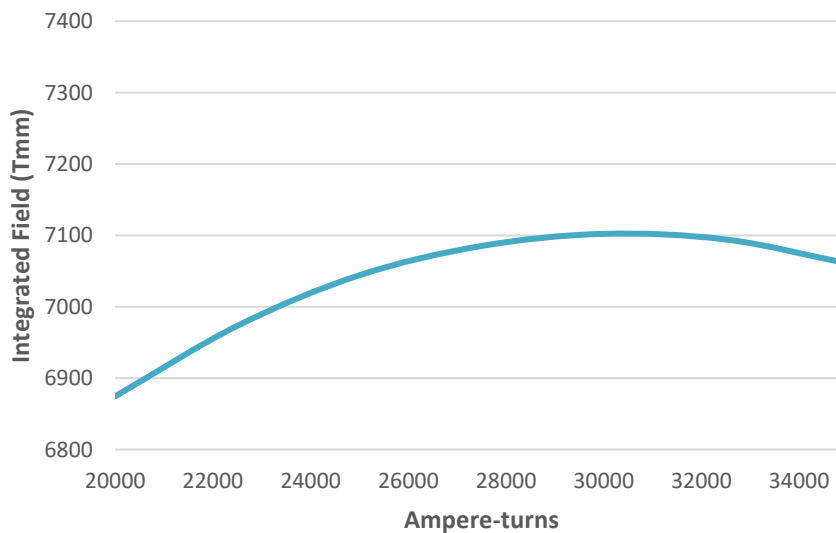


Figure 22: Integrated field with increasing number of ampere-turns, 0.35A/mm<sup>2</sup>

At higher current densities, the maximum number of ampere-turns available at 4kW is reduced. However, in many cases a higher magnetic field can be achieved for a given number of ampere-turns as the smaller coil cross-section impedes on the available magnetic iron less and therefore the reluctance of the magnetic circuit is reduced. This is illustrated in Figure 23, which shows the results for 0.45A/mm<sup>2</sup>. A 0.5A/mm<sup>2</sup> solution was also considered, however the 4kW power limit was found to give a maximum integrated field lower than the 0.45A/mm<sup>2</sup> solution.

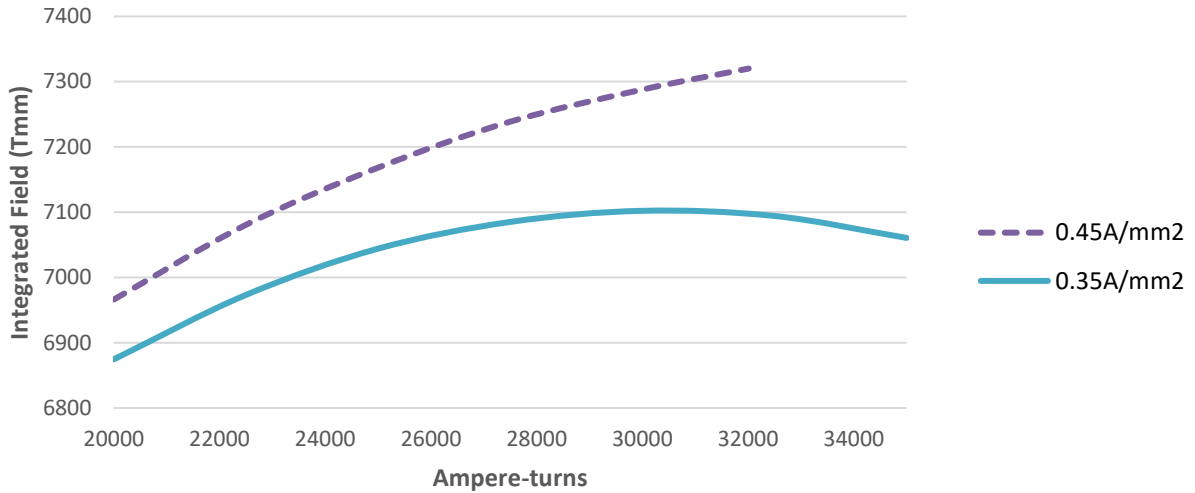


Figure 23: Integrated field with increasing number of ampere-turns, at 0.35A/mm<sup>2</sup> and 0.45A/mm<sup>2</sup>, with coil height 300mm

Next, the height of the coils was taken into consideration. Initially it has been assumed that the coils is 300mm high and the width of the coils is varied to achieve the desired cross-section. Further results were obtained for coils of heights 320mm and 340mm. These are shown in Figure 24. In this case it is seen that the integrated field can be slightly increased by moving to a higher, narrowed coil shape; however, the gain is small and this may not be the optimum solution in terms of heat dissipation and manufacturing the coil.

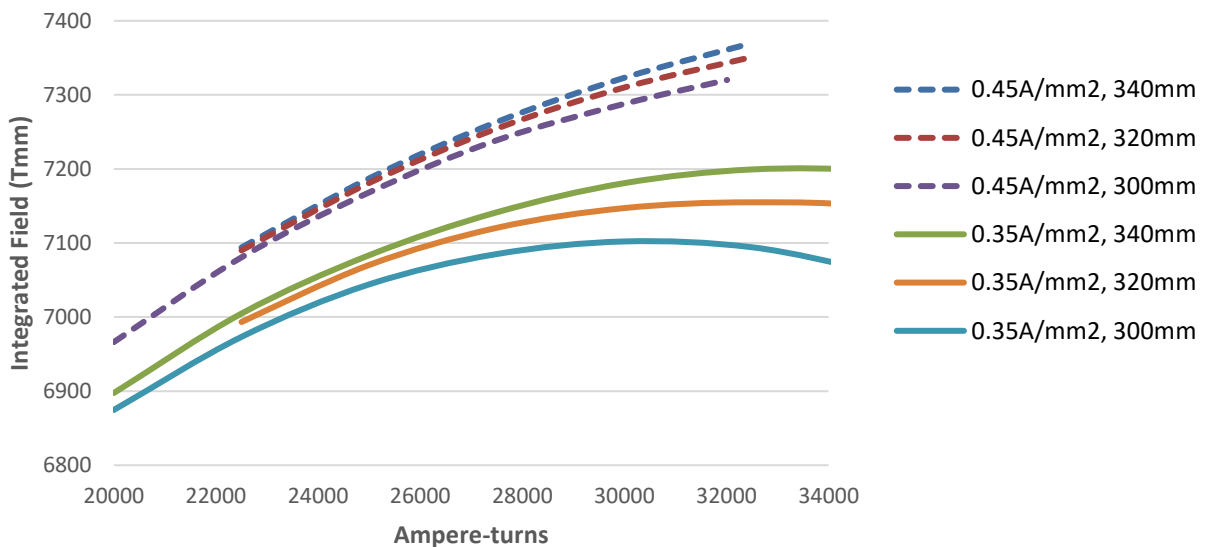


Figure 24: Integrated field with increasing number of ampere-turns, at 0.35A/mm<sup>2</sup> (solid lines) and 0.45A/mm<sup>2</sup> (dashed lines), and coils heights set to 300mm, 320mm and 340mm.

Finally the heat dissipation perspective is considered, focusing on the two coils with the optimum geometry for  $0.35\text{A/mm}^2$  and  $0.45\text{A/mm}^2$ , referred to as Coil A and Coil B for the remainder of this section, with details given in Table 2.

**Table 2: Coil parameters for Coil A and Coil B**

		Coil A	Coil B
<i>Current density for which the geometry is it optimised</i>	<i>A/mm<sup>2</sup></i>	0.35	0.45
<i>Ampere-turns at design current density</i>	<i>Ampere-turns</i>	30,000	32,013
<i>Coil height</i>	<i>mm</i>	300	300
<i>Coil width</i>	<i>mm</i>	318	264
<i>Power at design current density</i>	<i>W</i>	2806	4000

First of all the integrated field for a given power is compared with different coil shapes. Figure 25 shows that the integrated field achieved for a given power with both Coil A and Coil B is very similar, with Coil B generating only marginally better fields.

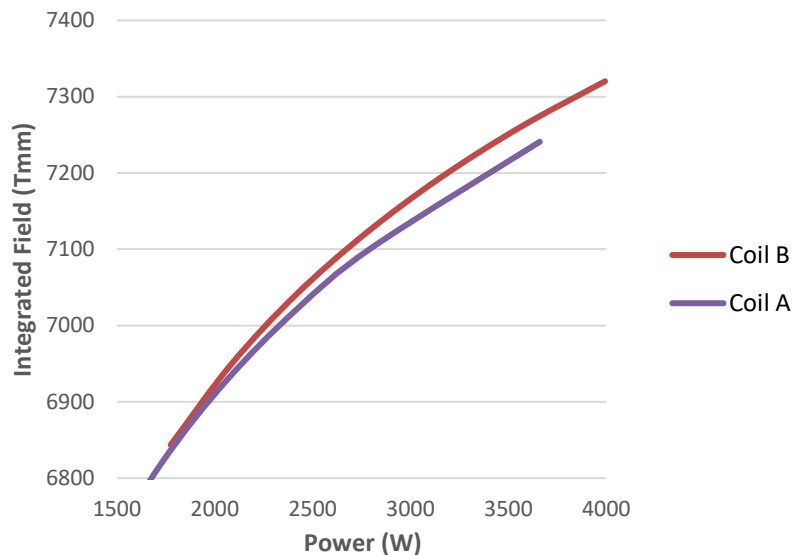


**Figure 25: Performance with power for Coil A and Coil B**

It should be considered that Coil A, with a larger outer surface, will be easier to cool and is therefore a safer design. For this reason the effect of ramping the current in Coils A and B are considered.

Figure 26 compares the effect of increasing the number of ampere-turns in the coil by changing the coil shape, and the effect of ramping the current in a given coil size. The dashed purple line shows integrated field when the coil is optimised for a given number of ampere-turns with a  $0.45\text{A/mm}^2$  current density (as shown above). The integrated field with the optimum coil at this current density, Coil B, is then shown when the current is ramped down by the dashed red line. The equivalent results with the  $0.35\text{A/mm}^2$  results and Coil A are then shown in blue and green.

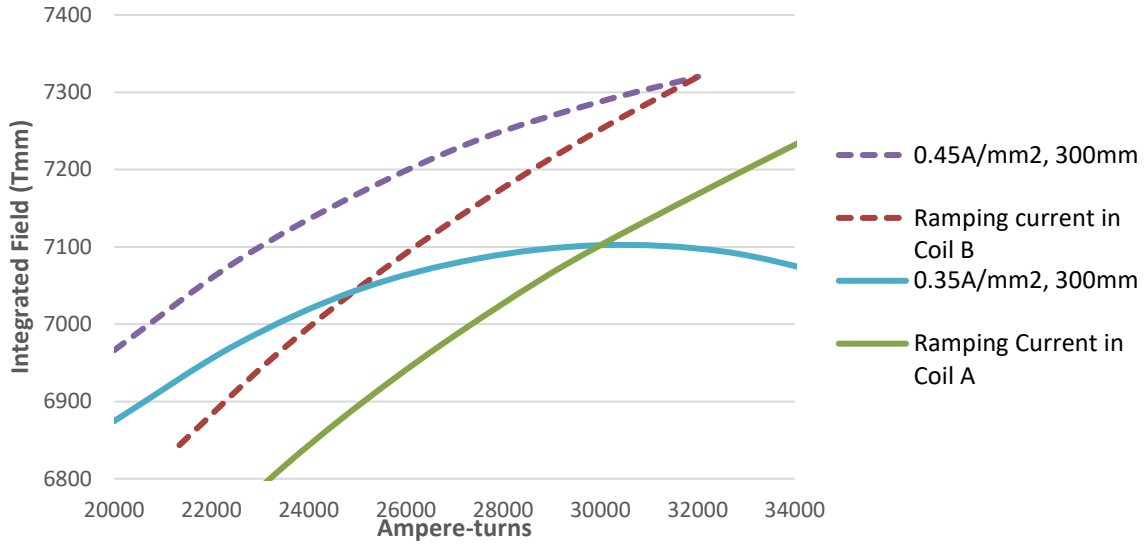


Figure 26: Performance of Coil A and Coil B with current ramping, compared to the performance of optimised coils for given current densities (as Figure 23)

It can be seen that in general, Coil B is generating a higher integrated field for any given number of ampere-turns. If in operation, there are found to be problems cooling Coil B, it could be operated at a lower current density,  $\sim 0.36\text{A/mm}^2$ , and still generate the same integrated field as Coil A operating at its design current density of  $0.35\text{A/mm}^2$  just with a lower number of ampere-turns. This is shown in Figure 27.

The optimum design magnetically is therefore Coil B. At this stage, the design of the cooling circuit is not far enough along to guarantee that this will be thermally stable – however it is generally assumed that  $1\text{A/mm}^2$  is a safe current density for air-cooled coils, and this design is still well below that limit. Initial calculations of the heat management are given in paragraph 5.3.2 and further analysis, including CFD for the complete cooling system of the target and target shielding system, will be carried out by CERN. In addition, if there are any issues, the coil can be run at a lower current density and still performs well.

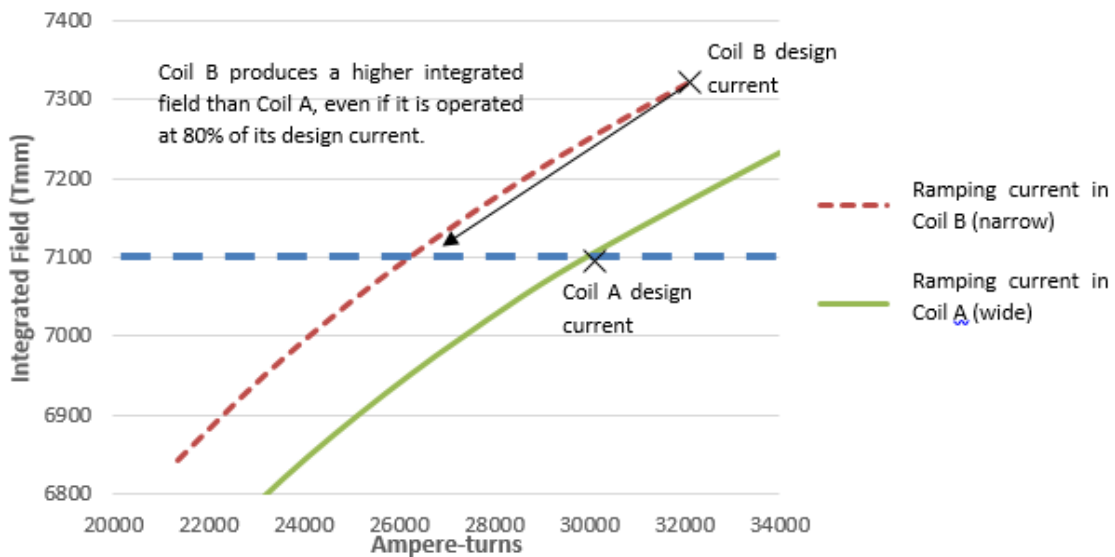


Figure 27: Performance of Coil A and Coil B with current ramping

## 2.4. Summary of magnet optimisation (Geometry & Performance)

Figure 29 summarises the results of all the variations discussed above, for ease of comparison. It is clear that some modifications make very little difference to the integrated field along the beamline, whereas others are more worthwhile.

The modification with the most impact is unmistakably the size of gaps between the shielding blocks. It is therefore important that these are well controlled during manufacture and alignment. In some cases there is little or no additional engineering effort required to apply the optimum solution (for example the width of the Stainless Steel pillars can easily be set at 550mm), in which case they should be applied. In others, such as coil radius, the optimum solution is not a significant improvement on the easier manufacturing/low risk route; in these cases it makes sense to keep the design simple and low risk.

The dimensions that are recommended to be changed as an outcome of the magnetic optimisation are given in Table 3.

The final baseline model with these changes implemented, as well as the details such as those relating to the cooling channels for Helium flow and the chimney for the services, gives an integrated field along the beamline of 7077Tmm and a maximum field of 1.57T. The field profile along the beamline is given in Figure 28.

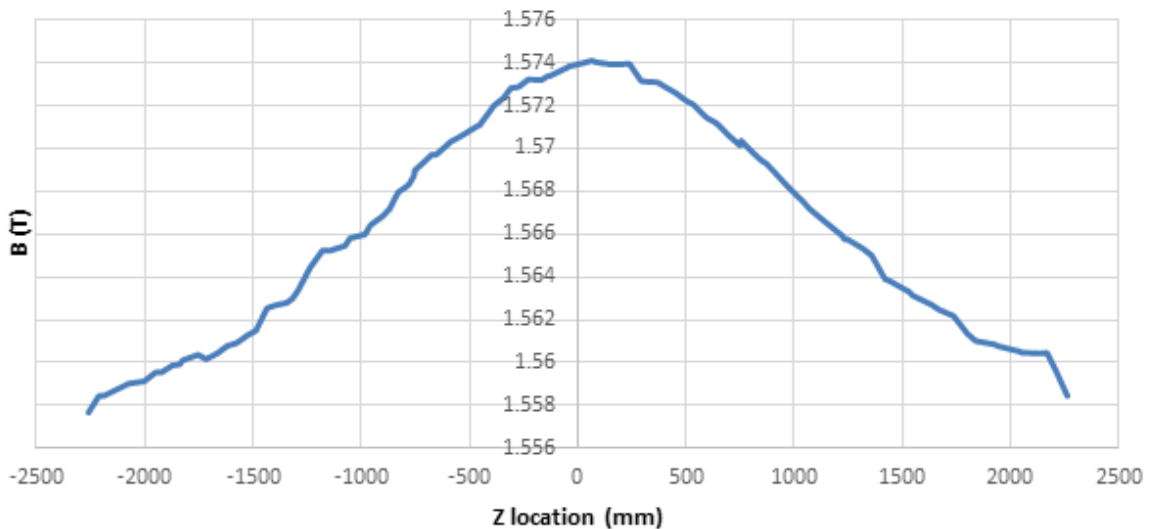


Figure 28: B-field profile along the beamline in final model

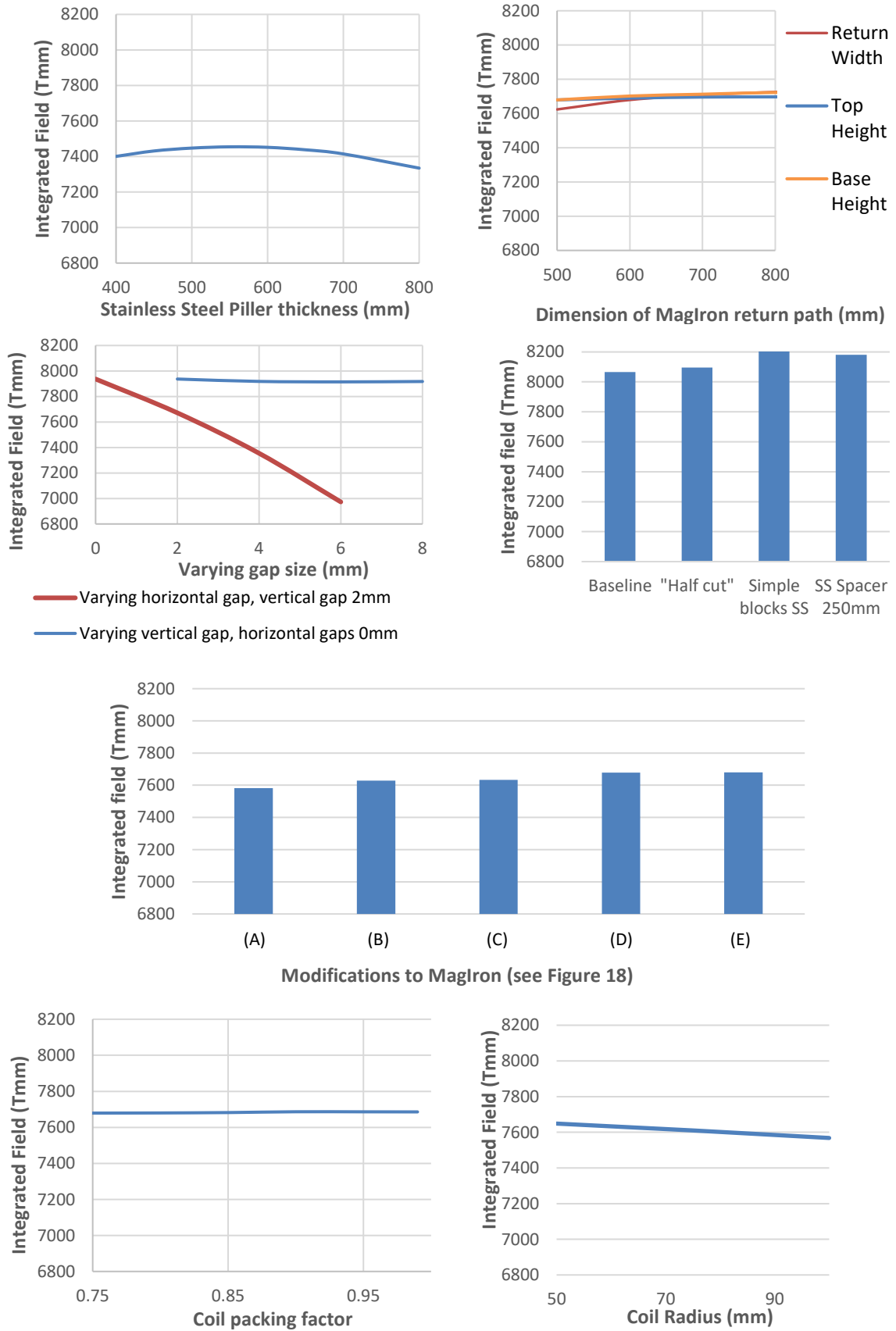
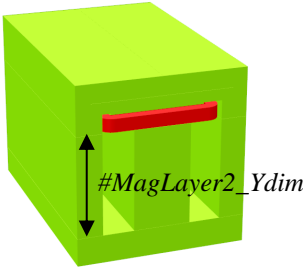
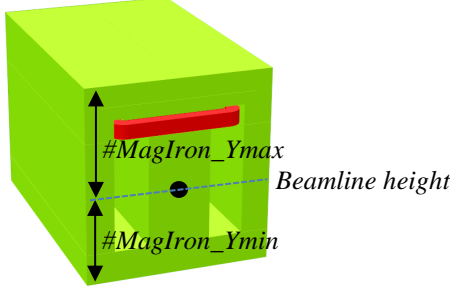
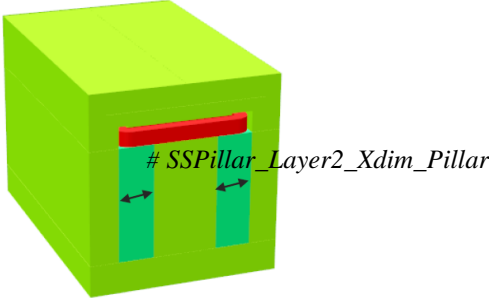


Figure 29: Comparison of effect of modifications

Table 3: Recommendations for dimensions changes based on optimising the magnetic circuit, also see Figure 74

Dimension		Original	Final
Height of active shielding area: #MagIron_Layer2_Ydim		2600mm	1800mm
Extent of magnetic iron above and below the beamline: #MagIron_Ymin #MagIron_Ymax		-1800mm 2170mm	-1000mm 2170mm
Width of the stainless steel pillar: #SSPillar_Layer2_Xdim_Pillar		400mm	550mm
All tolerances on gaps in magnetic iron yoke (includes Stainless Steel verticals) : #MagIron_XTolGap #MagIron_YTolGap #MagIron_ZTolGap  All tolerances on gaps in Cast Iron: #CastIron_XTolGap #CastIron_YTolGap #CastIron_ZTolGap	Gap naming conventions and table of inputs in section 2.1.4. <i>Size of gaps between blocks.</i>	0 0 0  0 0 0	Modelled as worst case: 0 2 0  Modelled as average: 10 10 10
Coil Dimensions	Final coil dimensions should be as described as Coil B in Table 2, in section 2.3.3. <i>Sizing the coil: Current density, aspect ratio and ampere-turns</i>		
Proximity Shielding Design	The design of the Proximity Shielding used in final results are based on the "SS Spacer 250mm" design described in section 2.2.4.  As described there, the use of more Stainless Steel in the proximity shielding and some bunker shielding would be beneficial.		



## 2.5. Forces

### 2.5.1. Forces on shielding

In order to calculate the forces on individual blocks in the shielding, a separate model was solved with each block being assigned a different material. As before, symmetry is applied in the YZ plane, so that only half the model is solved. This is shown in Figure 30 below.

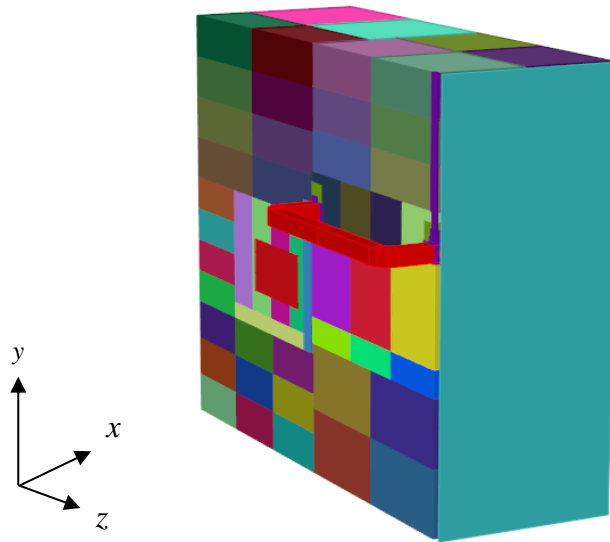


Figure 30: Final model with individual magnet and shielding blocks modelled in separate materials

The resultant forces are given in Table 4, Table 5 and Table 6. As is expected the highest forces are seen in the magnetic iron; forces of up to 900kN are acting to pull the iron together. There are also some significant forces seen in the shielding blocks and the proximity shielding, in particular close to the magnet iron where there are stray fields; these are much lower with a maximum force of 50kN.

Table 4: Forces on magnet blocks

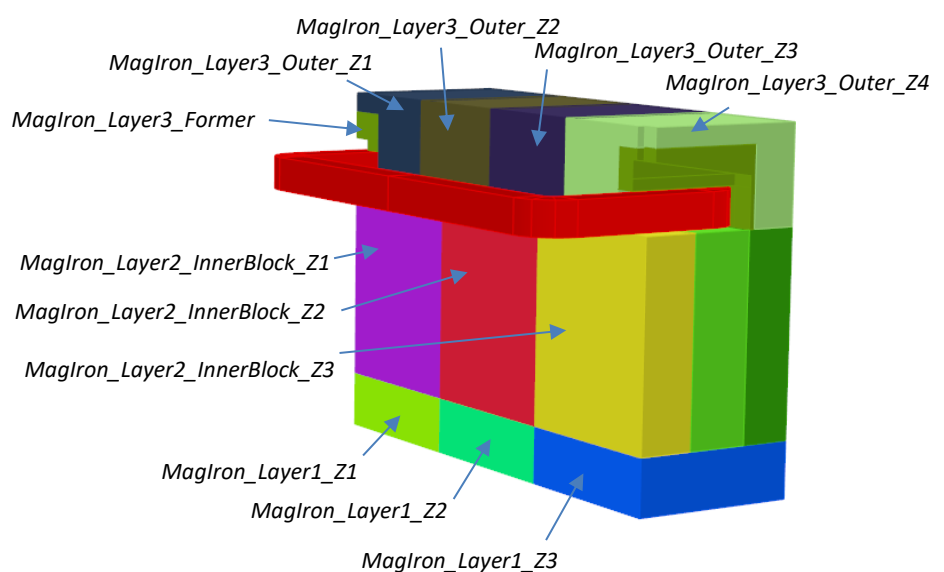
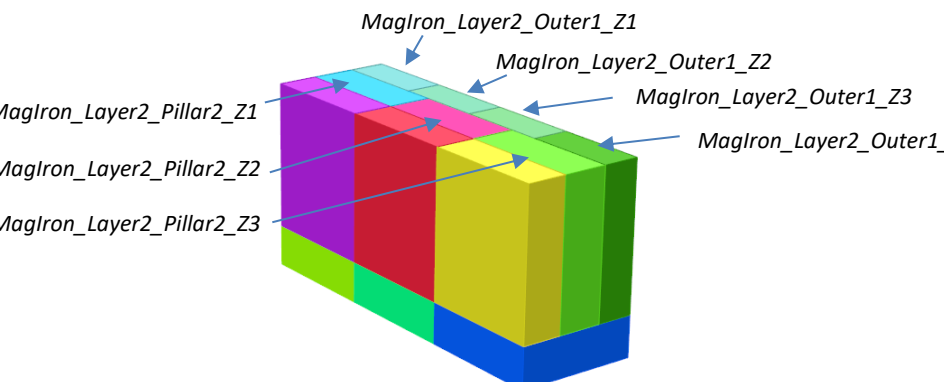
Block locations	Block Name	Resultant Forces (kN)			
		F <sub>x</sub>	F <sub>y</sub>	F <sub>z</sub>	
	MagIron_Layer1_Z1	18.0	811	-84.6	
	MagIron_Layer1_Z2	14.7	860	-13.7	
	MagIron_Layer1_Z3	14.7	871	-6.04	
	MagIron_Layer2_InnerBlock_Z1	35.3	163	-29.7	
	MagIron_Layer2_InnerBlock_Z2	24.8	352	-1.75	
	MagIron_Layer2_InnerBlock_Z3	35.9	163	-18.5	
	MagIron_Layer3_Outer1_Z1	-131	-733	-269	
	MagIron_Layer3_Outer1_Z2	10.29	-913	-97.8	
	MagIron_Layer3_Outer1_Z3	23.13	-898	1.83	
	MagIron_Layer3_Outer1_Z4	-112	-758	171	
	MagIron_Layer3_Former	29.8	-414	25.7	
		MagIron_Layer2_Pillar2_Z1	0.16	0.05	0.01
		MagIron_Layer2_Pillar2_Z2	0.12	0.03	0.00
MagIron_Layer2_Pillar2_Z3		0.15	-0.02	0.11	
MagIron_Layer2_Outer1_Z1		-239.97	142.41	-28.0	
MagIron_Layer2_Outer1_Z2		-292.43	139.19	-8.69	
MagIron_Layer2_Outer1_Z3		-279.61	136.99	-2.53	
MagIron_Layer2_Outer1_Z4		-215.40	126.49	-3.52	

Table 5: Forces on proximity shielding blocks and Helium vessel

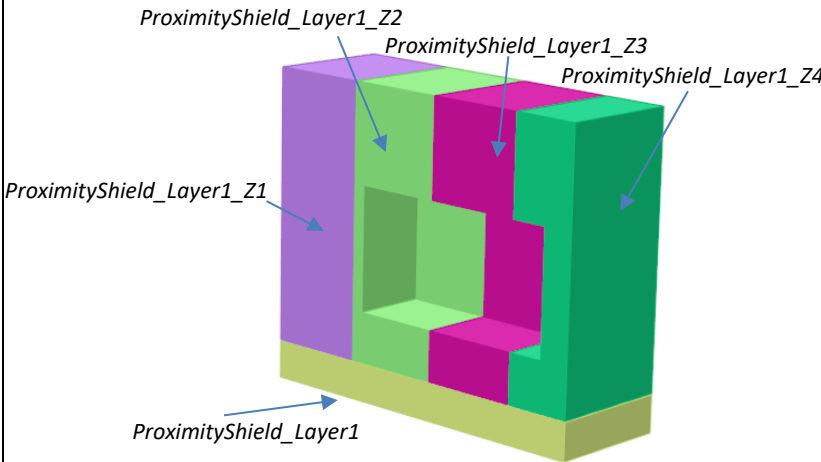
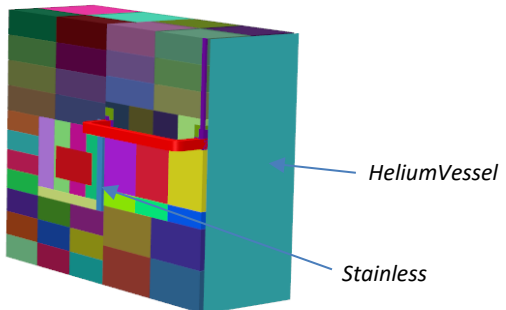
Block locations	Block Name	Material	Resultant Forces (kN)		
			F <sub>x</sub>	F <sub>y</sub>	F <sub>z</sub>
	ProximityShield_Layer1	Cast Iron	0.07	-0.06	0.02
	ProximityShield_Layer1_Z1	Cast Iron	0.10	0.18	0.00
	ProximityShield_Layer1_Z2	Cast Iron	0.11	0.77	-0.03
	ProximityShield_Layer1_Z3	Cast Iron	0.06	1.53	0.05
	ProximityShield_Layer1_Z4	Cast Iron	0.35	2.88	0.15
	HeliumVessel	Stainless Steel ( $\mu = 1.1$ )	$4 \times 10^{-3}$	$4 \times 10^{-4}$	$1.4 \times 10^{-2}$
	Stainless	Stainless Steel ( $\mu = 1.1$ )	0.02	0.06	0.07

Table 6: Highest forces on the bunker shielding

Block locations	Block Name	Materials	Resultant Forces (kN)		
			F <sub>x</sub>	F <sub>y</sub>	F <sub>z</sub>
	<i>USBS_Layer3_x3_Y1_Z1</i>	Cast Iron	2.56	-17.9	-8.97
	<i>USBS_Layer3_x3_Y1_Z2</i>	Cast Iron	3.64	-14.8	-0.27
	<i>USBS_Layer1_x3_Y2_Z1</i>	Cast Iron	2.47	18.4	-9.74
	<i>USBS_Layer2_Y4_Z1</i>	Cast Iron	-5.06	0.64	-21.0
	<i>DSBS_Layer2_Y1_Z2</i>	Cast Iron	-1.23	3.50	50.3
	<i>DSBS_Layer2_Y2_Z2</i>	Cast Iron	-0.42	-3.60	22.9
	<i>DSBS_Layer2_Y3_Z2</i>	Cast Iron	-0.12	0.80	13.0
	<i>DSBS_Layer2_Y4_Z2</i>	Cast Iron	-0.09	17.2	23.3
	<i>DSBS_Layer3_x2_Y1_Z2</i>	Cast Iron	0.54	-10.7	46.5
	<i>DSBS_Layer3_x3_Y1_Z2</i>	Cast Iron	0.53	-3.19	20.90

### 2.5.2. Forces on coil

The coil experiences a total force of 16.4kN upwards and 85N in Z. For comparison, the self-weight of the coil body is 2700kg.

The forces in X and Z axis are balanced or nearly balanced due to symmetry, so forces on coil sections should be considered. These are plotted in Figure 31. It should be noted that these forces are dependent on the position of the coil in the gas channel in the former.

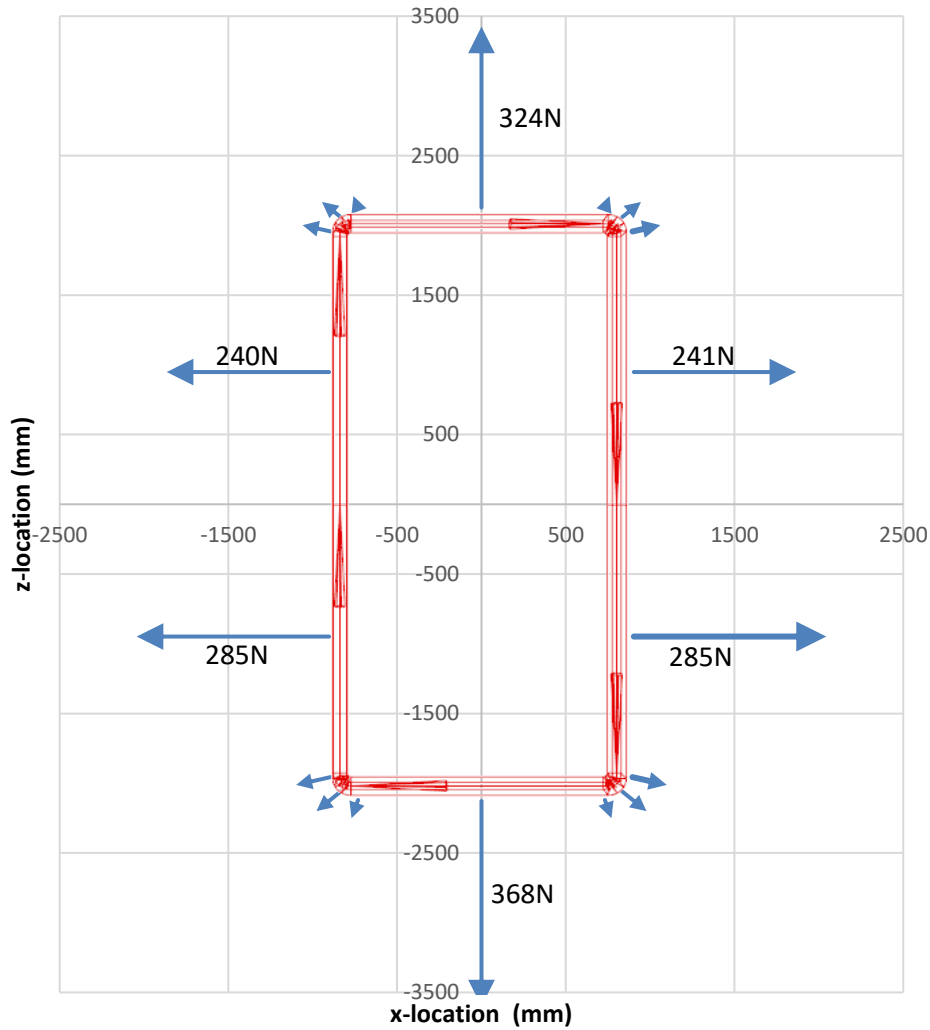


Figure 31: Forces on the coil

## 2.6. Stray fields

The stray fields from beyond the bunker shielding and inside the target area are highly dependent on the magnetic properties of the components in those regions. The following results are based on the assumption that there are no components with magnetic permeability greater than air.

### 2.6.1. Stray fields from within the target area

In the target region, the maximum B fields are seen on the outer edge of the target region (the internal surface of the proximity shielding) of the order of  $1.5 \times 10^{-2} \text{T}$ . These high field regions are in the region of the gaps in the proximity shielding blocks (Figure 32). The field in the bulk of the target region is around  $5 \times 10^{-4} \text{T}$  (5 Gauss), as shown in Figure 33. These stray fields are as low as they are due to the presence of the stainless steel spacers between the target and magnet regions.

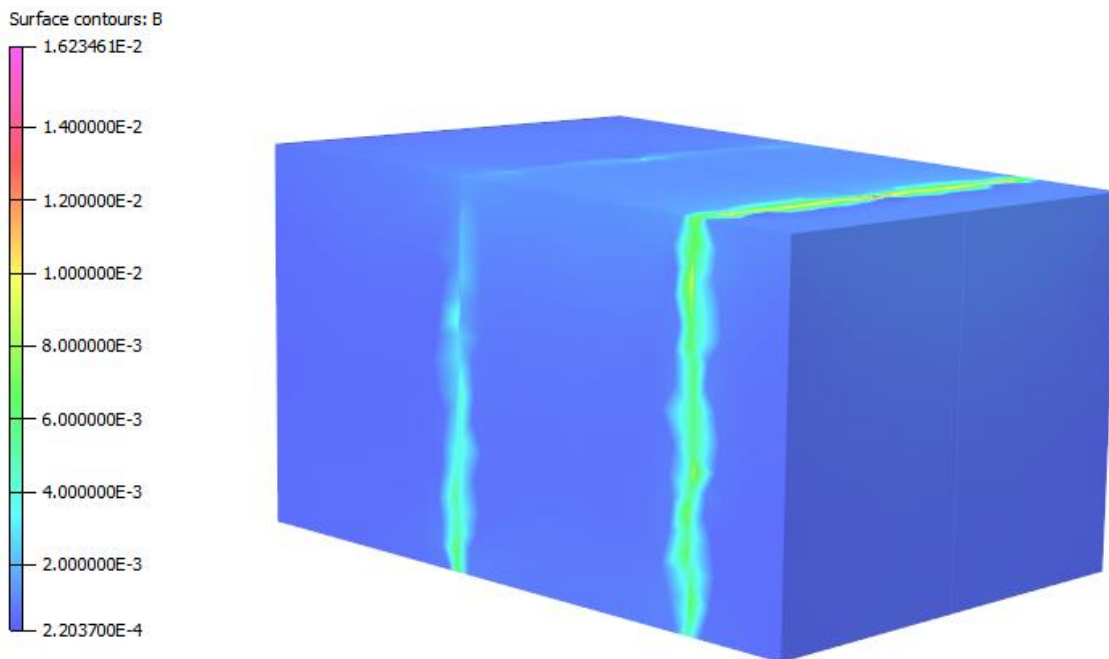


Figure 32: Internal surface of the target region/proximity shielding

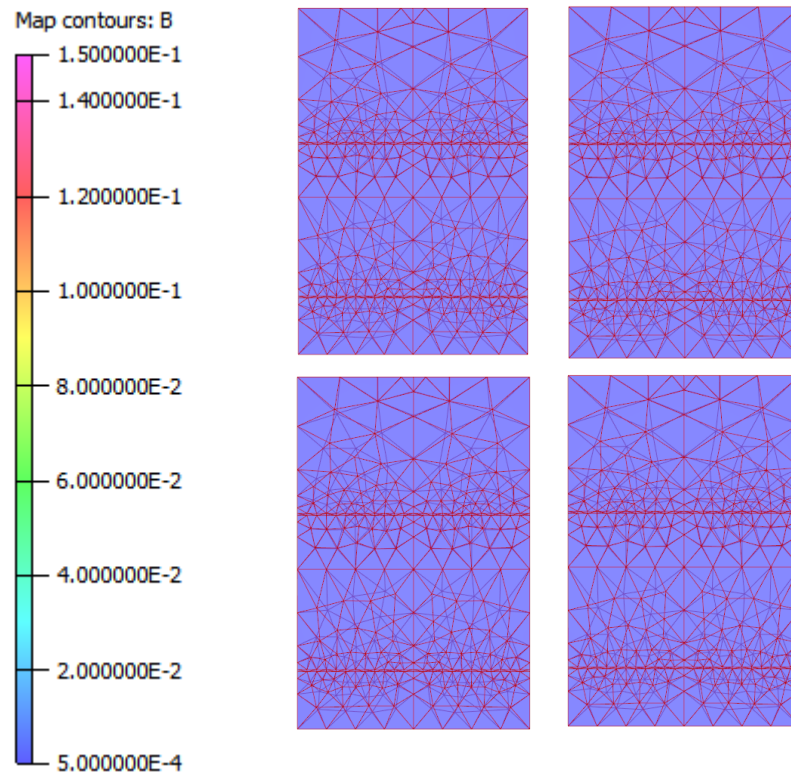


Figure 33: Field maps through the target region at 200mm height intervals (top left at 200mm height, then top right, bottom left and bottom right) overlaid over the target region mesh. B-fields on the outer edge reach  $1.4 \times 10^{-1} \text{T}$  and everywhere else is  $\sim 5 \times 10^{-4} \text{T}$  (5 Gauss)

### 2.6.2. Stray fields outside of the target bunker shielding

On the surface of the outside of the shielding (including the target shielding and the magnetic iron) the highest fields are 2.2T. These are seen on the outside of the magnetic iron; see Figure 34. It can be seen that away from the magnetic iron, over the vast majority of the surface of the bunker shielding, the fields are less than  $5 \times 10^{-4} \text{T}$  (5 Gauss). Figure 35 shows the fields 1m from the surface of the bunker shielding – at this distance, the maximum field seen is below  $5 \times 10^{-4} \text{T}$  (5 Gauss) even in the vicinity of the magnetic iron.

To give an idea of magnetic fields which need particular consideration:

- Static magnetic fields of less than  $5 \times 10^{-4} \text{T}$  (5 Gauss) are usually considered harmless. Above this local safety rules could apply – such as requiring safety signs and preventing access to people with pacemakers.
- Above  $3 \times 10^{-3} \text{T}$  (30 Gauss) magnetisable materials may be accelerated and present projectile hazards
- Biological hazards, such as transient sensations of vertigo or nausea, would not be expected until the magnetic fields were in excess of 2-4T – which is not reached anywhere in this facility.

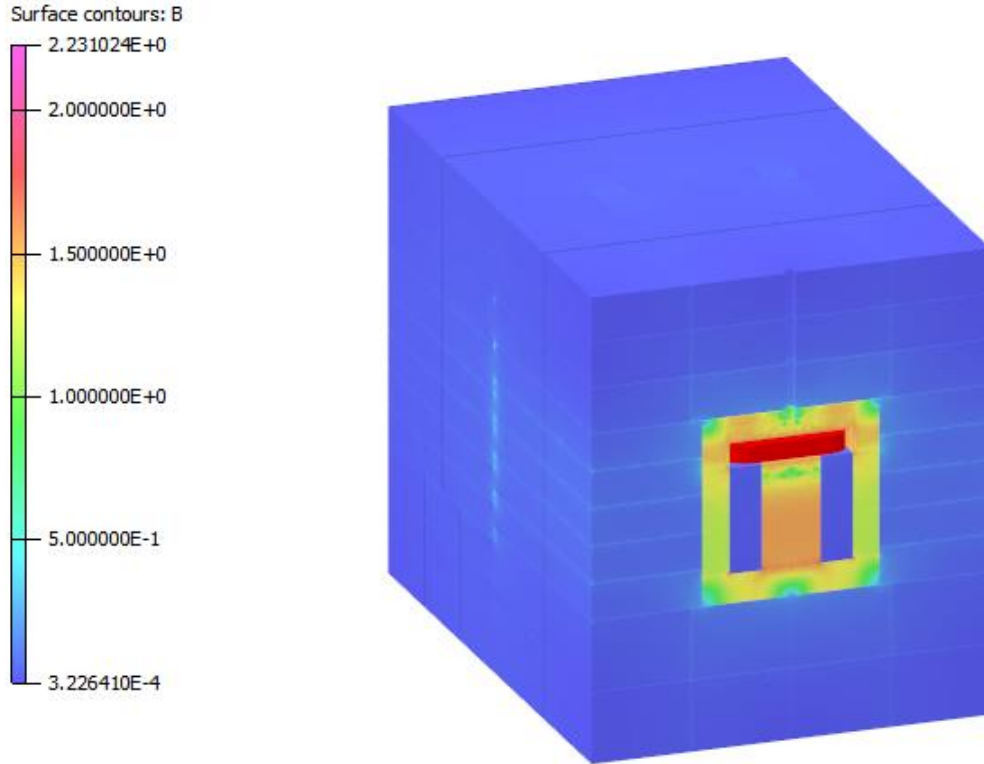


Figure 34: Fields on the outside of the shielding of the target complex

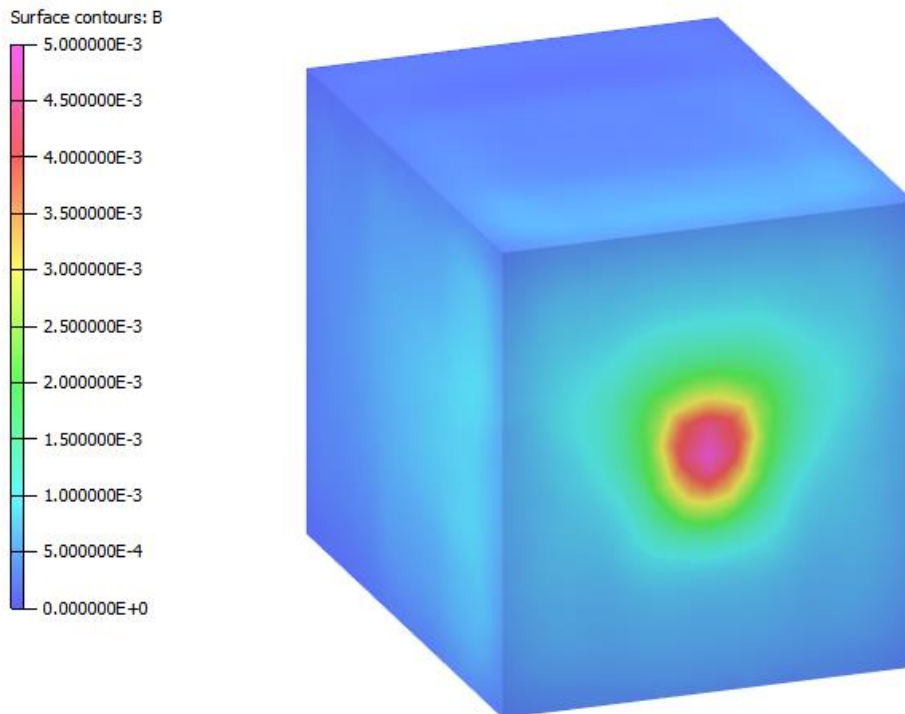


Figure 35: Fields at 1m from the surface of the shielding of the target complex



### 3. Assessment of hysteresis effects after multiple energisation

The baseline model for the magnetisation of the target shielding has been solved in Opera's Elektra Transient module with full BH curves to model the hysteresis effects – primarily to calculate resultant forces after energisation of the magnet. There is some concern that residual forces could cause difficulties when dismantling the components within the target shielding.

However, it is highly recommended that the magnet coil in the target bunker is powered to incrementally lower currents in opposite directions prior to any dismantling of the system. For example, it would be powered to 100%, then -90%, 80%, -70% etc of its nominal current down to 10% - this would act to remove residual forces remaining after normal operation and would greatly improve the safety of dismantling. The ability to do this must be built in to the design of the coil (either the current leads must be easily accessible in order to swap them over or a power supply capable of powering the magnet in both directions should be used). This is standard practice in other magnets of this scale. The principle of reducing the residual magnetisation flux (B) by alternating the current (proportional to the induction H) is shown in Figure 36<sup>6</sup>.

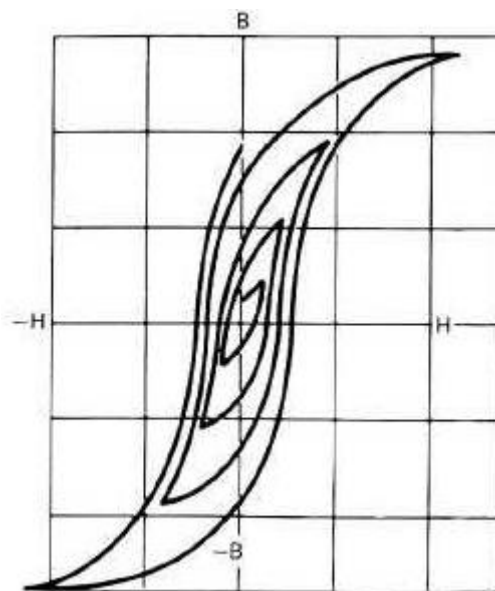


Figure 36 Demagnetisation of iron by alternating the applied field H (proportional to current I)

The BH curves used in the hysteresis modelling are given in Appendix C.

In order to generate results from a transient hysteresis model, the accuracy of the model had to be reduced in order to allow it to solve in 5 days, this was done by increasing the mesh size by a factor of three. For comparison the static model solves in just over 1hr. When the results of the transient model and the static model were compared, it was decided that the error in the transient model is unacceptable and therefore the results are not presented here. In order to achieve a similar level of

<sup>6</sup> Nondestructive Inspection Methods Manual, [http://chemical-biological.tpub.com/TM-1-1500-335-23/css/TM-1-1500-335-23\\_274.htm](http://chemical-biological.tpub.com/TM-1-1500-335-23/css/TM-1-1500-335-23_274.htm)

accuracy in the transient model to the static model, the mesh would have to be improved by a factor of three; this would increase the solve time by approximately 33, bringing the expected solution time to ~140 days (20 weeks).

## 4. Preliminary engineering design of the magnet coil

### 4.1. Comparison of different coil materials

The magnet coil can be made of a variety of materials. The three most obvious ones are:

- Aluminium, in particular anodised aluminium strip
- Copper, in particular hollow copper conductor
- Superconductor, in particular niobium-titanium, NbTi, or Magnesium Diboride, MgB<sub>2</sub>

The advantages and disadvantages of the three options are as follows:

#### *Aluminium strip:*

##### Pros:

- anodised surface acts as a complete electrical insulator between the winding layers, saving on space and complexity
- thermal conductivity of aluminium is high and heat can be transported easily in the plane of the strip to the edges of the coil
- heat has to cross over only \*one\* insulating barrier from the heat source into the heat sink (can be gas)
- a heat exchanger, spanning the entire side of the coil is independent of the electric conductor and can be shaped and sized as needed; a simple cooling circuit can be employed
- the coil body is about 1/3<sup>rd</sup> of the weight of copper, but with the added weight of the heat exchangers it may be only half
- coils of a very large size (4m x 1.5m) have been made, but not necessarily with the external cooling facility

##### Cons:

- electrical conductivity of aluminium is less than that of copper which may result in a slightly larger coil for the same flux density
- the strip structure of the aluminium stack will have to be kept totally rigid in the areas where the heat sinks are attached to in order to prevent any damage to the interface between coil and heat sink; this does, of course, not apply to gas cooling
- the use of very large aluminium coils is not as well established as the more conventional copper coils with central cooling; they have been described as beneficial to accelerator magnets as early as 1967 in a paper by Michael Green <sup>7</sup>.

#### *Copper hollow conductor:*

##### Pros:

- the hollow conductor route is a very common design in the world of accelerator magnets
- copper has a higher electrical conductivity, potentially allowing smaller coils than aluminium

---

<sup>7</sup> Use of Aluminium Coils instead of Copper Coils in Accelerator Magnet Systems, IEEE Trans on Nuclear Science, June 1967

- Cooling of hollow conductor is efficient with water in direct contact to the source of the heat
- A correctly resin-potted coil body is very robust

Cons:

- Each individual conductor length has to be insulated against its neighbouring conductor, requiring space, reducing the engineering current density and adding complexity to manufacture
- The cooling and electric circuitry are intimately interwoven resulting in issues with pressure drop of the cooling medium and with ultimate separation of the two circuits at their ends; this separation increased risk of water leakages
- The weight of the coil body is higher due to the higher density of copper
- The resin for potting the copper coil can be similar for both copper and aluminium

*Superconductor:*

Pros:

- The current density in the conductor is very high when compared to conventional conductor
- The power consumption of the coil is negligible; superconducting coils are used for either very high fields, or for very large magnets
- Despite the very low power consumption the magnetic flux densities can be achieved

Cons:

- The magnet coil is part of a complicated structure, embedded in a rigid coil former and in an insulating cryostat; this structure results in a large space requirement around the coil
- The cryostat has to be cooled according to the type of superconductor used; Niobium-titanium (NbTi) requires a more demanding cooling system than Magnesium diboride (MgB<sub>2</sub>). This needs a complicated infrastructure which can be prone to failure if not maintained carefully
- Access to the cryostat is necessary for maintenance purposes
- The cost of a superconducting coil is significantly higher than the cost of a conventional conductor

The complexities of a superconducting structure rule out this route for this project and superconductors will not be treated here.

#### **4.2. Gas-cooled vs liquid-cooled coil**

As indicated in the previous chapter cooling with liquid can be highly effective with aluminium coils. The method is also relatively simple as the heat exchangers are independent from the electrical circuits, limiting both the number of water connections and pressure drops. The supply channel can be slim as water has a very high heat capacity, thus being able to carry away heat in a compact way. The disadvantages of liquid-cooling the coil are two-three-fold:

- The presence of water within the helium container always carries the risk of leaks, and a leak of liquid within the helium container would be crippling for the installation.

- The interface between heat exchanger and coil surface could deteriorate over time, possibly even fracture
- The interface and the connections between the heat exchanger segments will be affected by radiation and could suffer in their function over time

Gas-cooling of the magnet coil within its steel former has one major advantage: there can never be a leak in the cooling liquid. Further advantages are the potentially easier manufacture of the coil as movements between the individual layers of aluminium strips are of no consequence. No composite material, like Stycast, can deteriorate due to radiation as there is no need for such a material to be used. The disadvantages of a gas-cooled coil are:

- The power density of the coil needs to be lower than the one of the liquid cooled coil, reducing the value of the field-integral within the magnet circuit
- The gas flow (here it needs to be helium gas) will require a larger supply channel
- The gas flow needs to be channelled around and along the coil body and provision needs to be made for the safe supply and exhaust of the helium gas to and from the magnet former

The advantages of a gas-cooled coil over a liquid-cooled coil were so significant that the reduction of the magnetic field integral value was deemed to be of a lower importance to the design than the improvement in the reliability of operation of the magnet.

### 4.3. Aluminium coil

A magnet coil made of aluminium conductor is best made of wide aluminium strip which has hard anodised surfaces. The electrical insulation of the aluminium oxide between the individual strip layers makes the need for extra insulation materials unnecessary.

The main reason for the use of a coil made of anodised aluminium strips is the easy capability of separating the electric circuit from the water-cooling circuit. This minimises the complexity of the arrangement for the cooling system. The cooling system can be operated with fewer and more durable connections, and operation with low pressure drops is possible.

One layer of the strip can be wound directly onto the next one. The voltage drop between the adjacent layers will be small, much lower than the maximum which the oxide can tolerate before voltage breakthrough occurs.

As heat is conducted mainly through regions of high pressure the heat flow perpendicular to the strips will not be optimal unless the strips are tightly pressed together. The heat sinks would, in this case, be mounted on the sides of the race-track coil, unlike the top-mounted heat exchanger seen in Figure 37.

The most direct route for the heat to take is in the plane of the aluminium strip. This means that the heat could be extracted at the bottom or the top of the coil. A heat sink would have to be glued to either the top or the bottom surface. This glued connection between aluminium coil and heat sink is crucial. It must not be compromised. The effects of radiation on the connecting compound needs to be considered.

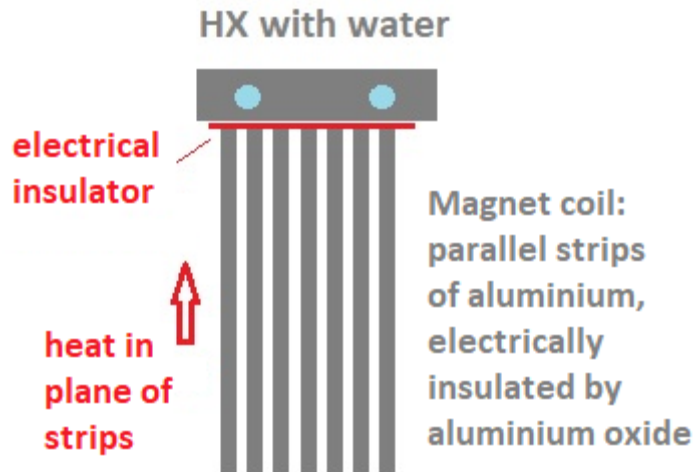


Figure 37: System of aluminium coil with heat exchanger glued to the top of the coil

#### 4.3.1. Example of a small aluminium coil

A small aluminium coil has been built to demonstrate the arrangement of coil and heat sinks, and this is shown in Figure 38 below.

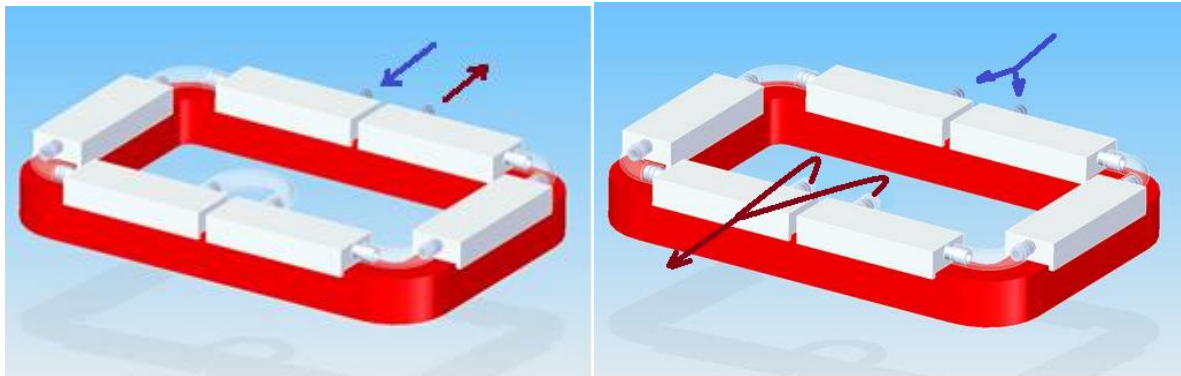


Figure 38: Small aluminium coil with attached heat sinks: single cooling circuit on left, divided circuit on right

The heat exchanger is split into a number of sections for three reasons:

- 1) A single heat exchanger would be difficult to manufacture above a certain size
- 2) To compensate for differential thermal expansion between coil body and heat exchanger the relative movement is minimised by splitting the heat exchanger into solid sections joined by flexible interconnects
- 3) It is possible to feed water into parallel sections of the heat exchangers, as indicated with arrows in the image on the right. This will reduce pressure drops but has the disadvantage of, potentially, unequal flow through the sections.

In Figure 39 an experimental setup is shown. This experiment was performed to establish the properties of heat removal from an aluminium coil with high current densities, approaching 20A/mm<sup>2</sup>.

Usually, aluminium coils are operated without active cooling and with current densities of around  $2.5\text{A}/\text{mm}^2$ . They can operate at high temperatures of  $> 500^\circ\text{C}$ .

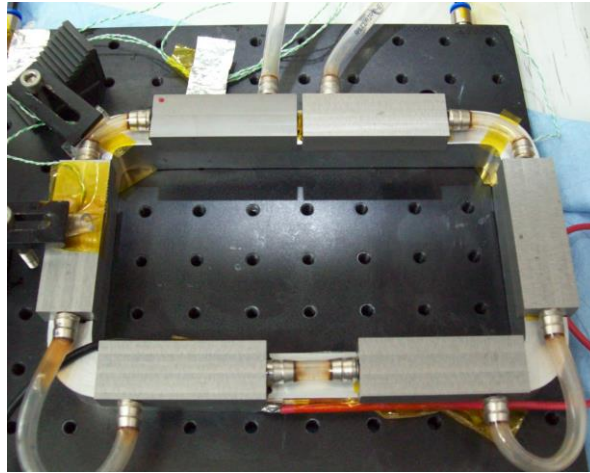


Figure 39: Experimental set-up of sample aluminium coil with

#### 4.3.2. Pressure drop of cooling circuit of aluminium heat exchangers

A hollow aluminium conductor is not common, certainly not at lengths at which copper conductor is available. Cooling of an aluminium coil is therefore applied externally. This is best performed with a flat heat exchanger which is thermally connected to the coil body, as shown in Figure 38 and Figure 39 above. One example of a flat-body heat exchanger is shown in Figure 40 below. The conduits for the cooling medium, water, was machined into an aluminium plate and the grooves were then closed from above with friction-welded aluminium plate. The cooling circuit is thus enclosed within the heat exchanger with only one entry and one exit port. As the cooling channels can be made very wide and high the issue with pressure drop is severely reduced when compared to hollow copper conductor. In this example the individual cooling channels are 26mm wide and 6mm high. The heat exchangers will add, of course, to the volume of the coil arrangement.



Figure 40: Aluminium heat exchanger with embedded channels seen in cross section, unit is friction-welded



An example of pressure drop for an aluminium coil with a 25kW output power and dimensions 4.6m long and 1.6m wide. As shown in Figure 38 it is best to subdivide the heat exchanger into segments that are connected either in series or parallel.

- Area of HX segment: 1000mm x 300mm
- Cooling channels / HX: 26mm (w) x 6mm (h) x 5 x 900mm = 4.5m
- Number of 1m HX on coil: 10, resulting in 45m of cooling channel
- Pressure drop (6mm groove height): 8bar @ 37 l/min
- Pressure drop (10mm groove height): 2bar @ 37 l/min

These values need to be adjusted slightly for the coverage of the heat sinks of the coil as the coil circumference is 11m and the heat sinks are  $10 \times 1\text{m} = 10\text{m}$ . A temperature rise of  $10^\circ\text{C}$  has been used in the above calculations. The pressure drop values in the above example need to be compared with the pressure drops for the hollow copper conductor in the following section for a copper coil.

## 4.4.Copper coil

### 4.4.1. Example of existing copper coil

The main reason for the use of a coil made of hollow copper conductor is the well-established method of producing such coils. In the image below (Figure 41) we show a large dipole coil of comparable size to the coil under consideration in this report. These coils are usually potted in a resin matrix and consist of hollow copper conductor. The current is carried by the copper, the cooling is performed via the central duct within that conductor. The following three images have been taken, with kind permission, of a dipole magnet installed at the ISIS synchrotron at the Rutherford Appleton Laboratory.



Figure 41: Dipole coil embedded in flux return yoke, seen from below

In order to keep the electric current to manageable levels, and the coil volume to a manageable size, the conductor is long and relatively thin. This means that the cooling water has to go through a long path with a large pressure drop as a consequence. In order to counter this pressure drop the conductor length can be sub-divided into several sections. Each section is then supplied with a separate water



circuit, usually tapping into a common manifold. At the location of the manifold the electric and water circuits are separated, and this area is a crucial point of increased complexity and of reduced reliability. An example is shown in the photograph below (Figure 42). There must be such an element in the circuit which consists of an electrically isolating material but which also acts as a coolant connection.



Figure 42: Area where the electric and cooling circuits are split

The coil which is fed by these complicated manifolds is shown in cross section in the picture below (Figure 43). Each of the (here) 168 conductor elements needs to be electrically isolated from each other with glass tape/weave before the combined bundle is potted within a resin matrix to give it rigidity.

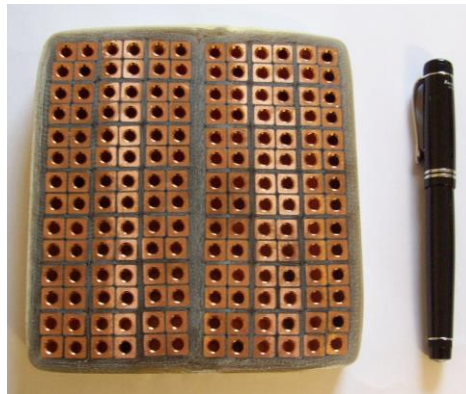


Figure 43: Cross sectional view of a compound copper coil, 9x9mm conductor, 4mm hole



Figure 44: Profiles of hollow copper conductor and insulation (Luvata of Finland)

#### 4.4.2. Pressure drop of cooling water, hollow copper conductor

In order to show the dependence of the size of the cooling channel within the hollow conductor two apertures for water flow inside the same external conductor size were chosen, namely 8 and 10mm in a 15×15mm<sup>2</sup> conductor. This assured the same length of conductor in both cases, albeit running at a different current density to achieve the same Amp-turns. The same temperature rise of 10°C was allowed.

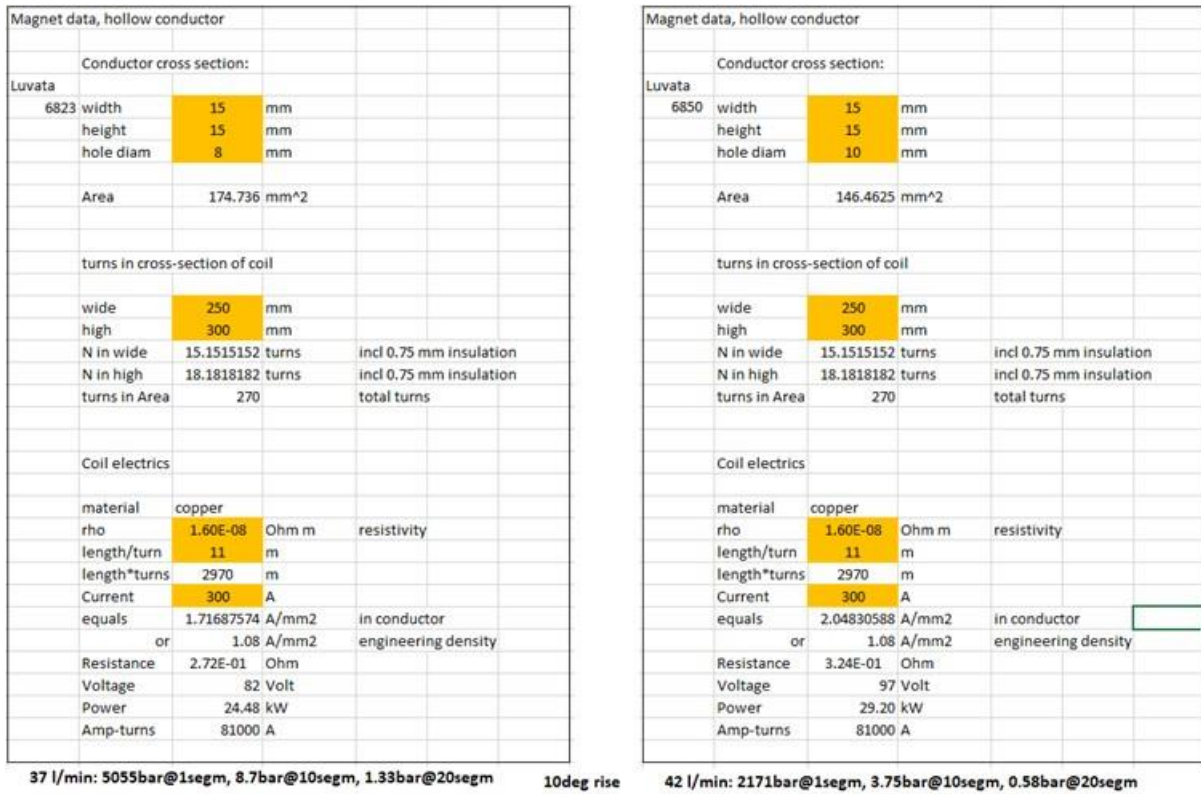


Figure 45: Comparison of 15mm with different orifices

Table 7: Effect of diameter of cooling water channel on pressure drop

Water flow through hollow copper conductor of 15×15mm <sup>2</sup> , temperature rise: 10°C		
Orifice	8mm	10mm
Power	25.5kW	29.2kW
Flow	37l/min	42l/min
1 segment	5055bar	2171bar
10 segments	8.7bar	3.75bar
20 segments	1.3bar	0.58bar

From the impractically high values for the pressure drop it is obvious that the coil body will have to be sub-divided many times to achieve a manageable pressure drop. This sub-division of the coil body requires an intricate piping scheme, as shown in Figure 42, to split the water circuit into sub-divisions. Distributing manifolds will have to be used. Feeding numerous circuits from a single manifold always makes it possible that various identical conductor sections are cooled by differing coolant flows and this could result in unequal cooling of the coil body.

The size of the conductor for this comparison is significantly larger than the size of the conductor shown in the practical example in Figure 43 above, where the size is  $9 \times 9 \text{mm}^2$  with an orifice diameter of 4mm. The smaller the diameter of the orifice, the higher the number of sub-divisions of the coil body must be in order to bring down the pressure drops.

#### 4.4.3. Separation of electric and coolant circuits

In Figure 46 a manifold is shown on the left which consists of an electrically non-conductive body which receives the inflow (or outflow) of cooling water. The individual ends of the coil sections are connected to this manifold; they are now electrically isolated from each other, but connected in a parallel way to the cooling water. An identical manifold is on the outlet side of the coil body where the individual coil sections feed the heated return flows into the insulating manifold from where the water will go to the chiller for re-cooling. The electric connections between input and output flow manifold are indicated in the image below on the right of this figure.

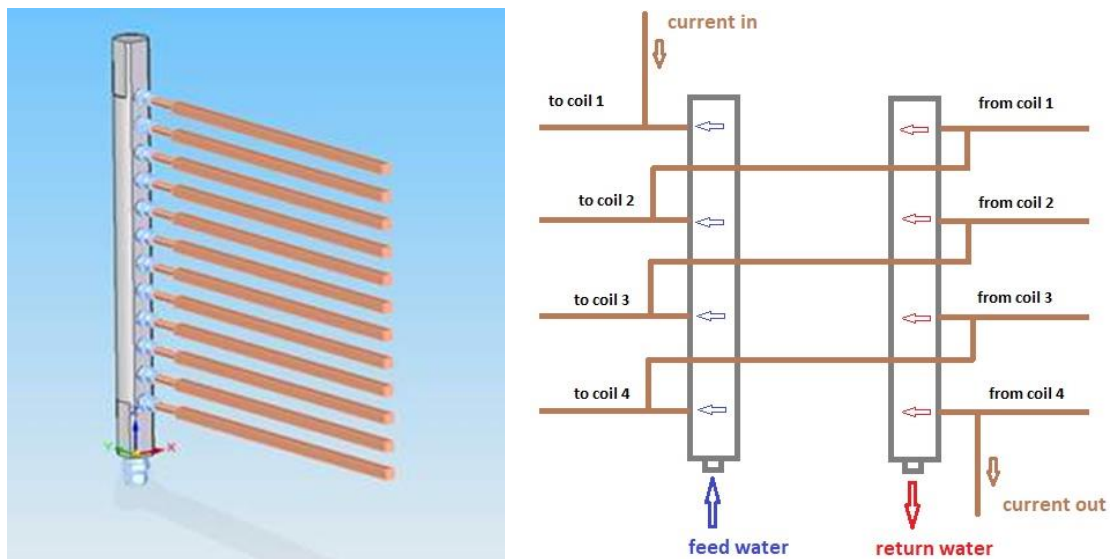


Figure 46: Coolant manifold and coolant / electricity separation, on right: electrics in brown, coolant in blue / red

The manifold material is PEEK (polyether ether ketone), a thermoplastic polymer, which has been shown to be water-resistant over time, mechanically robust and is used extensively for fluid manifolds. Experience of using other materials, for instance glass-fibre, showed that durability under water flow and pressure cannot be guaranteed. The connections of the copper conductor to the manifold must also be durable and leak-tight. Experience has shown that Swagelock connectors are best suited for this purpose. The sealing ring between Swagelock and PEEK surface should be a Dowty washer (a metal ring with a rubber insert on the inner diameter).

#### 4.5. Influence of ionising radiation on magnet materials

Ionising radiation can have a compromising, or even destructive effect on materials that have been used for the assembly of the magnet structure. Both the aluminium and copper coils treated up to now will have man-made composites included, either as resins to glue the heat exchangers onto aluminium coils, or as potting agents for copper coils.

The effect of radiation on low-carbon or stainless steel is not treated here in detail. One issue with stainless steel is the creation of the  $^{60}\text{Co}$  isotope within the steel which contains large amounts of the naturally occurring stable  $^{59}\text{Co}$ . As these isotopes are not airborne they will have no effect on the magnet coil.

The main effect of the radiation is to create oxidants from the surrounding water (humidity or immersion into water). These oxidants could potentially damage components of the magnet coil and ancillaries. As there is no immersion, and the humidity is removed by the operation of the target / magnet volume in a helium atmosphere, oxidation is not a concern.

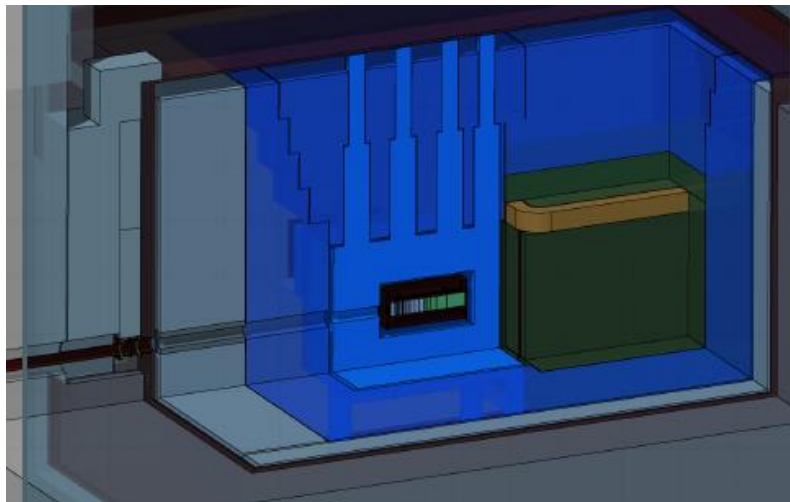


Figure 47: Proton beam coming from left, target area and magnet block with coil

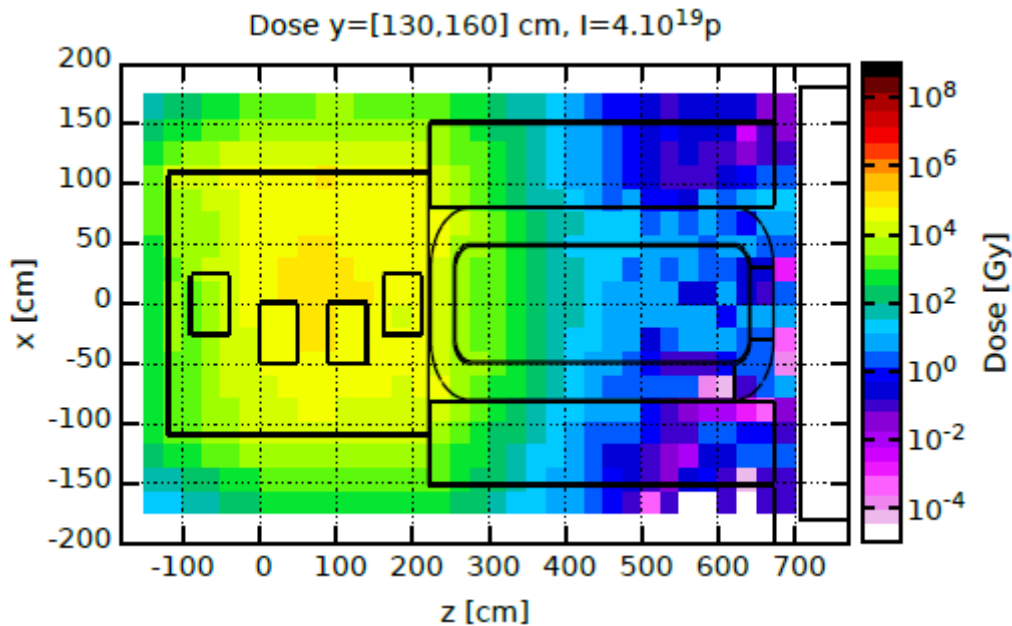


Figure 48: Average annual radiation dose at coil height

From Figure 48 it is visible that the coil body will see an annual radiation dose of around  $10^5$  Gray, i.e. 0.1MGy per year. The section of the coil away from the target, at the location where the supply channel is located, sees low doses of radiation, approximately  $10^{-3}$ Gray per year, therefore the materials within the supply channel (downstream side of coil) require little consideration as to their resistance to radiation. Even rubber seals would be suitable there (rubber seals may be used on the downstream cover plate as shown further down in Figure 54). The main concern is the area of the coil that is located towards the target volume (upstream side of coil).

An annual dose of 0.5MGy is tolerated by many materials but the design of the magnet coil must take into account the entire duration of the installation and use which could be up to 10 years. A total dose of 5MGy is therefore required and the practical sizing should take into account any unforeseen events. As a design criterion a total radiation dose of 10MGy is therefore assumed.

The material for coil centring suggested further down (from section 4.2 onwards), PEEK, is listed by CERN<sup>8</sup> as 3MGy in air, and 3 to 10 times higher in an inert atmosphere.

#### 4.5.1. Potting material for copper coils

A typical resin used for the impregnation of radiation-exposed coils is the mixture of Araldite MY 740 with Hardener HY 906 and Accelerator DY 073-1. Flexibiliser DY 040 may be used up to maximal 10%. This Araldite is cured under temperature ( $\sim 130^\circ\text{C}$ ) and can withstand the 10MGy dose. Copper coils are often embedded within this resin. One needs a very large curing oven for the impregnation of the large coil as the coil must be fully immersed and covered by the resin while being temperature cycled.

There are a number of alternative potting materials, listed in the CERN Yellow reports on radiation<sup>9</sup>. Epoxy AY103/HY951 or Araldite F HY905+DY040+ DY061 are examples.

<sup>8</sup> CERN document CERN-TIS-TE-IR-99-08.pdf, Behaviour of Organic Materials in Radiation Environment, Marc Tavlet and Sorin Ilie, 1999, page 5

<sup>9</sup> <http://imhotep.rl.ac.uk/cgi-bin/imhquery.pl>

#### 4.5.2. Interface material for aluminium coils

For aluminium coils the requirements are that the bond between coil and heat exchanger must not break. Silicone rubber, Grade G2 – CERCEM will withstand 5MGy. If that material is filled with thermally conducting material like Alumina ( $AlO_2$ ) the radiation resistance will increase further.

Silicone sheet, filled with electrically conductive carbon fibre, is used extensively for space-based applications (antenna) and these could also be used as an electrically insulating, thermally conducting interface to aluminium coils.

An alternative approach to the stability requirement of the interface is to restrain the coil body sufficiently to prevent any relative movement between coil and heat exchanger (see Figure 49). If no relative movement is possible then a thin layer of thermoset resin can be used. This was successfully tested in a laboratory at STFC, using Stycast 2850 (using room-temperature cured resin, Catalyst 9).

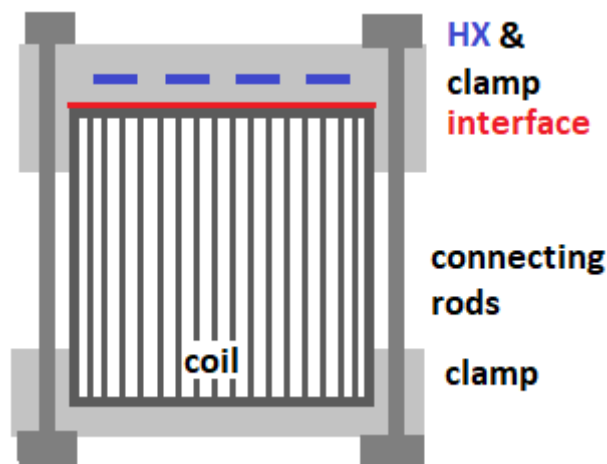


Figure 49: Restraint of Aluminium coil to keep interface undisturbed, heat exchanger can be at top or bottom of coil, or both

## 5. Gas-cooled coil

The coil designs up to now have included water cooling, either internal to the conductor (copper coils) or external to the conductor (aluminium coils).

The internal water cooling suffers from the necessity for splitting the water circuit into a number of sections in order to send water into a number of parallel circuits through the electrical conductor. This is the only way to limit a very large pressure rise without making the coil body so large that it is physically disadvantageous and uneconomical. Having many parallel circuits requires a large number of water connections. Each of the water connections represent the possibility of a water leak, or other failure. The coil may also need to be potted with resins, and it certainly will include manifolds made of plastics, mainly PEEK. These artificial materials will suffer from exposure to radiation and this may impact on their durability. As the magnet will be used in an inaccessible location the use of such a design is difficult to justify.



The external water cooling of an aluminium coil reduces the number of water connections significantly. It also separates the electric circuit from the cooling circuit, allowing large volumes of cooling water flowing through heat exchangers without building up pressure in a significant way.

Both coil designs will suffer from unreliability when operated in inaccessible spaces. Water leaks cannot be tolerated under any circumstances. One way out from this predicament is the use of gas cooling for the coil body.

The gas must be in direct contact with the metal of the coil. This requirement makes it more difficult to use a copper coil as there needs to be insulation between the layers or strands of copper. One could build up a copper coil from strips similar to an aluminium coil but, again, there would have to be layers of insulation between the strips, reducing heat transport within the coil.

A natural material for a gas-cooled coil is anodised aluminium strip. Heat is transported well in the plane of the aluminium, and also perpendicular to the strips if they are strongly pressed together. The aluminium strips are electrically isolated from each other by their layer of aluminium oxide.

The disadvantage of gas cooling is the reduced capacity for heat removal from the coil body.

#### **5.1.1. Gas cooling layout for an aluminium coil**

The installation within the target complex relies on high-reliability components with as little maintenance as possible. In particular, this is true of the magnet coil. The method of cooling with water poses an inherent risk stemming from leaks and blockages. This risk can be minimised by using a simple cooling method, such as described in the previous chapter, where electric and cooling circuits are separated and the number of connections for the cooling medium are kept low. A method of cooling that would dispense with a cooling liquid would still be preferable though.

It was agreed with the BDF Target & Target Complex (TTC) team that an evaluation should be done with the aim of producing the largest magnetic field integral provided by the lowest possible power input to the coil. If the power input could be reduced from the mid to high 20kW values to a level around 4kW then cooling with the surrounding helium gas could possibly be accomplished. The optimisation in paragraph 5.3.2 is concerned with this reduction.

The cooling with gas in a closed loop requires

- a) Sufficient cooling capacity for the return gas
- b) Sufficient gas flow past the coil (the heating element)
- c) Sufficient surface contact between coil and gas, i.e. a sufficiently large heat transfer coefficient

The major source of heat within the helium container is the proton target. The target and its immediately surrounding shielding blocks are water-cooled from the supply trolley. There is residual heat from these components and this heat will have to be removed by circulating helium gas within the helium container. Allowing helium gas to circulate between the iron shielding blocks will supply cooling to the entire content of the helium container. When using a gas-cooled aluminium coil within the helium container this circulation of helium gas should be enhanced and channels should be introduced between the shielding block. That would allow heated helium gas to escape from the

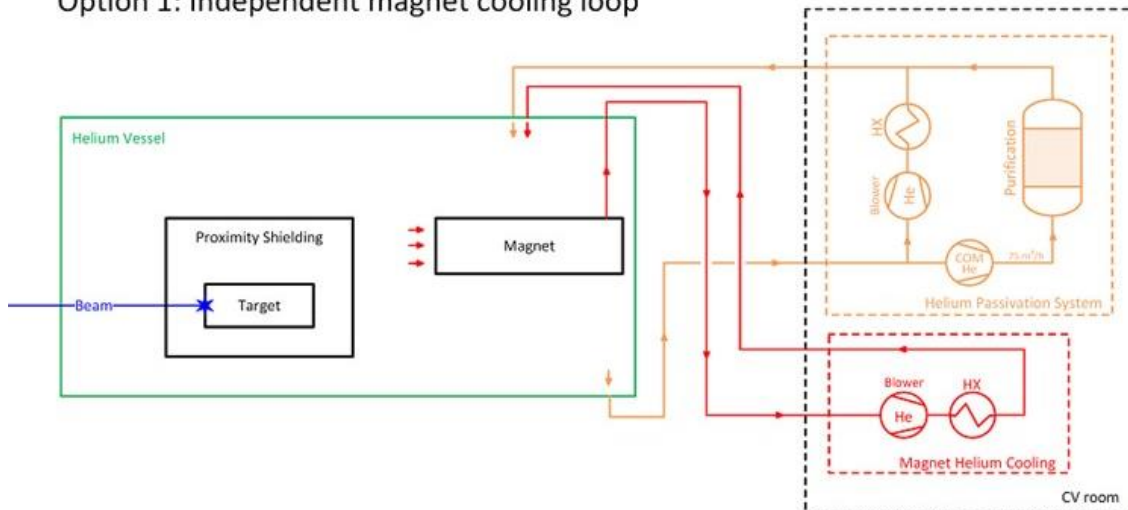
blocks and be directed to a port in the wall of the helium container. From there it would be guided into an external heat exchanger which would remove the heat and an adjacent pump would force the helium gas back into the helium container. It would first make contact with the aluminium coil before cooling the iron blocks – or, possibly but not preferably, the other way round.

Two options (Figure 50) for cooling circuits have been proposed by the BDF TTC team

- one utilising a separate cooling loop for helium container and magnet
- the other using a combined circulation loop but directing the gas flows from container and coil independently with provision for varying the gas streams coming from container and magnet.

As target and magnet are usually powered at the same time it makes sense to give the combined, parallel flow option 2 a preference as the arrangement is simpler as far as active components are concerned. Also, the lowest temperature possible should be used for cooling and the highest volume flow should be envisaged (up to 1000m<sup>3</sup>/h). The decision about which scheme will actually be applied will depend on a number of factors which will have an effect on the choice for the cooling circuit.

**Option 1: Independent magnet cooling loop**



**Option 2: Magnet cooling in parallel with helium circulation**

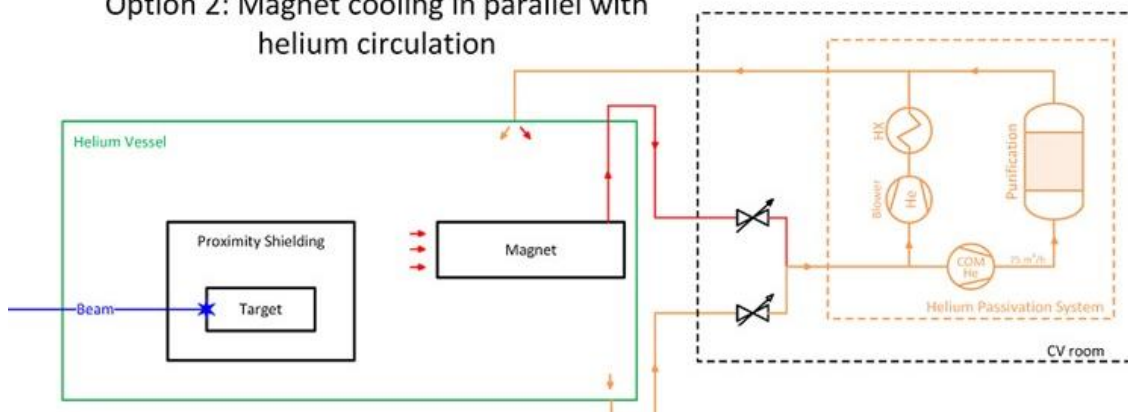


Figure 50: Cooling of the helium container and coil with helium gas, separate and combined variations (scheme by CERN)



## 5.2. Design of the gas-cooled coil

The coil can be designed and manufactured without the need of potting it or restraining it mechanically to prevent all relative movement to a heat exchanger. The cross-section of the strip material is such that the ends are slightly tapered (caused by the cutting of the strip) and this avoids any sharp edges or burrs between the individual strips. The coil can now be wound layer on layer, as described in section 5.4.1. The coil body, with its individual strip-layers, is then held together locally with tape. The aluminium surface should not be covered by this tape more than necessary in order to keep it accessible to a flow of helium gas that will remove heat from the coil.

The coil is then lowered into the grooves of the coil former where it will be kept at a uniform distance to the steel walls by locally mounted restraints, indicated in Figure 62. To prevent it from falling out from the former non-magnetic retainers are fixed across the lower opening of the magnet former. With these localised restraints the coil is still able to move slightly due to thermal expansion and contraction. The gap between coil and walls of the former, including the stainless steel surface at the base of the former, allows helium gas to flow over the entire surface of the coil, from the downstream entrance of the beam to the upstream exhaust near the target.

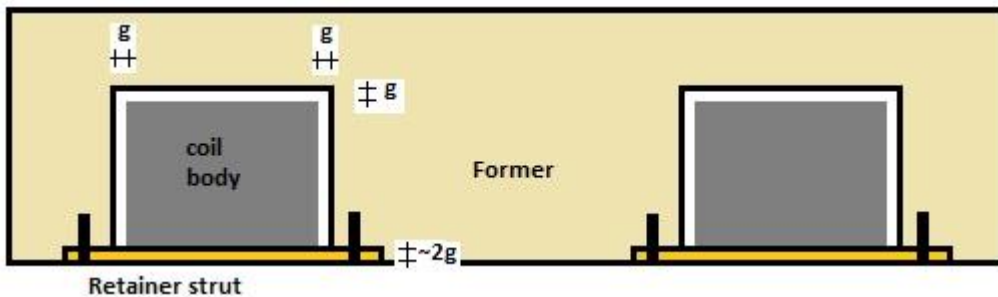


Figure 51: Retention of aluminium coil in magnet former at bottom

The coil is held flush to the magnet former by retainer struts which are bolted onto the former as shown Figure 51 above. The thickness of the struts should ideally be chosen to be equal to the gap,  $g$ , all around the coil but this may not be possible as the struts will need to support the weight of the coil, and also include provision for electrical insulation. Given a certain volume flow of the cooling gas the size of the gaps will determine the flow speed of the cooling gas along the surfaces of the coil. More detail is given in section 5.4

Coil characteristics are treated in the following section.

### 5.3. Coil data

The technical data of the coil are listed in the table below

**Table 8: Coil data, gas-cooled coil structure**

Material	Aluminium	
External dimensions	4.48 x 2.07 x 0.3	m
Cross section	0.26 x 0.30	m <sup>2</sup>
Coil surface	13 (approx.)	m <sup>2</sup>
Strip dimensions	1 x 300	mm <sup>2</sup>
Packing fraction	0.9	
Total length of strip	2560	m
Potting agent	None	
Mass	2700 (approx.)	kg
Electrical resistivity $\rho$ (at RT)	$2.82 \times 10^{-8}$	Ohm-m
Thermal conductivity	205 (in the plane of the strip)	W/mK
Current	135	A
Current density (strip)	0.45	A/mm <sup>2</sup>
Current density (engineering)	0.41	A/mm <sup>2</sup>
Amp-turns	32,000	A
Resistance	0.24 @ 20°C, 0.27 @ 50°C	Ohm
Voltage	33 @ 20°C, 36.2 @ 50°C	V
Power	4.43 @ 20°C, 4.90 @ 50°C	kW

The coil is terminated at both ends with a copper element to which the external power supply cables are soldered.

The resistivity,  $\rho$ , of high purity aluminium with respect to temperature is given in the following table and is calculated according to  $\Delta\rho = \alpha \cdot \Delta T \cdot \rho(0)$ , with  $\alpha$  being the temperature coefficient (K-1), here 0.0039 K-1:

**Table 9: Electrical resistivity and coil power consumption vs Temperature, base resistivity taken from manufacturer**

Temperature °C (K)	$\rho$ (Ohm-m)	Power (kW)
20 (293)	2.82 e-8 (base)	4.38
30 (303)	2.93 e-8	4.55
40 (313)	3.04 e-8	4.73
50 (323)	3.15 e-8	4.90
60 (333)	3.26 e-8	5.07
70 (343)	3.37 e-8	5.24
80 (353)	3.48 e-8	5.41
90 (363)	3.59 e-8	5.58
100 (373)	3.70 e-8	5.75

It is obvious that the coil temperature should be kept to a minimum in order to keep power consumption under control. Temperature sensors should be installed on the coil body and these sensors should be interfaced with the power supply for the coil. Any temperature of more than 100°C should cause the power supply to reduce the current or to de-energise the coil.

### 5.3.1. Sub-dividing the aluminium coil to obtain redundancy

It is possible to sub-divide the aluminium strip of 2560m length into two or more sub-sections. If the terminations of the sub-sections are guided to the outside of the helium container and electrically connected in series then it is possible to mitigate the effects of a local failure of the coil body. The undamaged sections could then be connected in series, by-passing a damaged section.

The location of the subdivision, or sub-divisions, must be in an area where no thermally induced coil movement takes place in order to prevent friction of the joints with the oxide layer on the aluminium strips. As space is required also to allow for the connections to be made the obvious location for any sub-division is within the gas inlet volume on the downstream side of the coil, the same location where the primary connections between aluminium coil and copper power cables are made.

### 5.3.2. Calculations of cooling requirements

The geometry of the coil, and the location of the coil within the coil former, does not lend itself to a 'text-book evaluation' of the heat exchange characteristics between coil body and surrounding gas. The coil is firmly embedded within the coil former but it has to be given a certain freedom to move under thermal expansion and contraction. There have to be constraints in all directions though to assure an open path for the gas flow around all surfaces of the coil, but, crucially, to prevent the coil from dislocating under magnetic forces. As the coil is embedded within a ferromagnetic former the issue of hoop stresses does not appear, which could have caused a potential deformation of the coil body which in turn could have blocked the gas flow path. A coil arrangement, consisting of individual conductors in close vicinity, and being driven by an electric current in the same direction, will pull the coil together, improving thermal conductivity.

The basic formula for extracting heat from heated surface by convection with gas is:

$$\frac{dq}{dt} = h \times (T_s - T_{gas}) \text{ W/m}^2 \quad \text{or} \quad \frac{dQ}{dt} = h \times A \times (T_s - T_{gas}) \text{ W}$$

where  $h$  is the convection heat transfer coefficient,  $T_s$  is the surface temperature (K),  $T_{gas}$  is the initial temperature of cooling gas (K) and  $A$  is the area of heated surface ( $\text{m}^2$ ).

Typical values for the convection heat transfer coefficient,  $h$ , are:

$h$ (low flow, natural convection)	10
$h$ (moderate flow, forced convection)	100 (this could mean up to 50 m/s flow velocity)
$h$ (moderate flow over cylinders)	200

For the coil geometry treated here the coefficient will be higher than 10 and dependent on the velocity of the cooling gas. Also, this coefficient will not be constant over the entire surface area as flow velocity and, possibly, the flow characteristics will change. Engineering data are given in Figure 52 below<sup>10</sup>.

<sup>10</sup> [https://www.engineeringtoolbox.com/convective-heat-transfer-d\\_430.html](https://www.engineeringtoolbox.com/convective-heat-transfer-d_430.html)

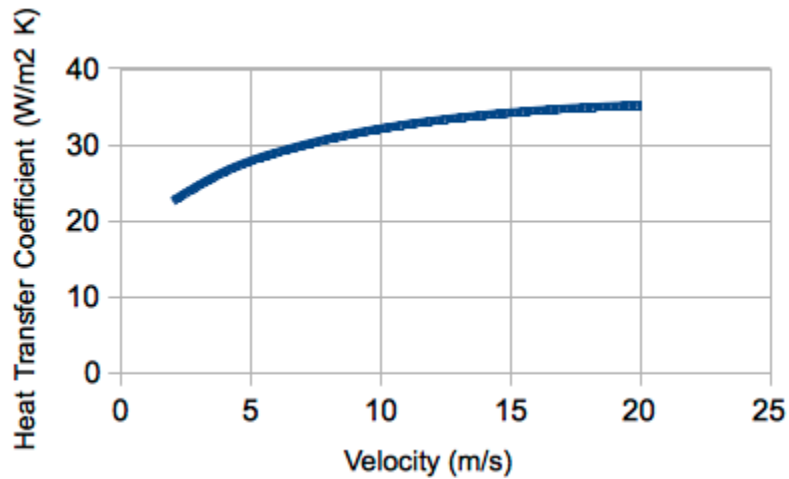


Figure 52: Engineering values for heat transfer coefficients

As an example, using a flow velocity for the cooling gas (here air) of 6 m/s the heat transfer coefficient is about 30 W/m<sup>2</sup>K. For a temperature rise of 30 K the value of heat transfer would be 900 W/m<sup>2</sup>. The surface area of the coil is approximately 11m<sup>2</sup>. The gas could therefore theoretically remove heat in the order of 10 kW. This value is high enough to incorporate a significant safety factor above the calculated value of 4.66 kW. For helium gas the lower molecular mass needs to be considered.

More analytical calculations were performed for this report and the results show comparable values, here with the cooling gas not air, but helium, a flow velocity of 6m/s, a heat removal of 5.0kW, resulting in a temperature rise of the gas of 35K and a temperature rise of the coil body of around 50K. The table below shows calculation results for laminar flow (h=20.8, Reynolds number 1798); and for turbulent flow for the calculation methods of Dittus-Boelter (h=30.25, smooth surface) and Gnielinski (h=18.8, more textured surface):

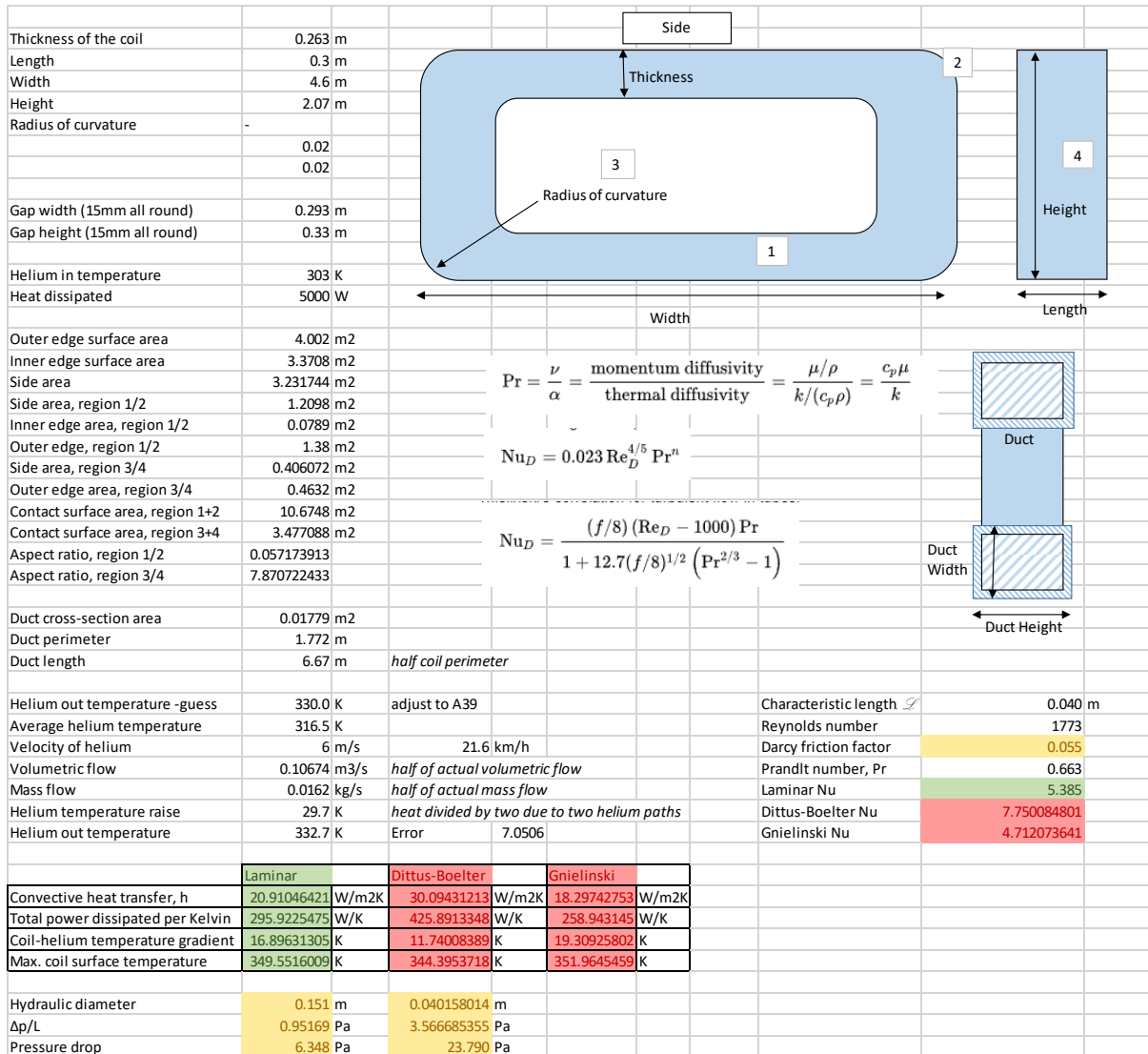


Figure 53: Gas flow and cooling calculation for energised coil

The coil and cooling arrangement in the table above show the results for heating the coil and gas when applying a gas flow of helium of 881m<sup>3</sup>/h. This is the result of a 15mm gap all around the legs of the coil and a flow velocity of 6m/s. The temperature rise of the coil will be around 50°C. The pressure drop will be below 50 Pa, meaning it is negligible.

A helium volume gas flow of at least 1000m<sup>3</sup>/h should be envisaged for the sizing of the installed pumps.

### 5.3.3. Supply of helium gas to coil body

The helium gas for the cooling of the coil will come from a port at the top of the helium container. From there it will be ducted to the end of the magnet coil through a pipe made of stainless steel or aluminium. The length of this pipe is approximately 3m. This down-pipe will slide into an up-pipe which is mounted on the coil former with a length of approximately 1m, giving a good overlap between the two pipes and providing a loose gas seal. The up-pipe will duct the gas to the end of the coil. In order to prevent immediate escape of the helium gas into the space of the helium container a metal housing is fitted to the opening at the end of the coil. This housing forces the helium gas towards and over the aluminium coil. The gas picks up the heat on its way towards the other end of the coil, the end where the target is located. Space is provided at this end location to allow the gas to enter freely into the gas space of the helium container from where it will ultimately be taken and cooled down again before starting its journey through helium container and coil space again. The components for this arrangement are shown in Figure 54 and Figure 55.

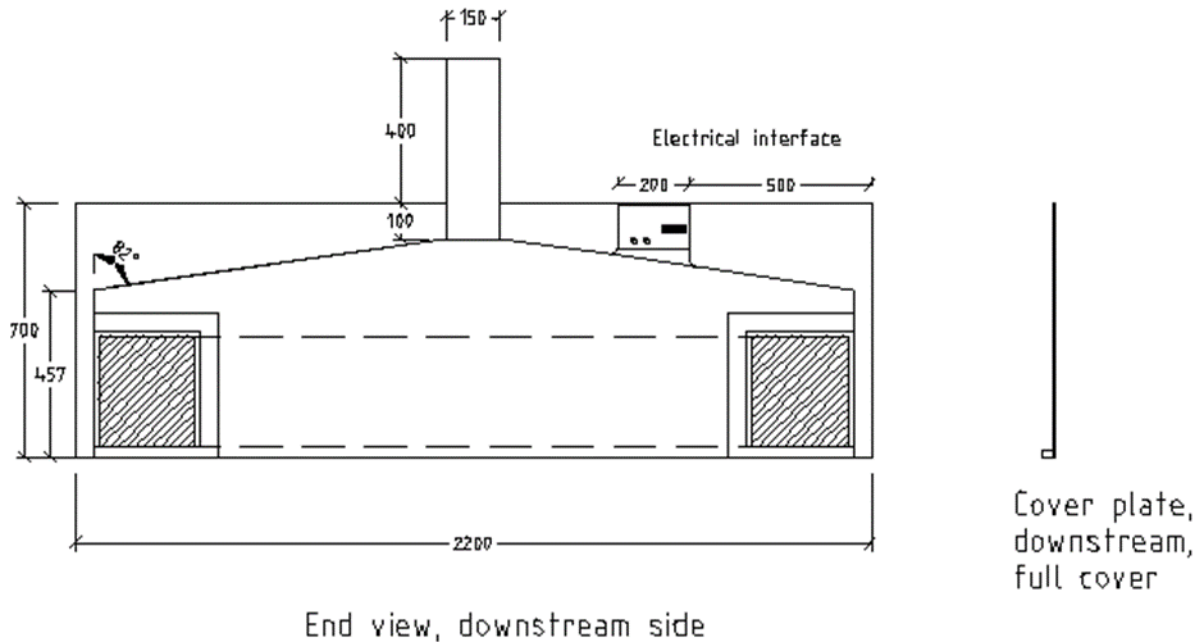


Figure 54: Downstream gas inlet with cover plate

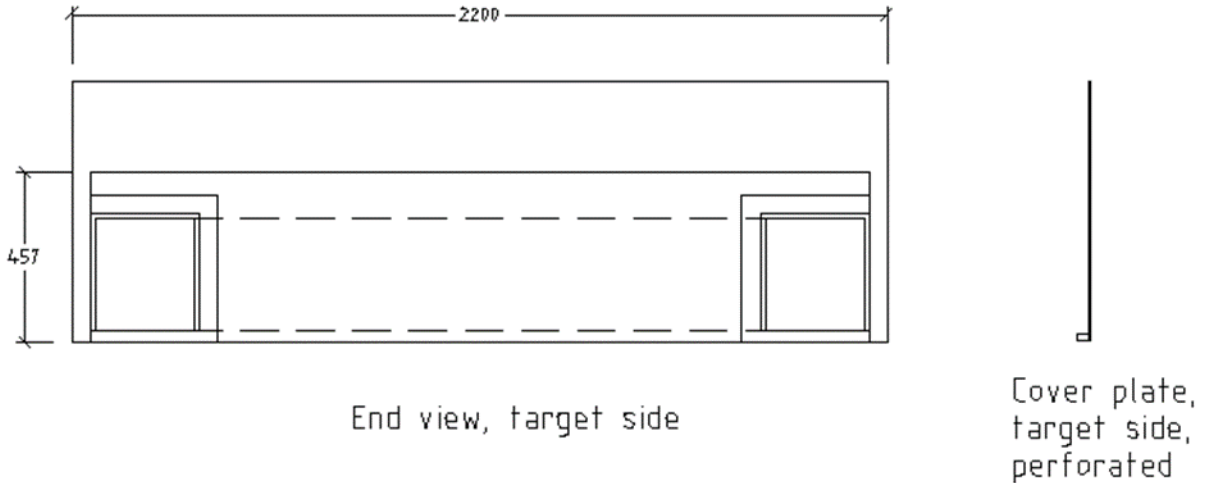


Figure 55: Upstream gas outlet with cover plate

The pressure drop for a gas flow of 1000m<sup>3</sup>/h streaming through the 3m long downpipe is small and it depends on the inner diameter of the pipe. In Figure 56 the relationship between flow velocity and pressure drop is shown. It is clear that even a 100mm diameter pipe with a gas flow velocity of 35 m/s (126km/h) only shows a small pressure drop (0.77mbar). The next larger pipe with 125mm diameter shows a flow velocity of 22.6 m/s (81km/h) and a pressure drop of 0.27mbar. To reduce flow velocity at the outlet of the downpipe a pipe diameter of 150mm is suggested.

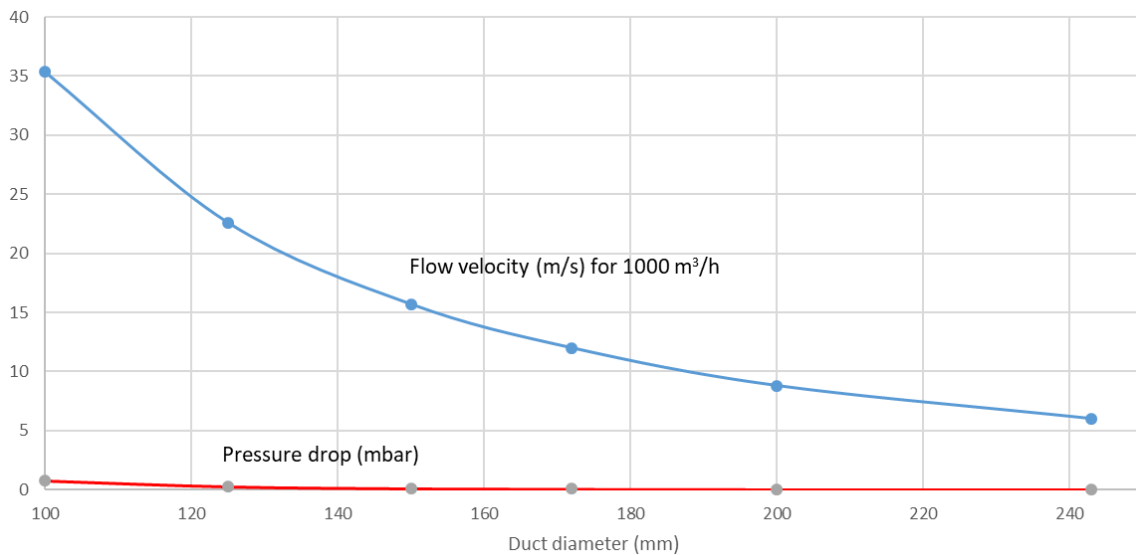


Figure 56: Flow velocity and pressure drop of helium gas in 3m feed duct for various duct diameters

### 5.4. Assembly of magnet coil into steel housing

The magnet coil is flexibly located within a steel yoke as seen in Figure 57. This yoke is made up of a large magnet slab (the magnet former) into which two channels are cut lengthwise in order to accommodate the long sides of the magnet coil. The yoke is open to the upstream (target side) and the downstream (gas supply side). The magnetic attraction vertically upwards is 16.4kN at the nominal current.

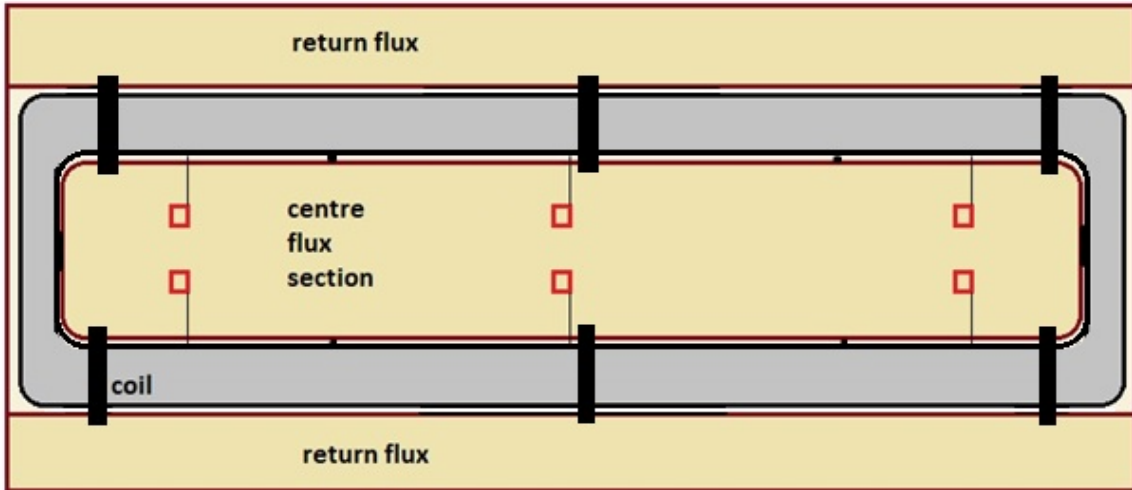


Figure 57: Coil in steel former, seen from below, showing retainer struts for holding coil

Shown again in Figure 58 are the details of the retainer struts. The coil rests on the 10mm thick PEEK insert which has diagonal channels to allow gas to flow between these struts and the coil, avoiding a stagnant area behind the struts. The diagonal channels prevent any possibility of individual strips of the coil body to come out from the coil body.

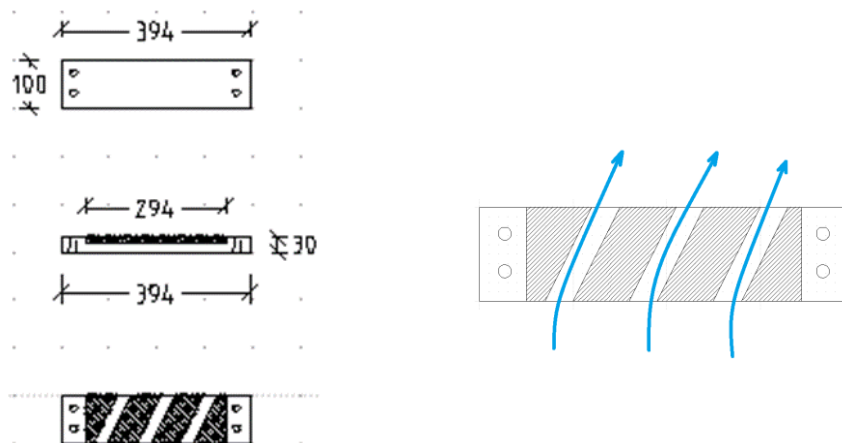


Figure 58: Retainer struts for coil, showing insulating PEEK insert (10mm high) and diagonal gas-flow channels



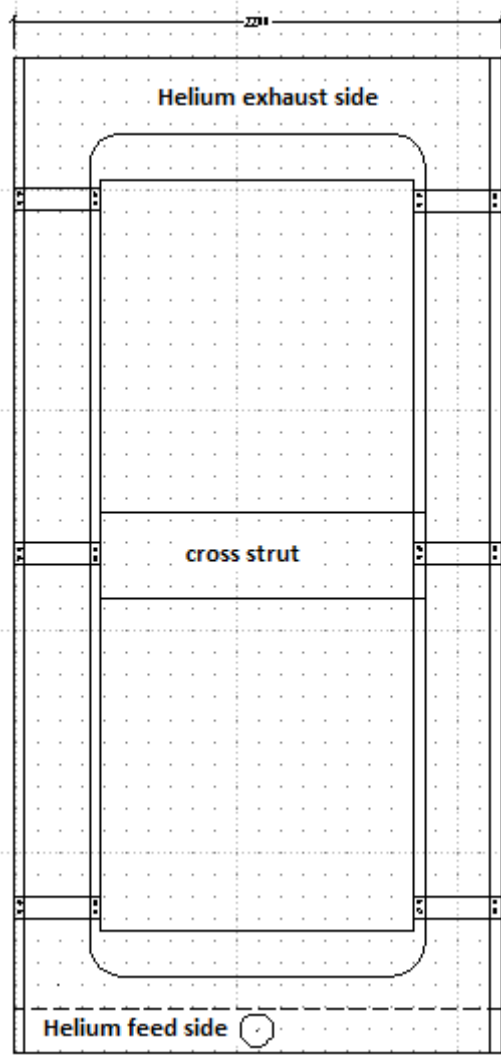
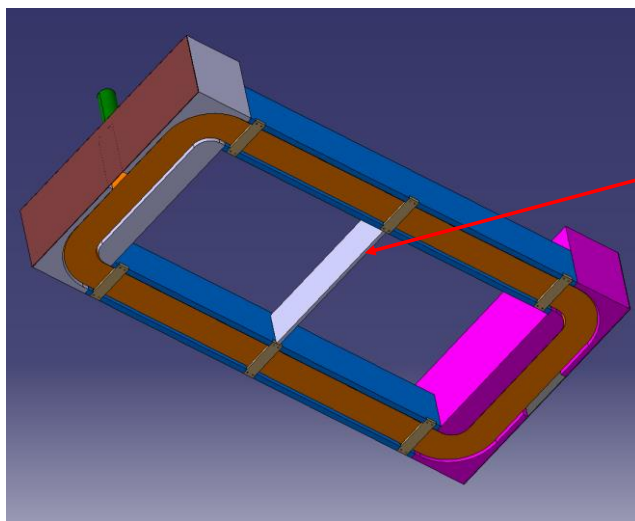


Figure 59: Bottom view of coil former, showing magnet channel and supply tube

The central cross strut is, like the main body of the former, made of low carbon steel (US1010). This cross strut could be rotated by 90 degrees which may allow simpler handling of the shielding blocks.



Central stiffener rotated through 90 degrees to allow biggest possible contact area between vertical blocks and U-shaped blocks that sit on them

Figure 60 Magnet former and coil from below, cross-strut vertical (image by CERN)

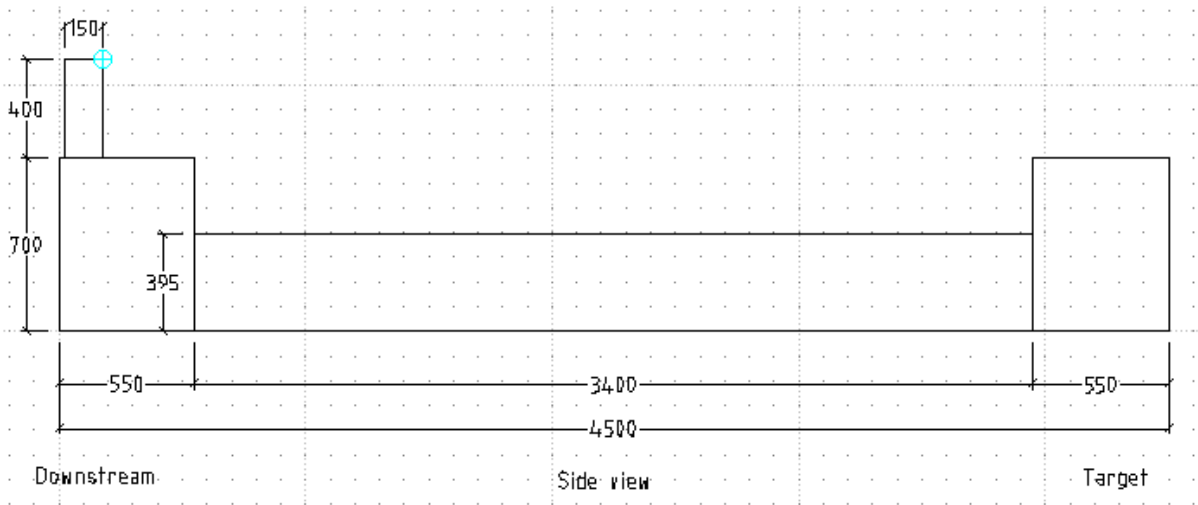


Figure 61: Side view of magnet former, showing downstream and upstream ends

When operated the coil will warm up and it will expand in x (sideways) and z (lengthwise along the beamline) direction. Restraining the coil rigidly in its direction of expansion would result in significant stresses between coil and magnet former.

The expansion over 1.6m and 4.5m under different temperatures is given in Table 10.

Table 10: Physical expansion of coil body due to temperature rise

ΔT	10 °C		50 °C		100 °C	
	over 1.6m	over 4.5m	over 1.6m	over 4.5m	over 1.6m	over 4.5m
distance						
copper (mm)	0.3	0.8	1.3	3.8	2.7	7.7
aluminium (mm)	0.4	1	1.8	5.2	3.7	10.4

Expansion coefficients  $\alpha$  for Cu:  $17 \times 10^{-6} /K$ , Al:  $23 \times 10^{-6} /K$ ,  $\Delta L = L \times \alpha \times \Delta T$

Assuming a failure of the coolant supply the coil temperature could rise by 100°C. This is not likely as thermo-couples will be installed that act as an interlock to the supply of electrical power. The temperature must not rise significantly to above 100°C as the Epoxy that holds the sensors in place will start to soften and deteriorate at these levels. It is obvious, though, that any rigid constraint to the coils would result in damage to the coil body, or the former.

In Figure 62 the method for flexible suspension can be seen. In combination with the bottom retainer struts a series of location plugs, coming from the sides and the top through the walls of the former, are there to keep the coil in its location while allowing it to move under thermal expansion and contraction, up to 4mm in width and up to 11mm in length.

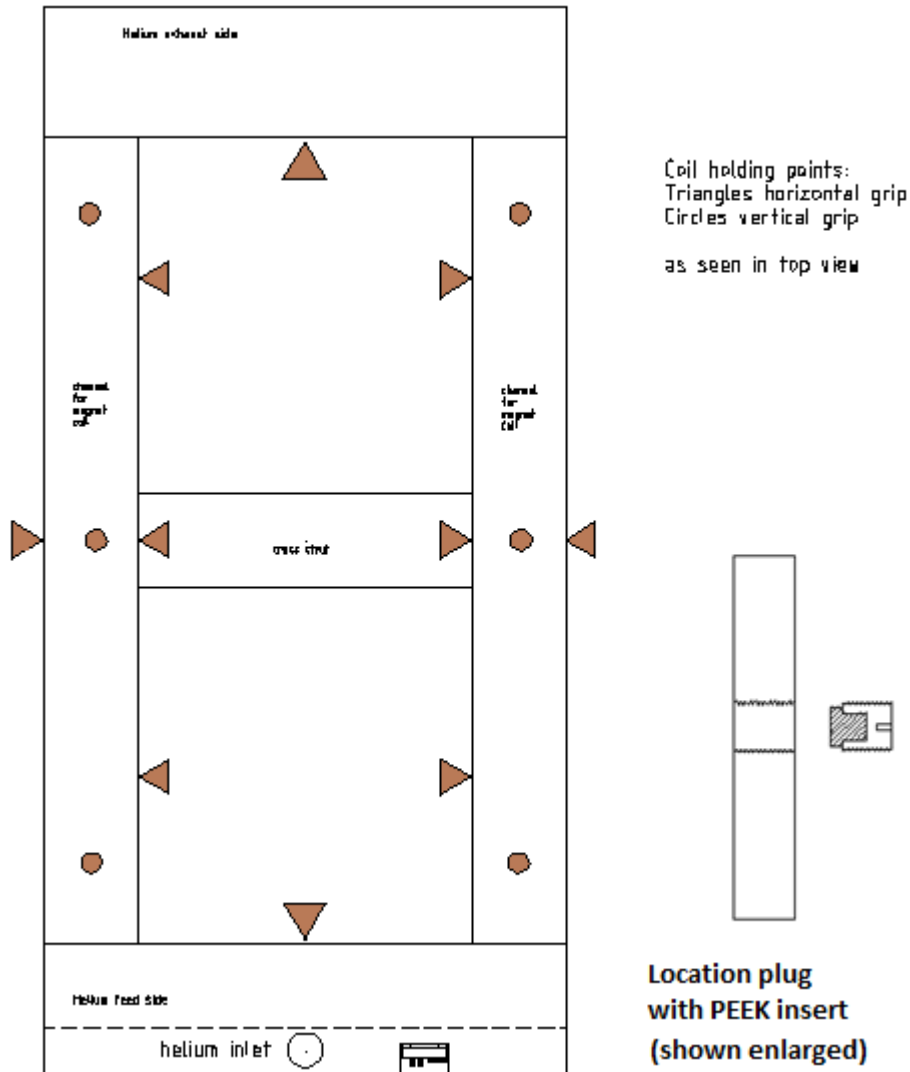


Figure 62: Retention of the aluminium coil within the magnet former, seen from above, also showing the location plugs

#### 5.4.1. Assembly of coil at site of coil manufacturer

The magnet coil can either be wound in the final shape, on a winding former from which it will have to be removed before insertion into the housing which will be the top section of the installed magnet. A suitable device will have to be manufactured that will allow the winding of the coil. This method is the preferred one.

An alternative method for the production of the coil is to wind it on a circular former, on a standard large winding machine. After completing the winding the coil will have to be removed from the winding bobbin and shaped into its final form utilising a hydraulic press. Once the round coil has been pressed into its rectangular shape it is removed from the press and transferred into the magnet pole piece. This pole piece is the actual top section of the magnet.

For both cases the coil itself should remain un-potted. For an aluminium coil this is of an advantage as heat can be transferred through the sides of the strip structure of the coil, as well as in the plane of the strip structure. The thermal conductivity across the layers of aluminium strip is not as high as the

conductivity in plane of the aluminium strip. It is still a magnitude better than for a coil with potted layers.

A square or a rectangular coil will always try to obtain a circular shape when energised. There is, therefore, an increase in outward pressure along the flat sides of the coil. Extensive 'radial' movement of the coil needs to be prevented and a solid limit needs to be set to this movement. This physical limit needs to be shaped in a way that thermal movement is still possible. For the purpose of cooling the coil body it is desirable that as much of the surface area is accessible as possible.

### 5.5. Assembly of helium gas supply channel

The supply channel to the magnet coil measures approximately 3m in length. It is located at the downstream end of the coil, at a maximal distance from the target. Radiation damage, or the danger of radiation damage, will be minimal at this location. The issues with the supply channel are more concerned with stability, accessibility and maintenance.

As the supply channel is a relatively long and fragile construct it is important that the movement of both coil body and iron blocks above will not clash with this channel during installation or maintenance of the magnet coil.

The direct housing of the magnet, and the 1010 structure enveloping it, should be located unambiguously on the stationary magnet structure below. This is best achieved with dowel pins as shown in Figure 63. The vertical magnet flux path is shown in grey and at the bottom of the figure. The (purple) magnet former is the 1010 grade steel that contains the coil. Directly before the supply channel is seen the first block in 1010 material (green), surrounding the former. This section, adjacent to the supply channel, should be shaped with a step. The carbon steel sections higher up should show similar steps where they meet with the supply channel. This arrangement will prevent accidental damage to the channel during movement of the magnet structure and the shielding blocks. The height of the steps should be approximately half of the height of the iron block.

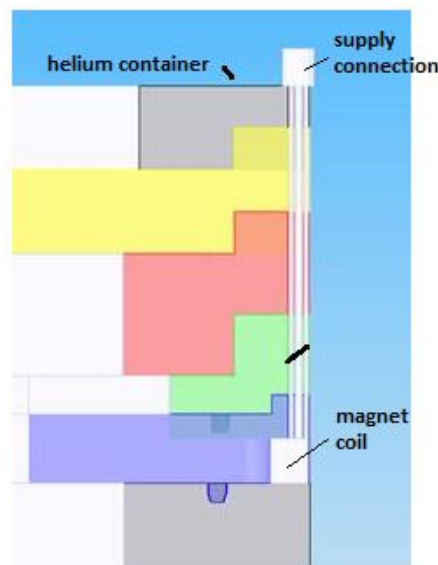


Figure 63: Proposal of an arrangement of magnet coil former (dark blue, with dowel pins) and iron blocks above it

The lower section of the supply channel (to black line) is fixed onto the magnet former and is installed or extracted as one unit with the former and coil. It can be dis-connected when it is accessible, outside of the helium container. Once the coil former is installed the gas supply tube should be attached to the tube protruding from the coil former (jointing connection indicated by black line in Figure 63). The power supply cables (seen in Figure 64), and the sensor cables, are then tied to the vertical gas tube which extends close to 3m vertically from the coil former. This clears the space for installing the shielding blocks above the coil former.

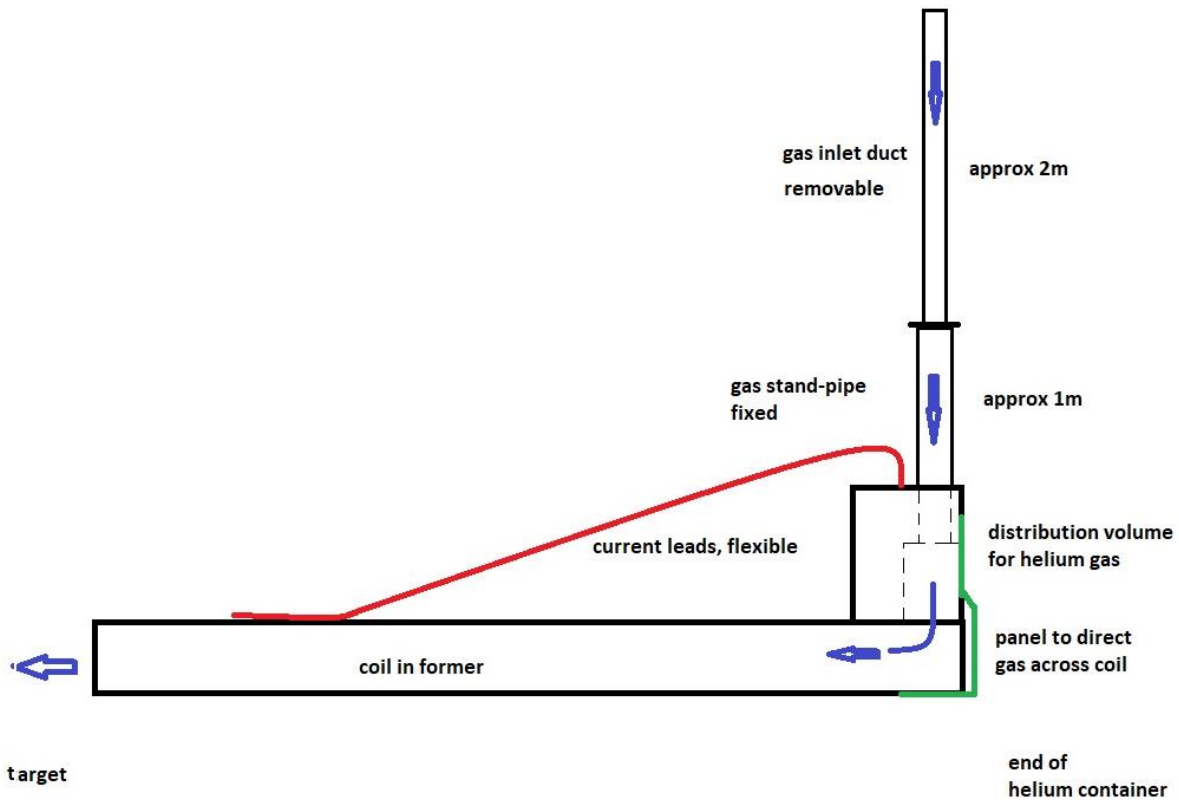


Figure 64: Coil former is delivered with fixed gas stand-pipe and loose electrical cabling

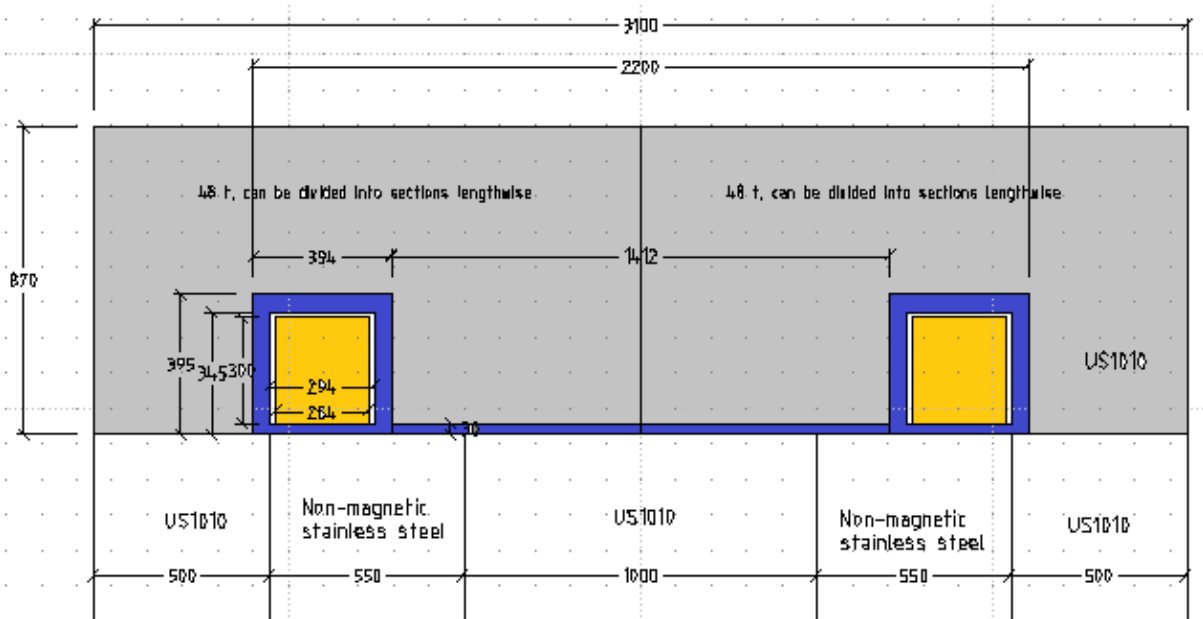


Figure 65: Magnet former (dark blue) with coil inside (yellow) and shielding blocks above (grey), shown midway between down and upstream side

After all of the shielding blocks have all been installed the top cover of the helium container is lowered down, leaving only a small cut-out open, where the gas supply tube and the electrical connections now protrude. A cover box is now fixed to the lid of the helium container with the gas supply protruding from it vertically, and the electrical connections emerging from it horizontally (see Figure 66 and Figure 67 below)

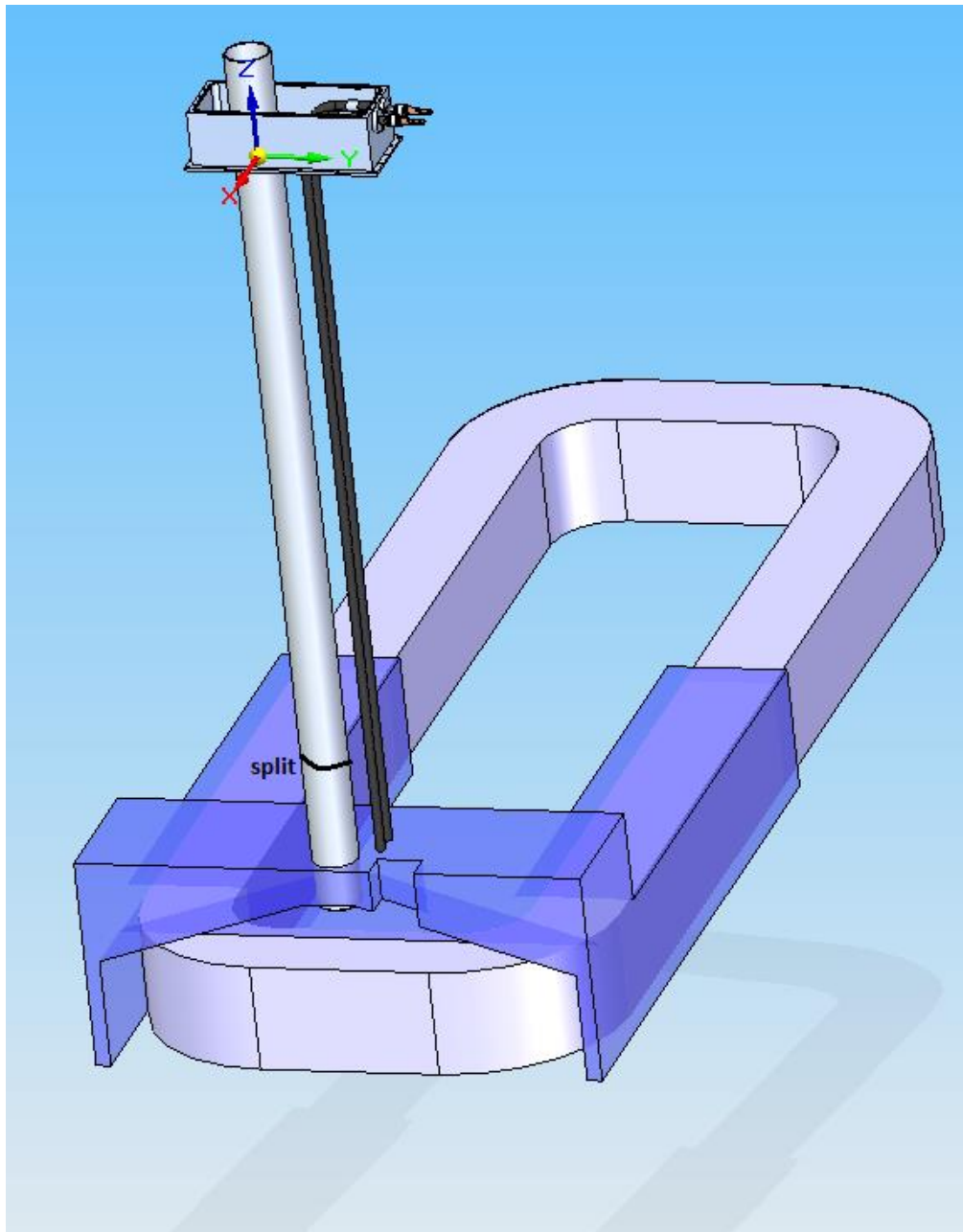


Figure 66: Coil body surrounded by coil former (only one half shown) and attached supply channel which is split

Once the supply channel and the electrical cables and wires are located within this cover box a lid is mounted on top of the cover box. The lid has a protrusion, fitted with a piston seal, which forms the seal around the supply tube.

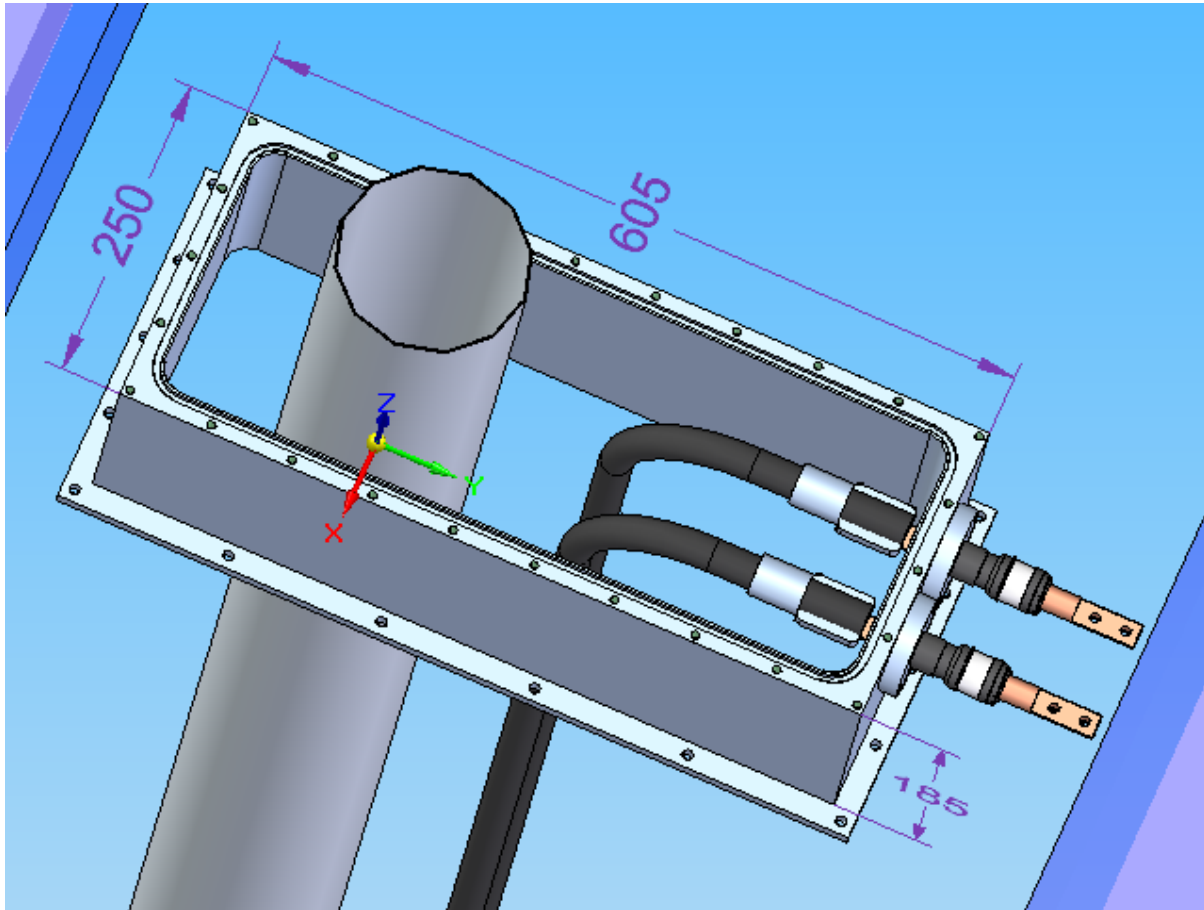


Figure 67: Hood above helium container with gas cooling supply and coil power connections (sensor wiring not shown, will be parallel to coil power cables)

## 6. Sensors

### 6.1. Temperature sensors on magnet coil

Simple and robust temperature sensors should be mounted on the surface of the magnet coil. As the radiation levels are not prohibitively high one suitable type is a PT100 (or PT1000) platinum sensor. Another type is a K-type thermocouple. The platinum sensors are more accurate but require a four-wire measurement setup. The thermocouples are less accurate, and due to their low level of sensing voltage they are sensitive to electro-magnetic noise, but only require a two-wire connection. One of the manufacturers of thermocouples, Omega, recommend a maximum length for the sensor wire of 30m.

Figure 68 shows a strain-relieved sensor arrangement which can be directly glued onto the body of the aluminium coil.



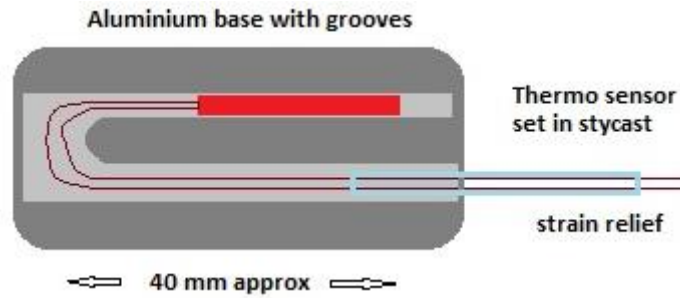


Figure 68: Temperature sensor, set in Stycast, on aluminium substrate

## 6.2. Magnetic flux density at defined locations

The usual method for measuring magnetic flux density is by the use of Hall sensors. These sensors are small, a few square millimetres, and the measured fields are strongly dependent on the orientation of the sensor. Measurement in a solid steel block requires a slot to be cut into the steel and the location and shape of the slot will influence the reading of the Hall sensor. The Hall sensor should be embedded in a very shallow slot perpendicular to the flux direction with dimensions close to the dimensions of the Hall sensor itself. In this way the flux of the core of the magnet will be measured as accurately as possible. If the slot dimension is large parallel to the direction of the flux then the flux within that slot will tend towards a zero value as flux will bypass this volume through regions with high magnetic permeability.

In Figure 69 the proposed location of the Hall sensors is shown. They should be embedded in very shallow cut-outs in the steel yoke, fixed by Epoxy resin and the sensor wires should be guided, in a shallow recess, to the space where the magnet coil is located. In that space the two wires from each sensor should be routed in the 4-wire configuration in order to compensate for signal inaccuracies on the way to the measuring instrument. Each location of the Hall sensors (centre, left and right) should contain two Hall sensors to assure redundancy provision for the signal should one of the sensors become damaged.

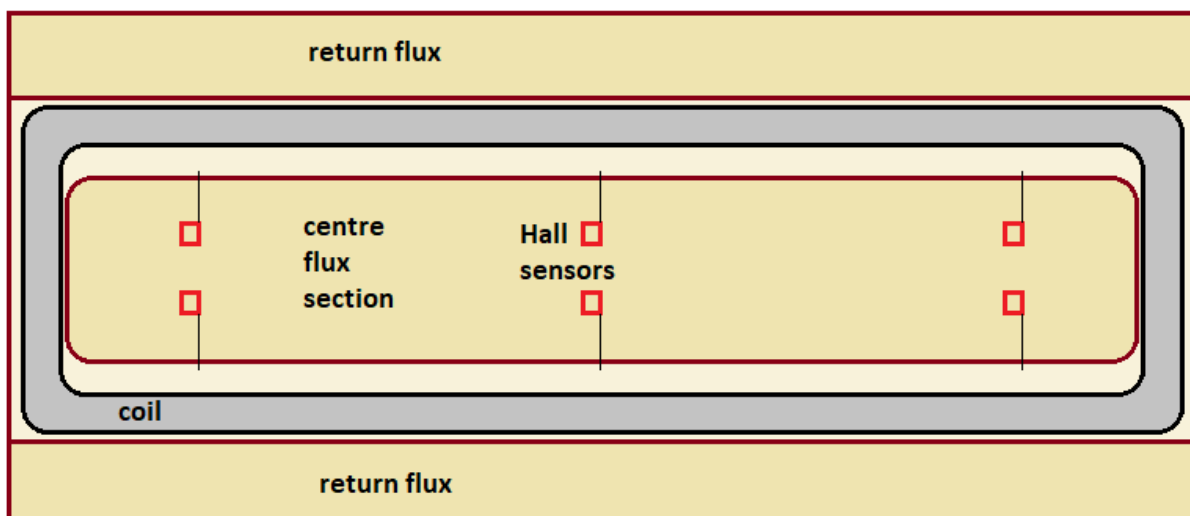


Figure 69: Location of Hall sensors on the steel yoke as seen from below, Hall sensors doubled for redundancy

### 6.3. Flux density integral over core of magnet

The flux density integral can be measured via the principle of Faraday induction. This principle says that there is an induced voltage in a loop of electrical conductor if the magnetic flux through that loop changes.

$$U = -d\Phi/dt, \text{ or } U = -N \cdot d\Phi/dt \text{ for } N \text{ turns of the loop, } \Phi = B \cdot A \text{ (Flux = flux density x Area)}$$

The time-changing field through the loop can either be caused, dynamically, by the loop area changing (see rotating pick-up coil) or, statically, by the magnetic flux changing during the ramping of the magnet. Magnetic flux density is measured in  $V \cdot s/m^2 = Wb/m^2 = T$ . Connecting an integrating voltage recorder to the ends of a current loop of known area, while ramping the magnet, will give the integral value in  $V \cdot s$ . Dividing this value by the area of the loop, and dividing it by the number of turns of the loop, will give the magnetic flux integral over the measured area.

Example: ramp magnet to 1.6T over 60s with an area of  $2.76m^2$  (4.6m x 0.6m):

$U = 1.6T \cdot 2.76m^2 / 60s = 0.0736V$  for one turn of the sensing loop. The integrated signal would therefore be  $0.0736V \cdot 60s = 4.416 Vs$ . The very low voltage in that loop may be suffering from noise and a sensing coil of 10 wire loops may be more appropriate, resulting in an integrated signal of 44.16Vs.

Integrating voltage meters are available. Those instruments often store data over a short period only, typically minutes but at a low voltage level. It is important to select an integrating Fluxmeter with a large-enough recording range, expressed in mVs, or Vs. The company Magnet-Physic (Dr Steingroever) seems to produce integrating fluxmeters without any restriction to range.

A dedicated data logger for the ramping of the magnet can be used instead where the data logger should be able to integrate the signal over the ramping time. A data logger from Dewetron, model Trionet and a Trion multi-card, has been used for this purpose.

The alternative is to power the coil in current control mode, assuring a constant rise in current and, therefore, magnetic flux. The integrated flux density is then simply the achieved maximum voltage on the pick-up circuit multiplied by the time for the ramp, and dividing the product by the number of turns and by the factor 2 (triangle, Figure 70).

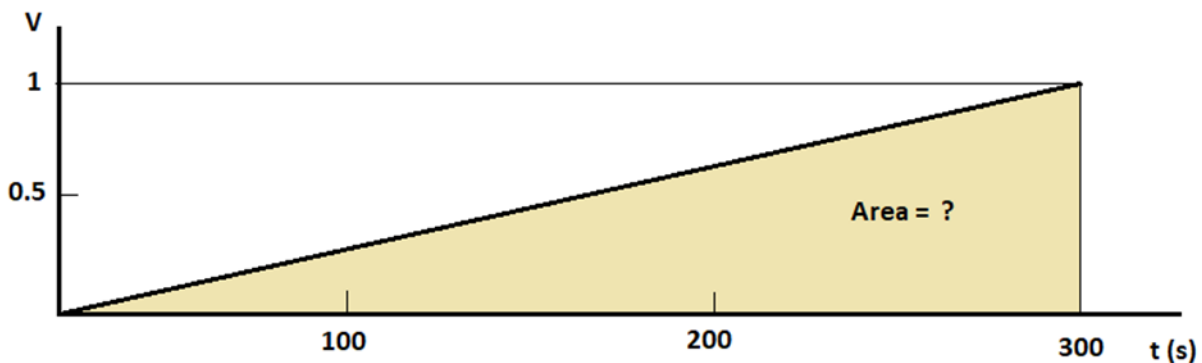


Figure 70: Example of a simple method for calculating the integrated flux through the magnet structure

Delta Elektronika of The Netherlands produces power supplies that are programmable for ramp rates. For instance, their SM6000 series of DC power supplies can provide 400A DC and more than one unit can be switched in series to achieve a maximum of 600V (<https://www.delta-elektronika.nl/en/products.html>).

## 7. Requirements for the operation of the magnet coil

The magnet coil will be operated below ground level, embedded in a large assembly of steel blocks. The supplies to the magnet coil are three-fold:

- Electric power
- Gas cooling
- Signal instrumentation, sensors

The supplies will need to go through the ceiling of the enclosing helium container. The helium container surrounds the entire target / magnet volume in order to prevent oxidation and corrosion of the steel blocks and target.

## 8. Information relevant to manufacture

### 8.1.Potential suppliers

The suppliers listed below are a selection from a larger pool of potential suppliers. No recommendation for any particular supplier is given here.

#### 8.1.1. Magnet coil

Aluminium coils are extensively used in hostile environments. Typically these coils are potted in some kind of resin, rubber, bitumen or other materials and the coils bodies are then encased in stainless steel, usually embedded in a ferromagnetic former that enhances the magnetic flux. The coils are then operated in switch on / off mode with a short duty cycle and a relatively high current density, or powered in permanent mode where the current density is very much reduced. As the coils can operate at very high temperatures forced cooling by gas or liquid is not normally applied. Current densities of 1 – 3 A/mm<sup>2</sup> are the usual range of operation. The manufacturer of the anodised aluminium strip can also be the manufacturer of the coils, or a coil manufacturer simply procures the material from that company and winds his own coils.

Some suppliers are listed here:

Anofol (Steinert Elektromagnetbau GmbH), Widdersdorfer Str 329 – 331, 50933 Cologne, Germany, Tel +49 221 4984-156, [www.anofol.de](http://www.anofol.de), manufacturer of aluminium strip and coils

Rotary Engineering, Old Lane, Halfway, Sheffield S20 3GZ, UK, Tel +44 114 251 3134, [www.rotary.co.uk](http://www.rotary.co.uk)

Anoxal, Umwelttechnik Wesselmann, Auf dem Knuf 21, 59073 Hamm, Germany, Tel +49 2381 87130-0, [www.anoxal.com](http://www.anoxal.com), manufacturer of aluminium strip and coils.

### 8.1.2. Magnet instrumentation

Power supplies are available from Delta Elektronika. As a guide, a 50V, 200A power supply unit will be sufficient. For the de-magnetisation of the iron former a bi-polar power supply would be advantageous (+/- voltages). As an alternative one could simply swap the power outlet cables on the power supply to achieve the same effect from a mono-polar PSU, ie reducing the current in stages with a consequent weakening of the residual magnetisation of the iron.

A temperature monitor with a display of eight channels is available from Lakeshore Cryotronics, model 218, suitable for the simultaneous display of up to eight temperatures

Gauss meter: Lakeshore F71 Multi-axis Teslameter, 3 sensor inputs, with Lakeshore Hall Sensors

Flux meter: Magnet-Physik, Dr Steingroever GmbH, Electronic Fluxmeter EF 5

### 8.1.3. Low carbon steel

One source for low carbon steel is the British Steel company in Scunthorpe, North Lincolnshire, UK. The material they can offer is in cast form, not rolled and they offer the sizes (minimum quantity is 280 t, one full cast) given in Table 11.

**Table 11: Sizes of low carbon steel available from British Steel**

Square billet,	Rectangular bloom	Slab
140x140mm or ,	283x230mm	800x225mm
180x180mm,	330x254mm	1100x225mm
Length 8.0-14.0m	355x305mm	1270x225mm
	483x305mm	1425x225mm
	Length 4.0-9.6m	1530x225mm
		1540x300mm
		1610x225mm
		1830x225mm or 300mm
		1970x225mm or 300mm
		Length 6.9-10.5m

## 8.2. Proposal for the development phase

We would strongly recommend that a ~¼ scale prototype magnet is made. This would allow the design for the thermal and magnetic design to be tested, as well as raising any manufacturing issues before the larger coils were made. A 2D magnetic model for such a coil is shown in Figure 71. A magnet of this scale would take 6-9 months to design, manufacture and test. The time requirement is mainly influenced by the supply of the steels, both low carbon and stainless. The stainless steel between the magnet paths may be avoided if it can be shown that the relative permeability is close to 1.

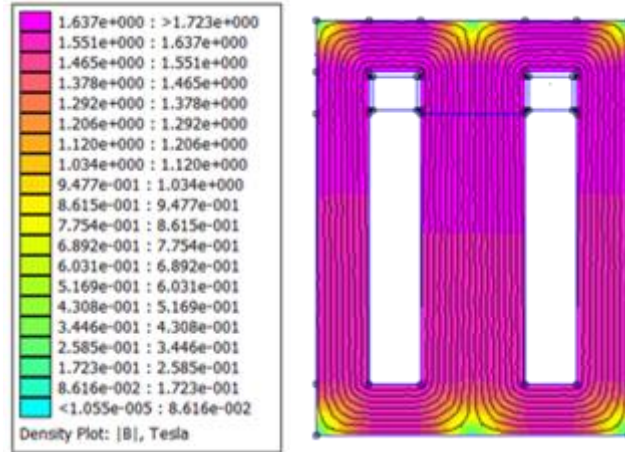


Figure 71 2D model for a quarter-scale prototype magnet

This prototype coil could also be modified to test a grain-orientated hybrid magnet (where the vertical sections could be replaced with GO steel, see Figure 72). The magnetic flux density will be increased significantly within the grain-oriented steel and the low carbon steel will have to be thickened to allow the higher flux density to flow without much reluctance.

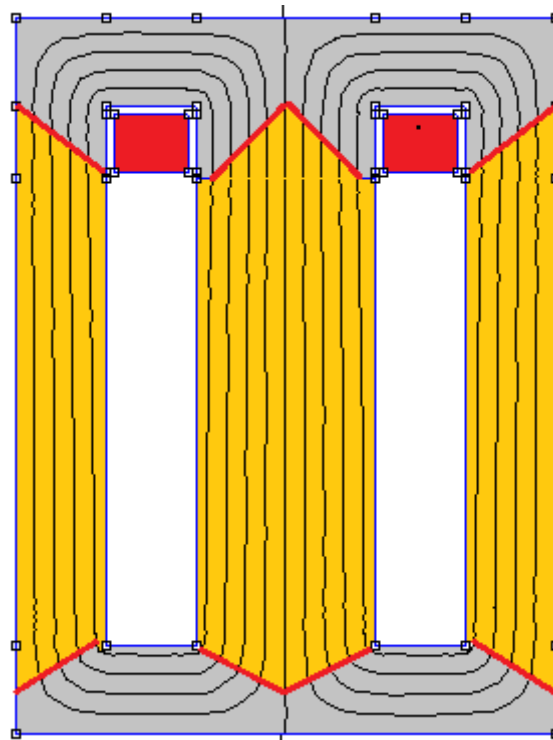


Figure 72: Hybrid magnet structure, showing low carbon steel (grey), grain-oriented steel sheets (yellow) and magnet coil (red). Stainless steel is shown in white.

### 8.3. Production of the final magnet system

The final, full-size magnet structure scales approximately with the weight of the magnet components. Aluminium coil costs are in the range of EUR 10 / kg.

Steel prices are highly volatile and a record of prices are given in the web pages of MEPS International Ltd<sup>11</sup>. It is not unusual that prices double or halve in a relatively short time span, as has been seen in the early 2000's when European steel supply faced shortages due to the high demand in the Far East. The prices are also severely influenced by the volume of the supply. Some manufacturers run special charges from their furnaces for particular grades of steel, with an accompanying cost.

At the time of writing this report the price of US1010 steel is around EUR 9,000 per cubic meter, machined to size. This figure has been arrived by using a budgetary quotation for raw, cast steel blocks from a steel supplier and doubling this figure to take into account the necessary machining of the blocks. The actual pricing will be very much influenced by the shape and size of the individual blocks.

The price of stainless steel 304 or 316 can be a factor of 3 or 4 higher than low carbon steel.

The magnet former has been minimised in size in this report and the cost will now be driven by the machining. If the former is assembled from plate material it is strongly recommended that the former should be annealed after machining. Annealing will reduce the stresses within the welds of the assembly and increase the magnetic permeability. The price of such an assembly can only be an estimate at this stage as the authors have no direct information on companies that can anneal such large components. It is, of course, possible, to anneal the long former in two or three sections. The sections must be split along the long axis in order to keep the high permeability orthogonal to the beam axis, i.e. in line with the direction of the magnetic flux.

Once the steel has been supplied a time requirement of manufacturing and assembly of the coil in its former would be between 6 and 9 months.

---

<sup>11</sup> [www.meps.co.uk](http://www.meps.co.uk)

## 9. Final Design

The final baseline model with these changes implemented gives an integrated field along the beamline of 7077Tmm and a maximum field of 1.57T. The field profile along the beamline is given in Figure 28.

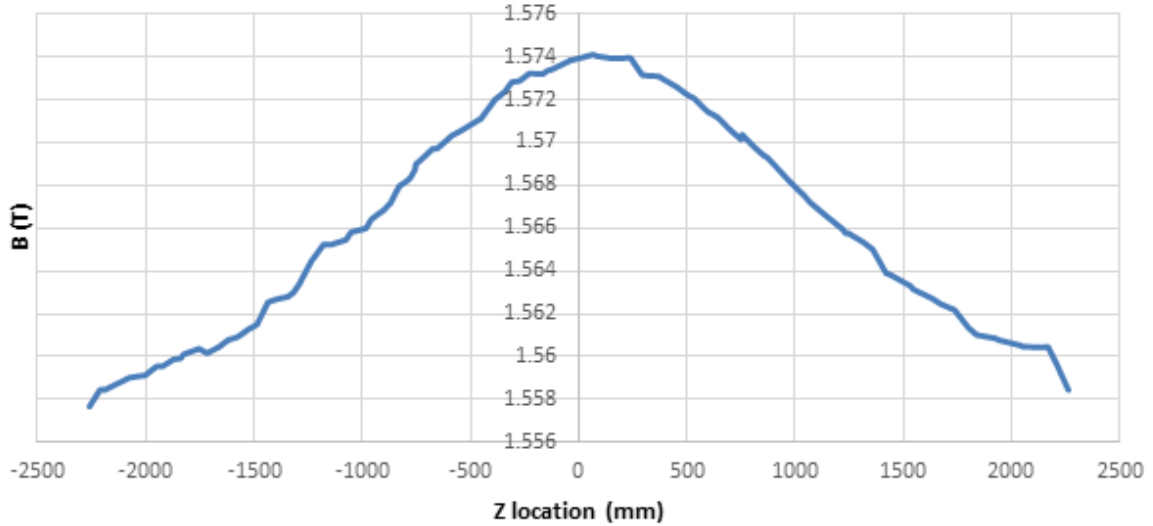


Figure 73: B-field profile along the beamline in final model

This is the coil data used as inputs to the modelling, as taken from the description of Coil B in Table 2.

<i>Current density</i>	<i>A/mm<sup>2</sup></i>	0.45
<i>Ampere-turns at design current density</i>	<i>Ampere-turns</i>	32,013
<i>Coil height</i>	<i>mm</i>	300
<i>Coil width</i>	<i>mm</i>	264
<i>Power at design current density</i>	<i>W</i>	4000

The overall dimensions of the magnet body, and the distribution of materials, can be seen in Figure 74 below. No individual metal blocks, or the coil itself is shown in this outline drawing.

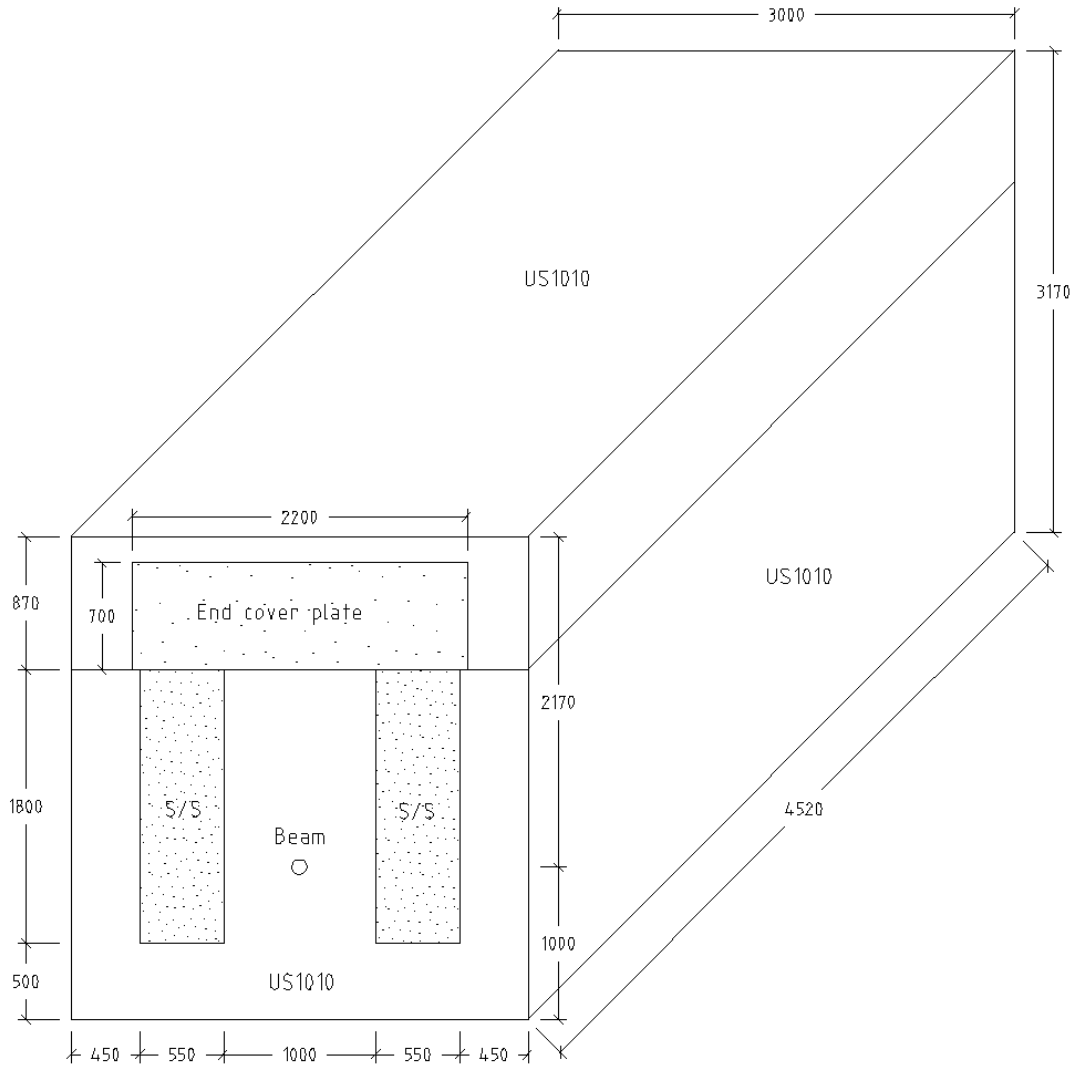


Figure 74 Outline of magnet body, showing materials and dimensions, magnet coil behind end cover plate



## 10. Conclusions

CERN has been evaluating the feasibility of a new experimental facility, the so-called Beam Dump Facility (“BDF”), with the primary goal of hosting the search for Hidden Particles (“SHiP”) experiment. SHiP would require a magnet-based shield immediately after the proton target in order to deflect the very large background flux of muons away from the detector acceptance. The inclusion of a magnet system integrated within the hadron stopper in the target bunker has been shown by the physics re-optimization to greatly improve the performance, and reduce the overall size and cost, of the free-standing part of the muon shield.

The aim of this work package was to move the design of this magnet system in the target shielding of the BDF from a conceptual stage to a preliminary engineering design. This has been done taking into account the constraints on the design and integration aspects of the magnet system imposed by the integration and remote handling of the target complex.

The initial aim was to generate a 1.8T field along the beamline downstream of the target. However, when the magnet power was traded-off against the integrated field, it was clear that the gain in integrated field when moving from a 4kW magnet (which could be gas cooled) to a 25 kW magnet (which has to be water cooled) could not be justified. This was primarily due to the additional operational risks of using water cooling within the target bunker where it could be avoided. This report treats both designs, and finally focuses on the design of a 4kW gas cooled magnet coil.

The work completed has focused on two distinct areas: developing useful 3D magnetic models of the complete target bunker and practical considerations of implementing the magnet. This work has demonstrated that it is possible to operate the magnet as a gas cooled unit, thereby avoiding the need for water cooling in the vicinity of the coil, while still fulfilling the requirements of the SHiP and the BDF project. When implementing this design it is important that care is taken to ensure the BH properties of the materials chosen are as desired as these will have a significant impact on the achievable integrated B-field. Another key issue is the manufacturing tolerances and alignment of the magnetic iron blocks, as these will again have a significant impact.

There is some consideration given to how this work would continue in the future, in particular the costs and timescales involved. It is strongly recommended that a prototype magnet of quarter scale should be made and tested prior to design and procurement of the full scale magnet.

## Appendix A. BH data used in magnetic modelling

### US1010

B (T)	97% B (T)	H (kA/m)
0	0	0
0.5757	0.558429	0.166317
0.68	0.6596	0.198944
0.7918	0.768046	0.240324
0.8949	0.868053	0.288866
0.9921	0.962337	0.347356
1.0821	1.049637	0.417623
1.164	1.12908	0.502134
1.2373	1.200181	0.603675
1.3021	1.263037	0.725747
1.3586	1.317842	0.872169
1.4074	1.365178	1.048831
1.4494	1.405918	1.261303
1.5171	1.471587	1.82312
1.5451	1.498747	2.191564
1.5955	1.547635	3.167183
1.6455	1.596135	4.578888
1.7019	1.650843	6.619254
1.7679	1.714863	9.567599
1.8045	1.750365	11.49894
1.8432	1.787904	13.83056
1.8831	1.826607	16.62373
1.9236	1.865892	19.98986
1.9636	1.904692	24.0316
2.0022	1.942134	28.89299
2.0384	1.977248	34.73557
2.0713	2.009161	41.76226
2.1003	2.037291	50.20941
2.1251	2.061347	60.37543
2.1461	2.081717	72.57465
2.1646	2.099662	87.2567
2.1869	2.121293	104.907
2.2137	2.147289	126.1223
2.2458	2.178426	151.5951

**Cast Iron**

B (T)	95% B (T)	H (kA/m)
0	0	0
0.314	0.2983	1.2
0.511	0.48545	2.2
0.781	0.74195	3.45
1.007	0.95665	5
1.175	1.11625	7.2
1.328	1.2616	10.4
1.533	1.45635	20
1.591	1.51145	26.034
1.62	1.539	30

**Appendix B. BH curves used in the Hysteretic Opera model**

**US1010**

B (T)	H(A/m)
-2.2458	-151595
-2.1869	-104907
-2.1461	-72574.7
-2.1003	-50209.4
-2.0384	-34735.6
-1.9636	-24031.6
-1.8831	-16623.7
-1.8045	-11498.9
-1.7019	-6619.25
-1.5955	-3167.18
-1.52434	-1854.91
-1.46479	-1439.36
-1.41249	-1192.7
-1.33375	-944.283
-1.20766	-694.37
-0.94915	-454.437
-0.61029	-298.628
-0.24842	-218.523
0	-179
0.419287	-126.021
0.781692	-32.5616
1.086223	166.3881
1.30045	428.6091

1.401911	800.0341
1.488671	1127.2
1.514053	1461.744
1.5451	2191.564
1.6455	4578.888
1.7679	9567.599
1.8432	13830.56
1.9236	19989.86
2.0022	28892.99
2.0713	41762.26
2.1251	60375.43
2.1646	87256.7
2.2137	126122.3
2.2458	151595.1

**GJS400-15\_Hysterisis (Cast Iron)**

<b>B (T)</b>	<b>H(A/m)</b>
-1.642	-30000
-1.576642336	-23103.448
-1.503649635	-17931.034
-1.386861314	-12500.000
-1.211678832	-8103.448
-1.00729927	-5689.655
-0.824817518	-4051.724
-0.394160584	-1896.552
-0.204379562	-1120.690
0	-344.828
0.248175182	517.241
0.729927007	2586.207
0.97810219	4051.724
1.065693431	4655.172
1.145985401	5689.655
1.262773723	7672.414
1.379562044	10689.655
1.445255474	14137.931
1.532846715	20172.414
1.591240876	26034.483
1.620	29999.000
1.642	30000.000